NANOMATERIAL-ENABLED MEMBRANES FOR WATER TREATMENT

By

Adam Roy Rogensues

A THESIS

Submitted to
Michigan State University
in partial fulfillment of the requirements
for the degree of

MASTER OF SCIENCE

Environmental Engineering

2012

ABSTRACT

NANOMATERIAL-ENABLED MEMBRANES FOR WATER TREATMENT

By

Adam Roy Rogensues

Incorporating engineered nanomaterials as components of synthetic membranes can improve their separation performance and endow membranes with additional functions. This work explores two approaches to the design of membranes modified with nanomaterials. In the first chapter, exfoliated graphite nanoplatelets (xGnP) decorated with gold nanoparticles were embedded in a polysulfone matrix to fabricate phase inversion nanocomposite membranes. The cast membranes were evaluated as flow-through membrane reactors in experiments on the catalytic reduction of 4-nitrophenol. The nanocomposite membranes were not as catalytically efficient as those fabricated by modifying anodized alumina membranes polyelectrolyte multilayers (PEMs) containing gold nanoparticles. However, because of the facility of membrane casting by phase inversion and new opportunities enabled by the demonstrated hierarchy-based approach to nanocomposite membrane design, such membrane may hold commercial promise. In the second part of the study, the practicability of PEM-based nanofiltration was evaluated under conditions of precipitative fouling (i.e. scaling) by calcium sulfate. Polyelectrolytes were deposited onto 50 kDa polyethersulfone membranes to create PEM-based nanofiltration membranes. The prepared membranes were compared with the commercial NF270 membrane in terms of flux and rejection performance, as well as the morphology of gypsum crystals formed on the membrane surface. None of the PEM coatings tested inhibited scale formation.

AWKNOWLEDGEMENT

Special thanks to Wenqian Shan for assisting with TEM imaging, as well as a variety of other items throughout my research endeavor. I would also like to thank Julian Taurozzi, Fulin Wang, Alla Alpatova, Elodie Pasco, and Dr. Volodymyr Tarabara for all their assistance.

TABLE OF CONTENTS

LIST OF TABLES

LIST OF FIGURES

.

KEY TO SYMBOLS

C_ℓ	=	concentration of constituent in the membrane permeate, mg/L
C_o	=	concentration of constituent in the membrane feed, mg/L
k'	=	first order rate constant, sec^{-1}
ℓ	=	membrane thickness, cm
t	=	time, sec
u	=	linear velocity of the solution in the membrane, cm/sec
ΔP	=	applied pressure, N/m^2
η	=	dynamic viscosity, $N \cdot s/m^2$
R_m	=	membrane resistance, m^{-1}
$\Delta\pi$	=	osmotic pressure, N/m^2
β	=	blockage coefficient, unitless
A_{free}	=	unblocked membrane area, m^2
A_{total}	=	total membrane area, m^2
C_m	=	salt concentration near the membrane surface, mol
C_p	=	permeate salt concentration, mol
C_f	=	feed solution concentration, mol
d_h	=	hydraulic diameter of the membrane channel
∂	=	boundary layer thickness

D	=	ion diffusion coefficient, m^2/sec
h	=	membrane channel height, m
J	=	solvent flux through the membrane, m/sec
R	=	universal gas constant
T	=	absolute temperature, K
w	=	channel width, m

INTRODUCTION

A *nanomaterial-enabled membrane* could be defined as a membrane that incorporates materials that have at least one dimension measuring less than 100 nm in length, width, or height. Two novel and rapidly developing materials science approaches to membrane design are polymer nanocomposite and polyelectrolyte multilayer (PEM) membranes. This thesis is divided into two parts; one that discusses the development of polysulfone-graphene nanocomposite membranes and the other that describes an evaluation of the performance of polyelectrolyte multilayer membranes in desalination applications.

Polymer Nanocomposite Membranes

Design of polymer nanocomposite membranes is an active direction of membrane science research. This field has gained increased attention largely due to advancements in nanoparticle (NP) fabrication and characterization techniques. A wide variety of NP enabled membranes has recently been developed. A few examples include membranes embedded with silver [1], C_{60} fullerenes [2], gold [3–5], silica [6], [7], titanium dioxide [8], and carbon nanotubes [9]. The subject of the first chapter of this thesis involves the use of a comparatively cheap, remarkably strong, carbon NP trademarked as exfoliated graphite nanoplatelets (xGnP™) as the foundation for creating a multifunctional NP enabled membrane. xGnP was chosen primarily for its relative affordability and remarkable strength; recent developments in fabrication techniques have dramatically decreased the cost of these NPs to under $5 per lb and they have been shown to have an elastic modulus of over 1 TPa [10].

Thin Film Composites

TFC membranes have been fabricated using a variety of techniques. Popular techniques include dip-coating, spray coating, spin coating, interfacial polymerization, in-situ polymerization, plasma polymerization, and grafting [11]. Among others, dip coating, in this case involving layer-by-layer deposition of polyelectrolyte films, has attracted considerable attention in recent years [3–5], [12–17]. Layer-by-layer (LbL) deposition has been defined as the alternating adsorption of polycations and polyanions onto a support structure [13]. The second chapter of this thesis describes our efforts to evaluate the performance of membranes fabricated using the LbL technique under conditions of precipitative fouling.

CHAPTER 1

NP ENABLED MEMBRANES: XGNP-POLYSULFONE NANOCOMPOSITE MEMBRANES

1.1 Background

One of the driving forces behind the development of NP enabled membranes is the ability to utilize NPs to introduce additional functions to the membrane filtration process. This is often achieved by incorporating NPs capable of performing additional functions into the membrane matrix. Such membranes with added functionalities are often termed multifunctional membranes. A multifunctional membrane could be defined as a permeable or semi-permeable entity capable of performing functions in addition to its inherent separation function. A few examples of demonstrated membrane functionalities include sorption [18–22], catalysis [3–5], [12], biocidal functions [1], and controlled release capabilities [23–25].

1.1.1. Catalytic Flow-Through Membranes

A catalytic flow-through membrane reactor is a device that combines two distinct functions - reaction and separation - into a single unit. This synergistic process is not a novel concept, but did not gain substantial interest until recently [26]. Most progress is this field has taken place in the last twenty years, although the first publications on the topic appeared in the early 1960's [26]. In the early stages of reactive membrane separations, two physically distinct reaction and separation units were coupled by simply connecting the reactors in series. The combining of the two processes into a single unit was the result of natural design evolution [26].

A common method for preparing catalytic flow-through membrane reactors involves embedding precious metal nanoparticles (e.g. Au, Pt, Ru) that are used as the catalysts into the membrane matrix. This can be achieved as an additional step during

membrane casting by *immersion precipitation*. The second method involves adding functional nanoparticles only to select areas of the membrane matrix; this can be accomplished, for example, using layer-by-layer film deposition technique [3–5].

The former membrane fabrication method, *immersion precipitation*, is one of the most commonly used membrane preparation methods and is used to produce most commercially available porous membranes [11]. The latter preparation approach, layer-by-layer film deposition, has been utilized by a number of authors [3–5], [12] and demonstrated impressive results, but to this author's knowledge, membranes fabricated using this technique have not yet been used to produce commercially available membranes.

1.1.2. Exfoliated Graphite Nanoplatelets

Carbon nanoparticles have attracted significant attention over the past two decades due to their superior mechanical, electrical, and thermal properties, as well as other unique characteristics [27]. Recent research has largely focused on three types of carbon nanoparticles: nanotubes, fullerenes, and nanographite. Recent advancements in fabrication methods for nanographite in particular, have allowed for the production of a distinct form of nanographite known as exfoliated graphite nanoplatelets (xGnP). These particles can be produced for a cost of less than $5/lb, a relatively low cost in comparison with that of similar carbon nanoparticle allotropes [28].

Graphite has been defined as a stack of alternating graphene sheets [29]. A platelet of graphite consists of a number of graphene sheets bonded together by van der Waals forces. Single crystal graphite (i.e. graphene) is one of the stiffest materials

in nature; it has an elastic modulus of over 1 TPa [30]. Elastic modulus can be defined as a proportionality constant that directly relates the stress and strain of a material. Nanoscale graphite sheets (nanoplatelets) can be produced by expanding graphite that has been intercalated with acid, which separates the sheets along the c-axis (out of the plane) of the graphene layers [31]. An example of a typical graphite nanoplatelet produced via this process is shown in Fig. 1.1 [32].

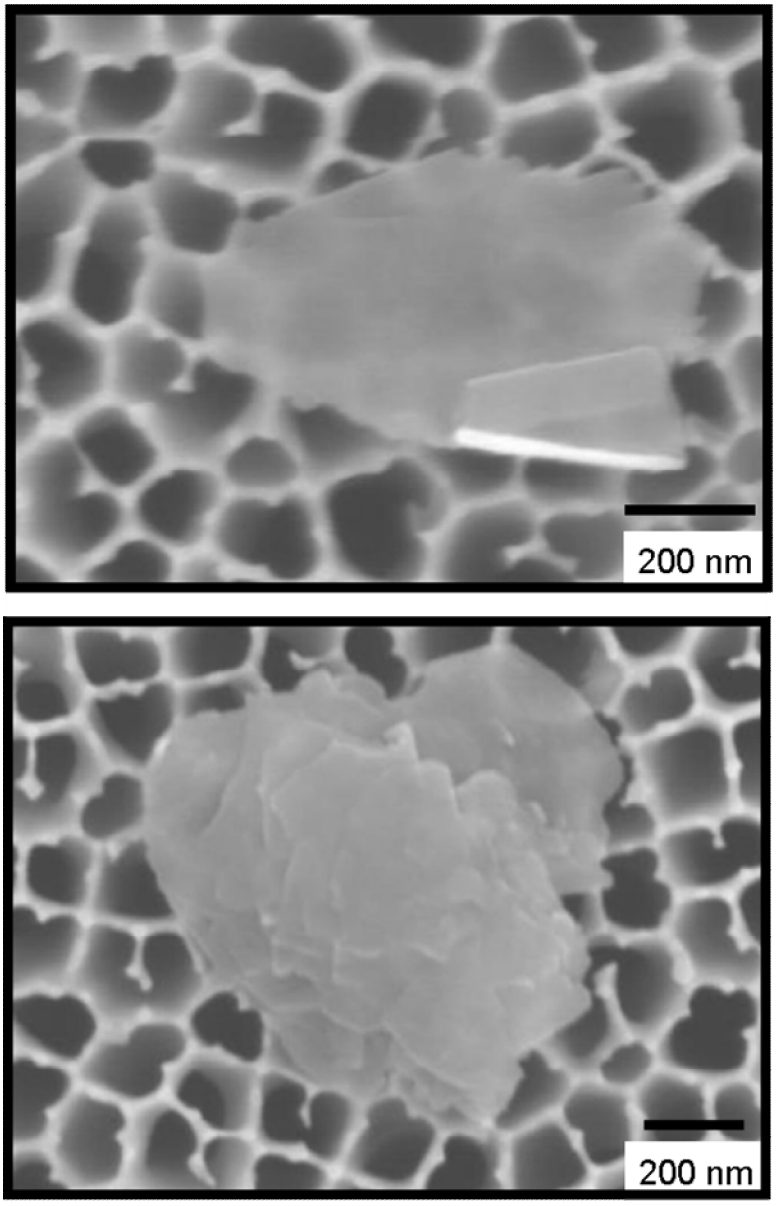

Figure 1.1. SEM image of a graphite nanoplatelets [32].

1.1.3. Gold as a Catalyst

Historically, gold was regarded to be catalytically inert [33]. However, since the discovery of surprisingly high catalytic activity for low temperature carbon monoxide oxidation [34], gold has been shown to be catalytically active in a range of reactions [33]. The catalytic activity of gold appears to be size dependent – smaller particles typically being more reactive while the bulk material is inert in nature [33], [35]. Due to their high surface energies, however, smaller particles in the low nanometer range often aggregate, which leads to decreased catalytic activity as less surface area is available for reaction [36]. In order to overcome this barrier, these nanoparticles are often immobilized on a suitable support material [37]. Commonly used support materials include TiO_2, SiO_2, activated carbon, Fe_2O_3, among others [33]. Additionally, it has been suggested that the Au/support interface plays a pivotal role in gold's activity as a catalyst [33]. Therefore, small nanometer sized gold nanoparticles are known to be catalytically active and the nanoparticle carriers are critical to the efficiency and functionality of the nanocatalyst.

1.1.4. 4-Nitrophenol

4-Nitrophenol (4-NP) is a synthetic chemical used to manufacture drugs, fungicides, insecticides, and dyes and to darken leather [38]. There have been numerous studies on the removal of (4-NP) from water by a range of unit processes [39]. They include adsorption [40], microbial degradation [41], photocatalytic degradation [42], and catalytic flow-through membrane reactors [3–5]. 4-NP also has laboratory-scale significance, in

addition to its role as a commercial and industrial compound; it is commonly used as an easy-to-detect, easy-to-characterize reactant [4] because concentrations are easily determined by spectrophotometry.

1.1.5. Nanoparticle Preparation via the Polyol Method

The polyol process is a convenient, versatile, low cost metallic nanoparticle preparation method [43] wherein a metal precursor is reduced using a polyol or diol in the presence of a surfactant. In the present study, the metal precursor was gold chloride, the polyol was ethylene glycol and the surfactant was PDADMAC. This system can be described by the following reactions [43]:

$$CH_2OH\text{-}CH_2OH \rightarrow CH_3CHO + H_2O \quad (1)$$

$$6CH_3CHO + AuCl_4^- \rightarrow 2Au^o + 3CH_2CO - COCH_3 + 6H^+ + 8Cl^- \quad (2)$$

During the reaction process the color of the reaction solution changes from yellow to colorless, then to a reddish color, which is indicative of nanoparticle formation. Li et al. [43] reported that this transformation is the result of as-formed Au atoms (eq. 2) being oxidized to $AuCl_2^-$ through (eqs. 3-5_, which is finally reduced to Au atoms through (eq 6).

$$Au^0 + AuCl_4^- + Cl^- \rightarrow AuCl_2^- + AuCl_3^- \quad (3)$$

$$2AuCl_3^- \rightarrow AuCl_2^- + AuCl_4^- \quad (4)$$

$$2Au^0 + AuCl_4^- + 2Cl^- \rightarrow 3AuCl_2^- \quad (5)$$

$$2CH_3CHO + 2AuCl_2^- \rightarrow 2Au^0 + CH_3CHO - COCH_3 + 2H^+ + 4Cl^- \quad (6)$$

1.1.6. NP Bonding Mechanism

A survey of the literature suggests that there exist two generally accepted theories for the mechanism of bonding between metallic nanoparticles produced via the polyol method and the carbon support. The first bonding theory focuses on the functional groups that are typically located along the perimeter of the catalysts support carbon nanoparticle. Most of the functional groups (carbonyl, carboxyl, and hydroxyl [27]) are indeed along the edges of the carbon nanoplatelet in the case of xGnP. These functional groups purportedly act as seed locations for the growth of metallic nanoparticles. More specifically, the metal ions are nucleated by the surface functional groups and upon heating the reaction mixture, the metal ion is reduced to nanosized particles [44–46]. This hypothesis is further supported by the findings of Lordi et al. [47] who did not see adsorption of platinum nanoparticles to the surface of SWCNTs without chemical oxidation, which typically involves soaking the NPs in a strong acid or a combination of strong acids for an extended period of time, to introduce functional groups to the tubular surface of a carbon NP [48]).

An ion exchange reaction can be defined as the reversible exchange of ions between a liquid and a solid [49]. In reference to the process described in the preceding paragraph, the functional groups contain an atom that is bonded to the functional group predominately via an ionic bond. The metallic ion replaces the atom

previously stored in the functional group (which is located on the surface of the carbon nanoparticle). The metallic ion is then reduced upon heating of the polyol mixture, thus creating a nanoparticle growth seed. The seeds then grow by gathering neighbor particles via van der Waals forces [50]. An example of such a reaction is shown below [48]:

$$xGnP \cdot COOH + Au^{\oplus}X^{-} \rightarrow xGnP \cdot COO^{-}Au^{\oplus} + HX \qquad (7)$$

The gold-carbon bonding scenario described above does not explain the attachment of nanoparticles to the inert basal plane of the graphitic platelets, though it is generally accepted for the instance where functional groups are present. This phenomenon has been explained by the secondary theory as follows. The surface basic sites are of Lewis type and are associated with π-electron rich regions within the basal planes [51]. The protonation of the basic carbon sites lead to electron donor-acceptor complexes, which are responsible for the strong interactions between metal particles and graphite nanoplatelets [46], [51], [52].

The role of PDADMAC in the metal ion attachment to the carbon support was not considered within the scope of this research. However, it is important to note that the cationic surfactant (PDADMAC) could interfere with the ion-exchange reactions that take place between the positively charged metal ion and the predominately negatively charged surface functional groups. Specifically, the cationic surfactant could compete with the metal ion for the negatively charged surface groups. This could result in

reduced gold nanoparticle attachment to the xGnP support as fewer functional groups would be available to anchor the metal ion.

1.2. Hypothesis

We hypothesize that a catalytically active flow-through membrane can be easily fabricated by combining gold nanoparticles as the nanocatalyst, xGnP as the catalyst support, and polysulfone (PSf) phase inversion membranes as the porous polymer matrix. Gold nanoparticles will be fabricated via the polyol method, which will also serve as the method for xGnP nanocatalyst decoration, thereby streamlining the fabrication and decoration procedure. xGnP decorated with gold nanoparticles (xGnP-Au) will be dispersed in a casting solution of polysulfone membranes, thereby homogeneously dispersing the nanocatalyst throughout the entire polysulfone matrix. A membrane will then be cast using the immersion precipitation method. Next, 4-NP will be filtered through the resulting membranes in order to characterize the catalytic activity of the novel nano-enabled membranes.

It is our belief that membranes fabricated via the methods described above will be more robust than those recently reported [4], as they will be fabricated using a commercially-tested membrane fabrication technique. Furthermore, we surmise that these membranes will be as, or nearly as catalytically active as similar membranes prepared using the PEM method [4].

Additionally, within this study we also hope to demonstrate the ability to fabricate hierarchically structured nanocomposite membranes. We expect this to be a gateway procedure, leading to the development of more sophisticated, more functional, and more efficient membranes. For example, one could decorate a relatively large nanoparticle with superparamagnetic nanoparticles, thereby facilitating the in-situ manipulation of nanoparticle orientation with the use of simple magnetic or electric field.

1.3. Objectives

- Decorate xGnP nanoplatelets with gold nanoparticles via the polyol method. The protocol used will be similar to that outlined by Li et al [45] and Lu et al [46].
- Disperse gold decorated nanoplatelets into the casting solutions of polysulfone membranes and cast homogeneous nanocomposite membranes.
- Add xGnP-Au to the polysulfone membranes at a variety of concentrations and test catalytic activity as a function of xGnP-Au loading using 4-NP as the model reactant.
- Fit results to the simple model outlined by Dotzauer et al. [4] and calculate the reaction constant of the Au/xGnP-PSf nanocomposite membranes.

1.4. Methods and Materials

1.4.1. Chemicals and Reagents

xGnP's with an average plate diameter of 15 microns were donated by XG Sciences Inc (Lansing, MI). Sodium borohydride, 4-nitrophenol, polysulfone (Udel P-3500 LCD Pellets, MR8, 79 kDa), polydiallyldimethylammonium chloride (PDADMAC) (20 wt% aqueous solutions), 1M NaOH solution, ethylene glycol and acetone were all used as received.

1.4.2. Nanoparticle Preparation

xGnP decorated by gold nanoparticles xGnP (xGnP-Au) were fabricated via the polyol method [43], [45], [46], [50]. Our method for producing xGnP-Au was a combination of methods reported by Li et al.[43] and Lu et al. [46]. The method described by Li et al. [43] was used for producing gold nanoparticles and the method described by Lu et al [46] was used to decorate xGnP with the gold nanoplatelets. First, a desired quantity of xGnP was added to a mixture composed of 50 mL ethylene glycol and 1 mL of a 20 wt% PDADMAC solution. This mixture was stirred and sonicated for 1 h in order to adequately disperse the xGnP in ethylene glycol. Membranes to be loaded with 10% xGnP-Au loadings were sonicated for 12 hours due to dispersion and catalyst dissociation issues (this is described in more detail later in this report). Next, NaOH and $AuCl_4$ were added to achieve resulting solution concentrations of 3 mM and 0.5 mM, respectively. This mixture was mixed and then heated to 190 ^{o}C for 30 min to facilitate nanoparticle formation.

Ethylene glycol (EG) acts as the reducing agent for the metal salt when heated to the temperature listed above. PDADMAC acts a dispersion agent for the gold nanoparticles. NaOH is used to adjust the pH of the polyol solution, which has been shown to precisely control the size and morphology of the product gold nanoparticles [43]. xGnP was utilized as the nanoparticle support due to its large specific surface area and low cost.

After reacting for 30 min 190 ^{0}C, the mixture was centrifuged for 1 h at 8,000 rpm to separate xGnP-Au from the polyol solution. Particles were then rinsed in acetone to remove any residual ethylene glycol and allowed to dry overnight at 100 ^{o}C after separation by centrifugation.

1.4.3. Nanocomposite Membrane Fabrication

Nanocomposite membranes were fabricated via the phase inversion method [11]. The membrane casting mixture consisted of 65 wt% N-methyl-2-pyrrolidone (polymer solvent), 20 wt% polysulfone (polymer), 15 wt% PEG400 (porogen), and a desired quantity of xGnP or xGnP-Au. xGnP and xGnP-Au mass percentages added to the casting mixture were calculated according to wt% with respect to the polymer. Relatively high polymer content was used because, in our experience, at low polymer content nanocomposite membranes nanoparticles tend to escape the casting mixture, which results in wasted nanoparticles. Relatively high porogen concentrations were used to produce a relatively higher flux membrane.

Nanocomposite phase inversion membranes were fabricated by first adding a desired amount of xGnP/xGnP-Au to a NMP solution and sonicating the suspension for

1 h in order to disperse the particles. An increased sonication time of 12 h was needed to sufficiently disperse the particles in NMP for membranes with 10% nanoparticle loading. Next, polysulfone (PSf) pellets and polyelethelyne glycol 400 (PEG 400) were added to N-methyl-2-pyrrolidone (NMP) and the mixture was stirred at 60 ^{o}C on a heating plate for approximately 12 h to completely dissolve PSf (the dissolved mixture is known as a casting mixture).

Casting mixtures were inspected after this step to ensure the homogeneity of the solution. The solution was subsequently casted as a thin film with a drawdown thickness of 300±1 μm onto a flat sheet of Pyrex glass at room temperature using an ELCOR casting knife. The casted film and Pyrex glass were then gingerly, but immediately immersed in water bath to induce phase inversion and for the asymmetric polymeric nanocomposite membranes. Membrane sheets were then thoroughly rinsed with DI water to remove any residual NMP. All membranes were stored in a 1.5 wt% sodium metabisulfite solution in order to inhibit bacterial growth [53].

1.4.4. Catalytic Activity of Nanocomposite Membranes

Reduction of nitrophenolates to their corresponding aminophenolates in the presence of sodium borohydride provides an immediate, easily characterized reaction that can be used to evaluate the catalytic activity of nanoparticles embedded in a membrane matrix [4]. The reduction does not occur in the absence of $NaBH_4$ and both reactant and product are easily quantified using UV-Vis spectroscopy. 4-NP shows a strong absorbance peak at 400nm, the decrease of amplitude of this peak corresponds to a

decrease in 4-NP concentration. The gradual appearance of a peak at 300nm indicates the formation of 4-AP [4].

4-Nitrophenol reaction solutions were prepared by first weighing out a target mass of $NaBH_4$ and then adding a desired volume of deionized (DI) water. The desired volume of a 4-NP stock solution was subsequently added to the mixture in order to achieve the target concentration. This suspension was then briefly mixed and the reaction experiment initiated. All the reactions within this report were performed using a solution containing 0.5 mM 4-NP and 50 mM $NaBH_4$.

Reactions were carried out in a Millipore stirred ultrafiltration cell connected to a stainless steal feed tank. A clean glass flask was used to store the reaction fluid within the stainless steel tank to mitigate contamination and prevent degradation of the bulk solution. Bulk concentrations were measured as a function of time to quantify and compensate for any minor degradation of 4-NP in the solution.

4-NP concentrations were quantified using a UV-Vis spectrophotometer, as it shows a strong absorbance peak at 400nm. Flux data was gathered using a mass-balance interfaced with a LabView equipped a computer. The LabView program used for data-logging was written in-house.

1.4.5. SEM/TEM characterization

Membrane samples were freeze-fractured following immersion in liquid nitrogen, coated with gold for 20 seconds at a current of 10 mA and then mounted on SEM sample holders for SEM imaging of membrane cross-sections. A JOEL 6400 scanning electron microscope was used to image the membrane cross-sections.

A 10 μL droplet of xGnP-Au particles suspended in acetone was dropped onto 300 mesh standard copper grids and imaged using a JEOL 100 CX transmission electron microscope for the TEM imaging of xGnP-Au particles. The TEM was operated at an accelerating voltage of 100 kV, with a maximum theoretical resolution of 0.2 nm. Micrographs were recorded using a MegaView III Camera (Soft Imaging System, Lakewood, CO). TEM images of nanocomposite cross-sections were analyzed using the public domain NIH ImageJ program, Version 1.43u (developed at the U.S. National Institutes of Health and available on the Internet at http://rsb.info.nih.gov/ij).

1.5. Results and Discussion

1.5.1. Nanoparticle Characterization

A TEM image of an xGnP-Au platelet formed via the polyol processes is shown in Fig. 1.2. This image and similar images confirmed that gold nanoparticles were well distributed across the nanoplatelets surfaces. Figure 1.3 shows a photograph and a UV-Vis spectrum of EG waste solution produced during the polyol procedure. The deep red color indicates that not all gold nanoparticles from the reaction mixture bonded to the xGnP platelets. This is likely due to a relative shortage of overall bonding sites along the surface of the xGnP particle.

The strong peak at ~540 nm of the polyol reaction EG waste suggest an average Au particle diameter of ~20nm (Figure 1.3) [43]. Gold nanoparticles prepared via polyol synthesis have been shown to exhibit a linear correlation between adsorption peak position and particle edge length [43]. These optical properties of gold nanoparticles are the result of basic photophysical response that does not exist in nonmetallic particles. When gold nanoparticles are exposed to light, the oscillating electric field causes the conduction electrons to oscillate concurrently. This electron oscillation forms a dipole oscillation along the direction of the electric field of the light. The amplitude of the oscillation reaches a maximum at a specific frequency. The specific frequency is termed the surface plasmon resonance frequency, which induces a strong adsorption of the incident light that can be measured using a UV-Vis spectrophotometer [54].

A single experiment was conducted to evaluate the effect of introducing additional functional groups onto the xGnP surface after observing the results shown in

Fig. 1.2 and Fig. 1.3. Additional functional groups were added using a method described in detail by Goyanes et al. [55]. Basically, xGnP were treated with a solution of 1:3 HNO_3/$H2SO_4$ for a period of 2 h, filtered, washed, and dried overnight in an oven. The standard polyol synthesis procedure was then followed to the decorate xGnPs with gold. These results are shown in Fig. 1.4.

There appears to be an increase of gold loading onto the xGnP platelets, particularly around the perimeter of the platelet, when looking at these two images of Fig. 1.4 and comparing them with Fig. 1.2. These results support the results reported by Li et al. [45] and Lordi et al. [47]. We can therefore suggest that the introduction of additional functional groups to the perimeter of the xGnP appears to increase the Au loading onto the carbon nanoparticle surface via enhanced surface functionalization. However, this process involved the use of strong acids, therefore was not employed further, and needs quantifiable justification prior to drawing any formal conclusions.

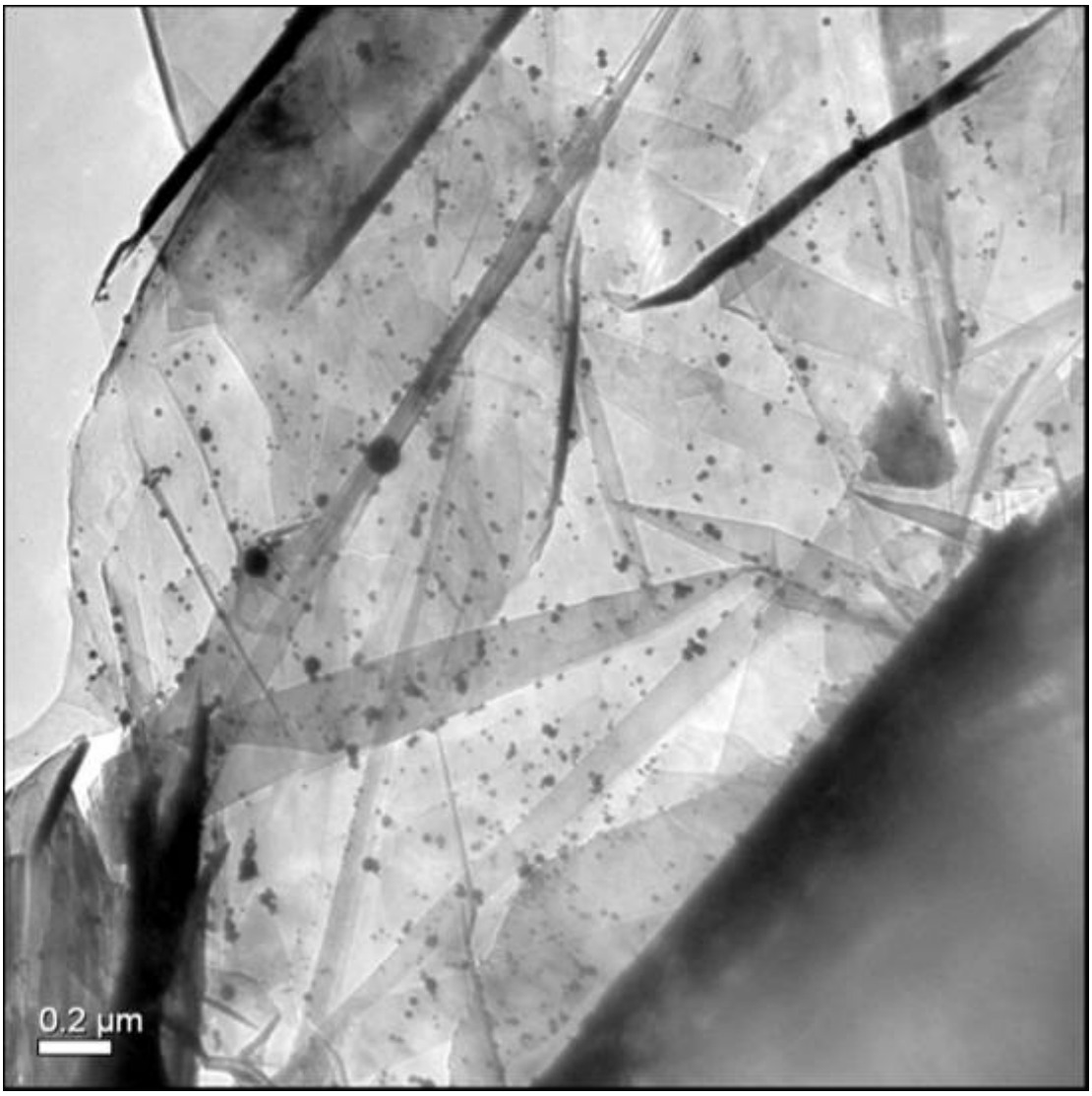

Figure 1.2. TEM image of an xGnP-Au particle.

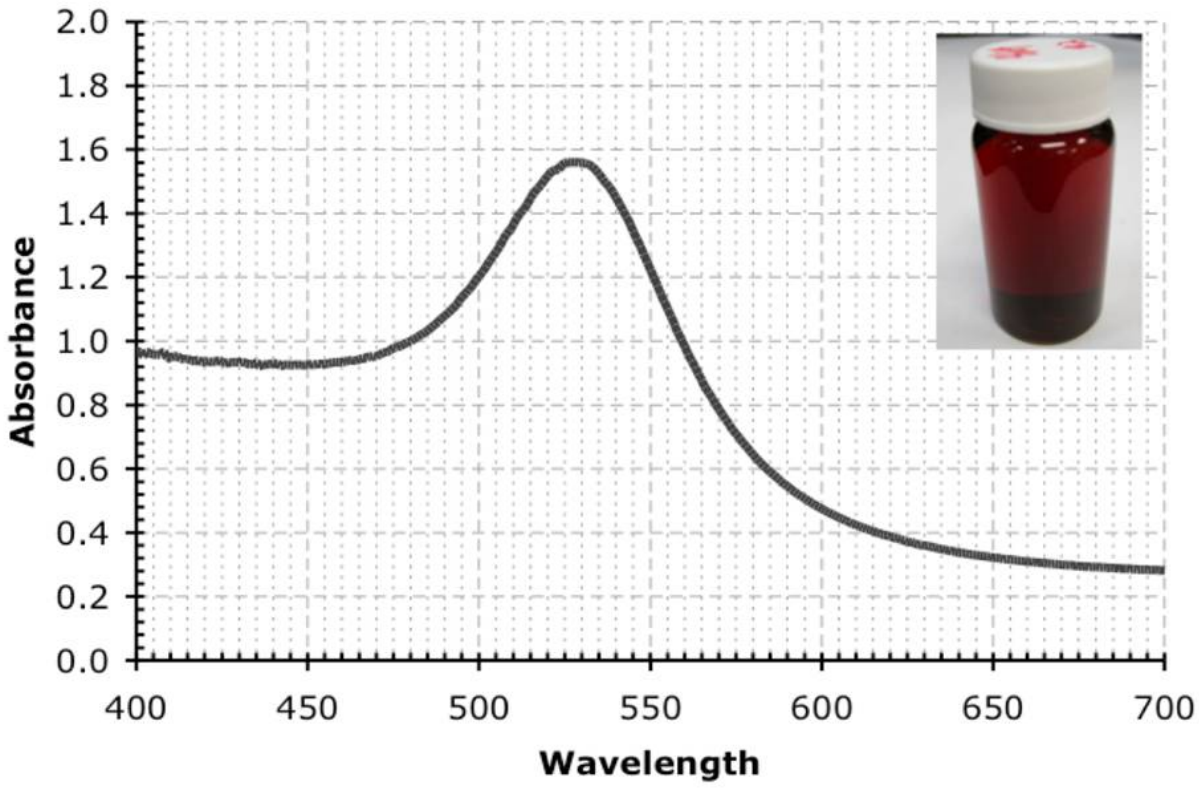

Figure 1.3. UV Vis spectra and a photograph of a vial containing EG waste from a polyol reaction. The strong peak at ~540 nm suggests a gold particle diameter of ~20nm.

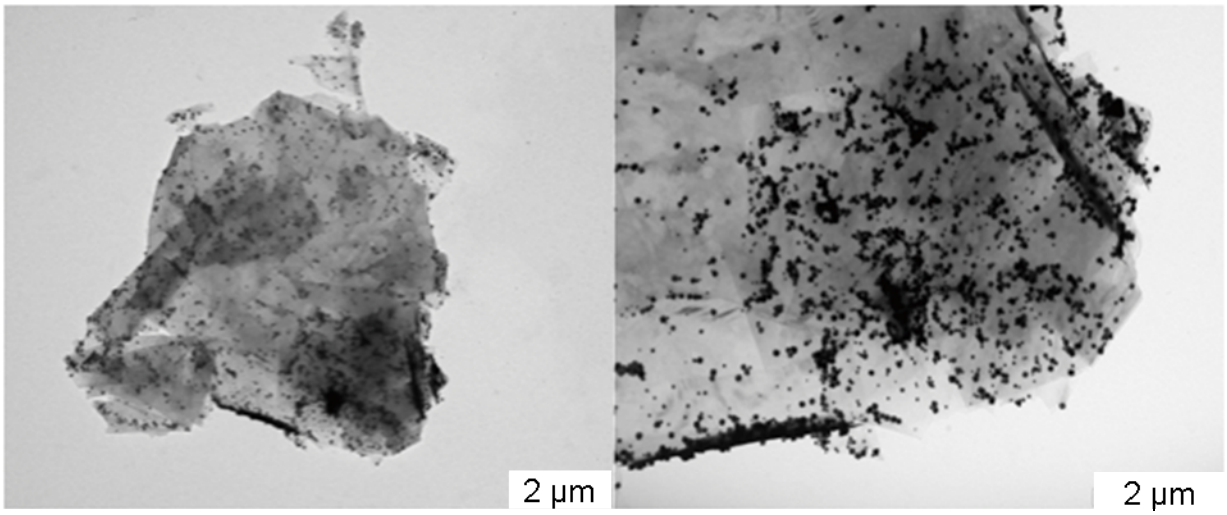

Figure 1.4. TEM image of a functionalized xGnP-Au. The particles were treated with a solution of 1:3 HNO_3/$H2SO_4$ for a period of 2 h, filtered, washed, and dried overnight in an oven in order to introduce additional functional groups to the xGnP particles. The additional functional groups are likely responsible for the apparent increase in gold loading observed when comparing these images to Figure 1.2.

1.5.2. Membrane Fabrication

Figure 1.5 is a visual outline of the general procedure used to prepare the xGnP-Au enabled membranes considered in this study. For control membranes - membranes impregnated with un-decorated xGnP - steps 1-9 were omitted, as no gold decoration was needed. In certain circumstances, there were a few modifications to the general procedure, however. The first modification was used for the preparation of membranes containing an xGnP loading of 10%. The higher loadings necessitated elevated sonication times to fully break up xGnP–Au aggregates in NMP. If not fully dispersed, these aggregates would get caught in the membrane blade and drag through the membrane film as it was being casted, creating tears in the membrane sheet. Therefore, for the xGnP-10% membrane, an elevated sonication time was used at step #11 of the fabrication procedure. This eliminated the presence of aggregates and enabled the production of visually scratch/seam-free membranes.

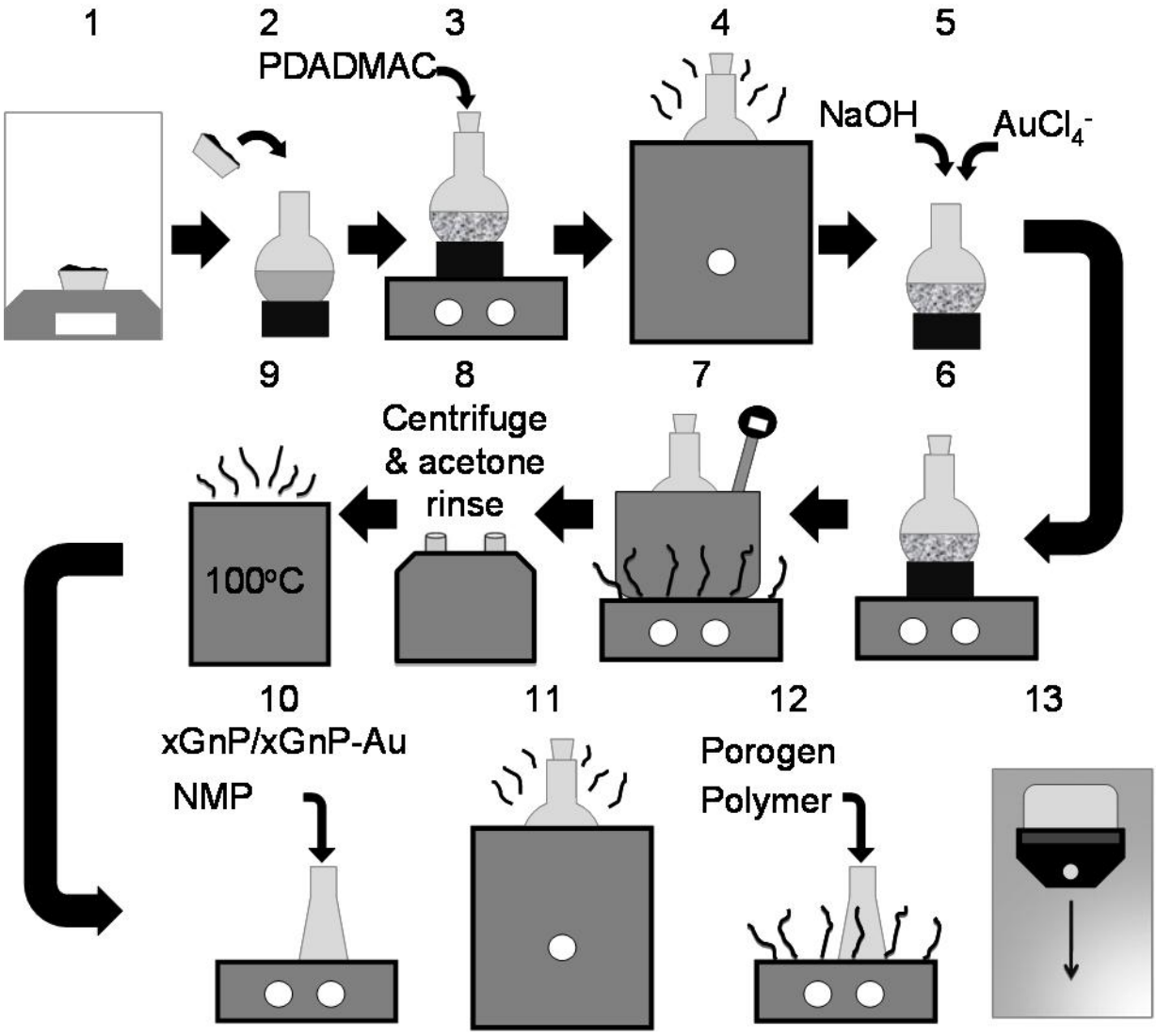

Figure 1.5. Schematic representation of the xGnp-Au particle fabrication and xGnP-Au nanocomposite membrane fabrication process.

Analysis of the xGnP-Au10% particles described above yielded a need to further modify the sonication protocol used for xGnP-10%. TEM analysis of the xGnP-Au10% particles sonicated for 12 h at step #11 (post gold decoration) of the fabrication procedure clearly indicated a loss of gold coverage. Elevated sonication times appeared to have caused the detachment of gold nanoparticles from the surface of xGnP. Figure 1.6 displays TEM images comparing the gold coverage of xGnP platelets that were sonicated for 1 h and for 12 h at step #11 of the preparation procedure. We clearly see that more gold was lost after 12 h of sonication than after 1 h sonication. To our knowledge, this is the first instance in which anyone has reported such phenomenon.

As an alternative approach, an elevated sonication time was introduced at step #4 of the fabrication procedure, as opposed to step #11. Therefore, the extended sonication treatment was carried out prior to the decoration of xGnP with gold nanoparticles. Potential side effects of this approach were 1) the further exfoliation of the graphite nanoparticles and 2) potential fracturing of the graphite nanoplatelets. The former likely created more surface area available for particle decoration and the latter likely introduced more functional groups, which would make more anchor sites available for particle decoration – both processes should result in an increase in gold decoration.

Figure 1.7 is a comparison of the EG waste from two different polyol experiments, the sample on the right was subjected to 1 h of sonication time at step #4 and the sample on the left was subjected to 12 h of sonication at step #4. We clearly see a loss of the vivid red color in the sample on the left. This suggests that the increased sonication time prior to gold decoration does indeed either further exfoliate or

fracture the xGnP, ultimately resulting in additional gold loading onto the xGnP. Further testing of this hypothesis is needed before any concrete conclusions can be drawn.

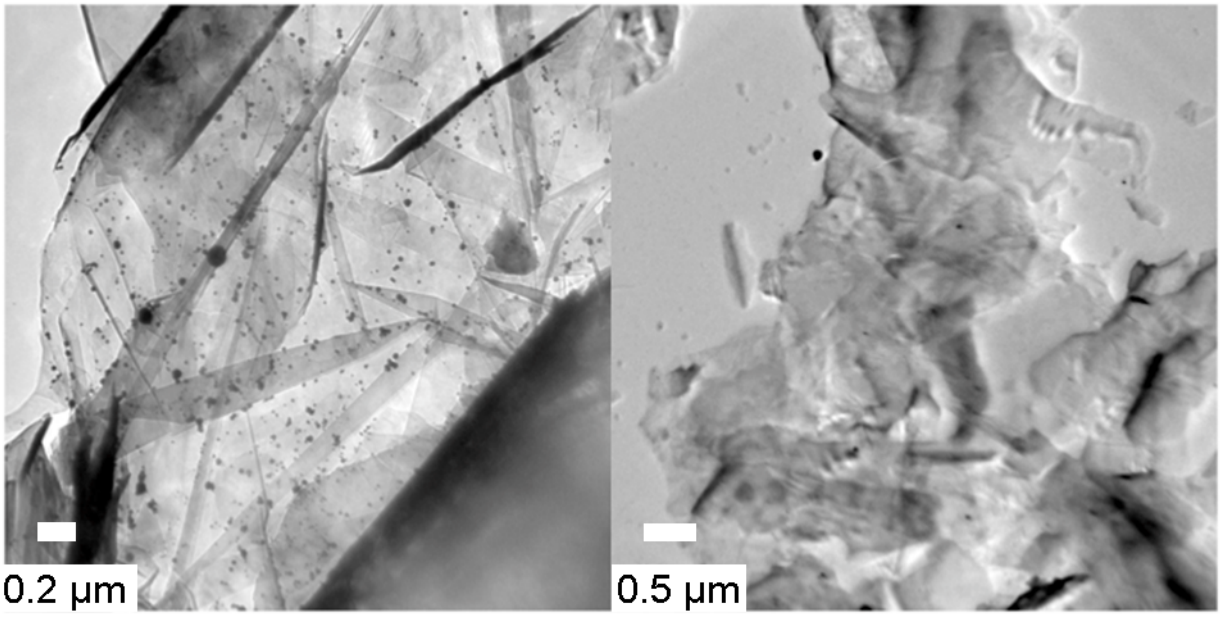

Figure 1.6. Left: TEM image of xGnP-Au after 1 h sonication in NMP. Right: TEM image of xGnP-Au after 12 h of sonication in NMP. We clearly see a loss of gold nanoparticles (particles indicated by the black dots) attached to the xGnP platelet surface in the image on the right.

Figure 1.7. A photographical comparison of the EG waste from two different polyol experiments. The sample on the right was subjected to 1 h of sonication time at step #4 of the preparation method displayed in Figure 1.5 and the sample on the left was subjected to 12 h of sonication at step #4. There is a clear loss of the vivid red color in the sample on the left, suggesting that increased gold loading onto the xGnP particles results from increased time of sonication prior to decoration.

1.5.3. SEM Images

Figures 1.8 and 1.9 display SEM cross sections of xGnP-free polysulfone membranes cast from a solution of 65 wt% N-methyl-2-pyrrolidone, 20 wt% polysulfone, and 15 wt% PEG400 using the wet phase inversion preparation method. Figures 1.10 and 1.11 display SEM cross sections for membranes prepared via the same protocol but loaded with 10% xGnP (weight percent with respect to the polymer). We see a more clearly defined skin layer and a neat, tear drop shaped macrovoids for xGnP-free membranes. xGnP-10% membranes visually appear to have a less uniformly defined skin layer and a less organized macrovoid structure. Additionally, the xGnP particles visually appear to be uniformly dispersed throughout the membrane cross section.

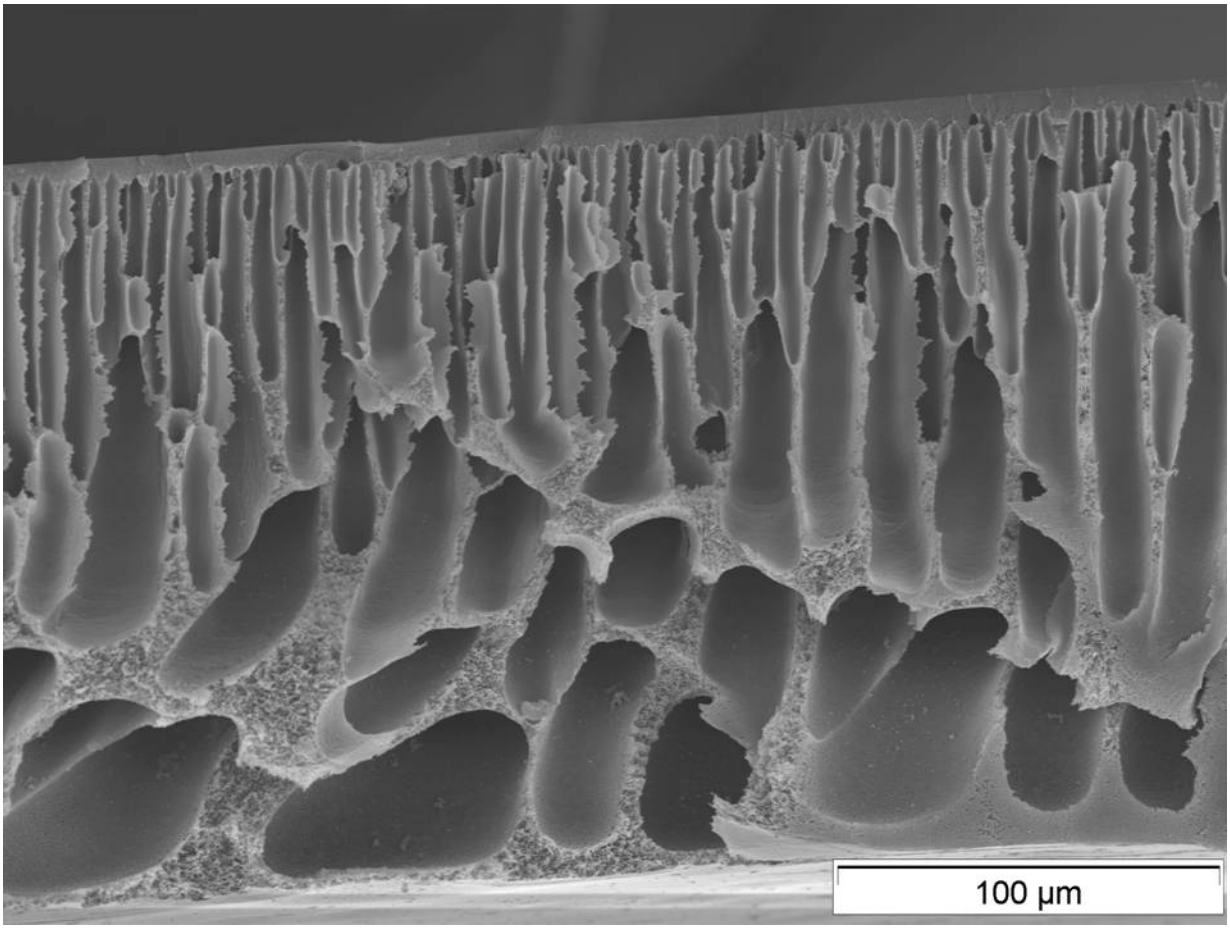

Figure 1.8. A SEM image of a cross-section of a xGnP-free PSf membrane cast from a solution of 65 wt% N-methyl-2-pyrrolidone, 20 wt% polysulfone, and 15 wt% PEG400 using the wet phase inversion preparation method.

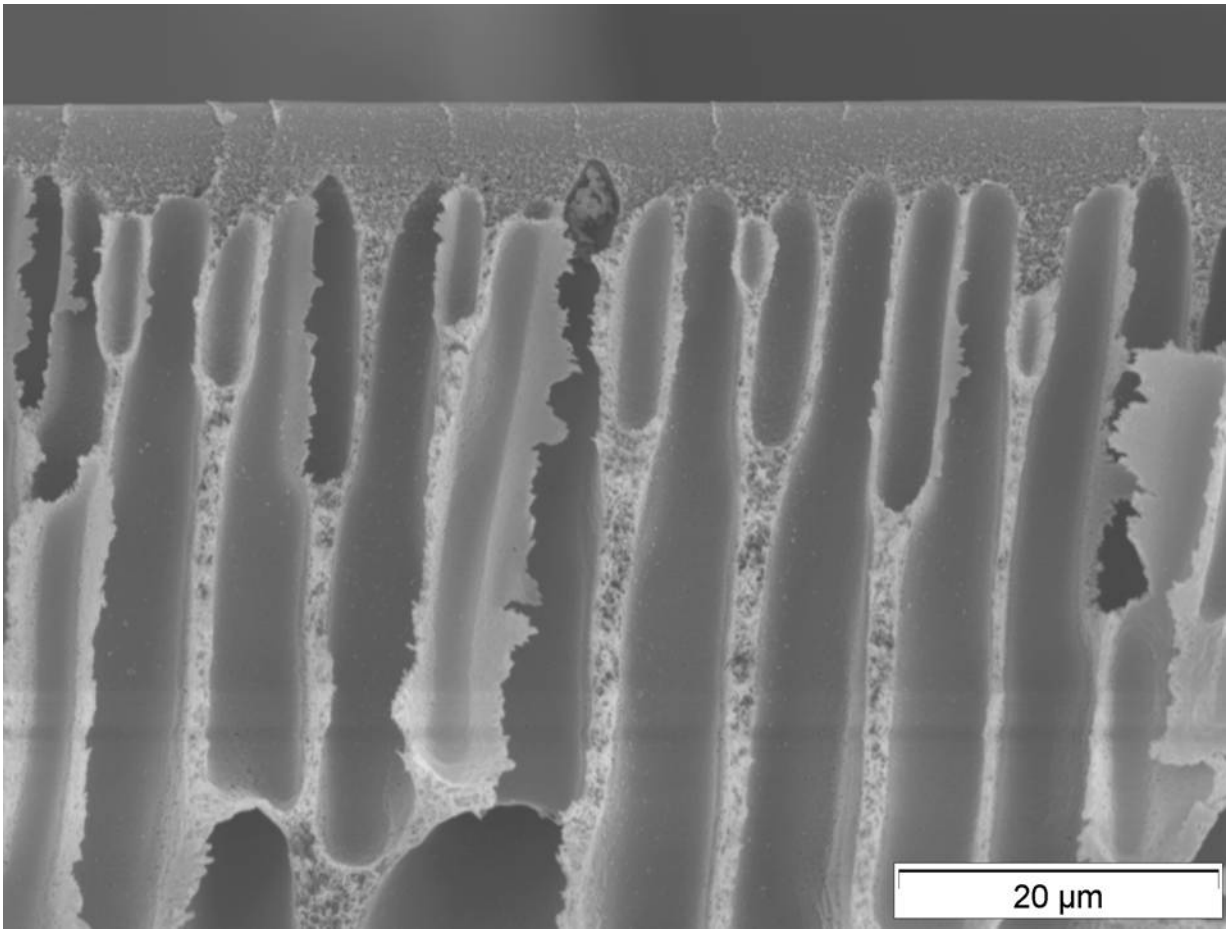

Figure 1.9. A SEM image of a cross-section of a xGnP-free PSf membrane cast from a solution of 65 wt% N-methyl-2-pyrrolidone, 20 wt% polysulfone, and 15 wt% PEG400 using the wet phase inversion preparation method. This is a magnified image of the same coupon pictured in Figure 1.8.

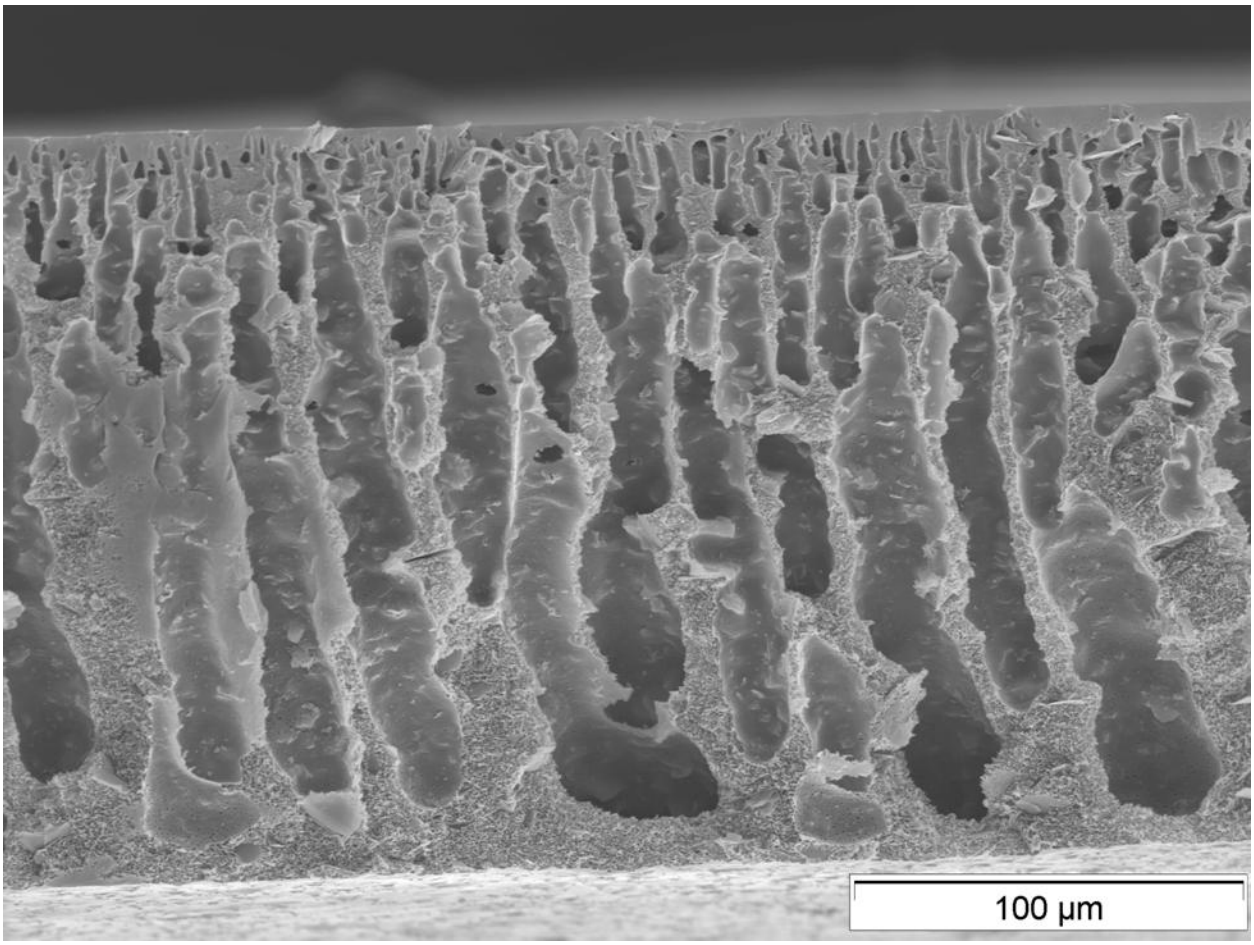

Figure 1.10. A SEM image of a cross-section of a membrane cast from a solution of 65 wt% N-methyl-2-pyrrolidone, 20 wt% polysulfone, and 15 wt% PEG400 loaded with 10% wt of xGnPs using the wet phase inversion preparation method..

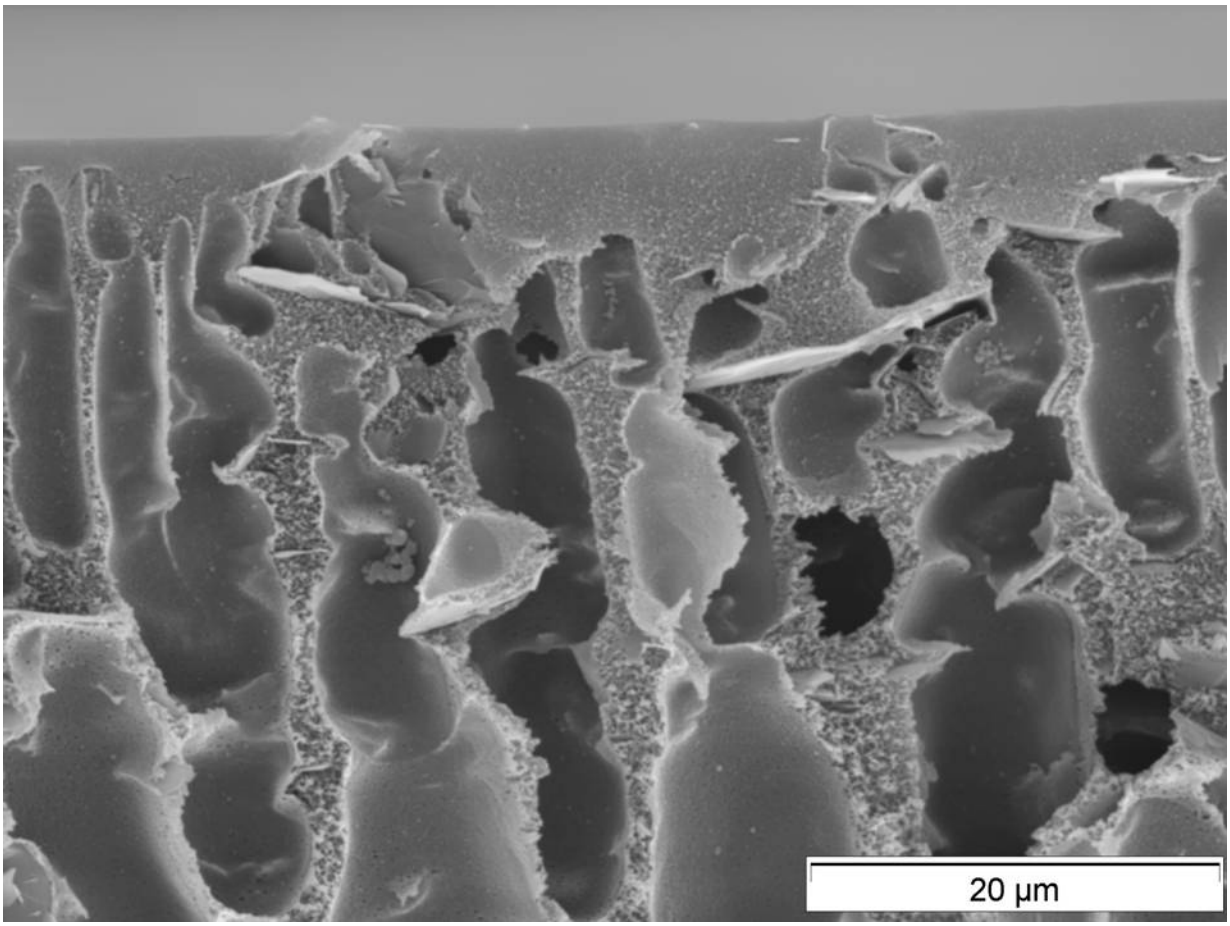

Figure 1.11. A SEM cross-sectional of a xGnP-10% PSf membrane casted from a solution of 65 wt% N-methyl-2-pyrrolidone, 20 wt% polysulfone, and 15 wt% PEG400 using the wet phase inversion preparation method. This is a magnified image of the same coupon pictured in Figure 1.10.

1.5.4. Nanocomposite Membrane Characterization

1.5.4.1. 4-Nitrophenol Reduction Efficiency

All nanocomposite membrane recipes consisted of 65 wt% NMP, 20 wt% PSf, and 15 wt% PEG400. Nanoparticles were added at the loadings of 1, 5, or 10 wt% xGnP or xGnP-Au with respect to the polysulfone. Different nanofiller loadings were used to both increase the percent of 4-NP reduced and as a method to control the structure of the membrane; functionality being controlled by the quantity of gold added to the membrane and structure being controlled by the amount of nanoparticle added.

xGnP-Au membranes proved to be moderately efficient catalytic flow-through reactors when comparing with the results reported using multilayer film membranes [3], [4]. Figure 1.12 displays our experimental results for reaction experiments with xGnP-Au1%, xGnP-Au5% and xGnP-Au10%. Figure 1.13 displays a linearized version of the same results that includes error bars depicting a 90% confidence interval. We see that for xGnP-Au1%, the highest observed percent reduction of 4-nitrophenol was 68%, which was achieved at the lowest permeate flux tested. Additionally, we see that as permeate flux increased, a significant decline in catalytic conversion was observed.

For xGnP-Au5%, the highest obtained percent reduction was 93%. A similar trend was observed when increasing flux through the membrane as with the xGnP-Au1% membranes. The clear inverse proportionality of permeate flux and percent 4-NP reduced suggested that our fabricated membranes were not mass flow limited as were the membranes prepared using the LbL method [4], rather they were reaction limited. If membranes were mass flow limited, we would not see the dramatic decreases in percent reduction at increased fluxes.

The same trend in percent reduction as a function of flux was also observed for xGnP-Au10% membranes, however to a lesser extent. The highest achieved percent reduction with these membranes was 96%. With respect to percent reduction, the performance of these membranes is similar to those reported by Dotzauer et. al [4], who basically achieved 100% conversion. Our membranes however, had significantly lower permeate fluxes, which was a direct function of our fabrication method. This was done purposely however, as this type of membrane is commonly used in commercial and industrial settings.

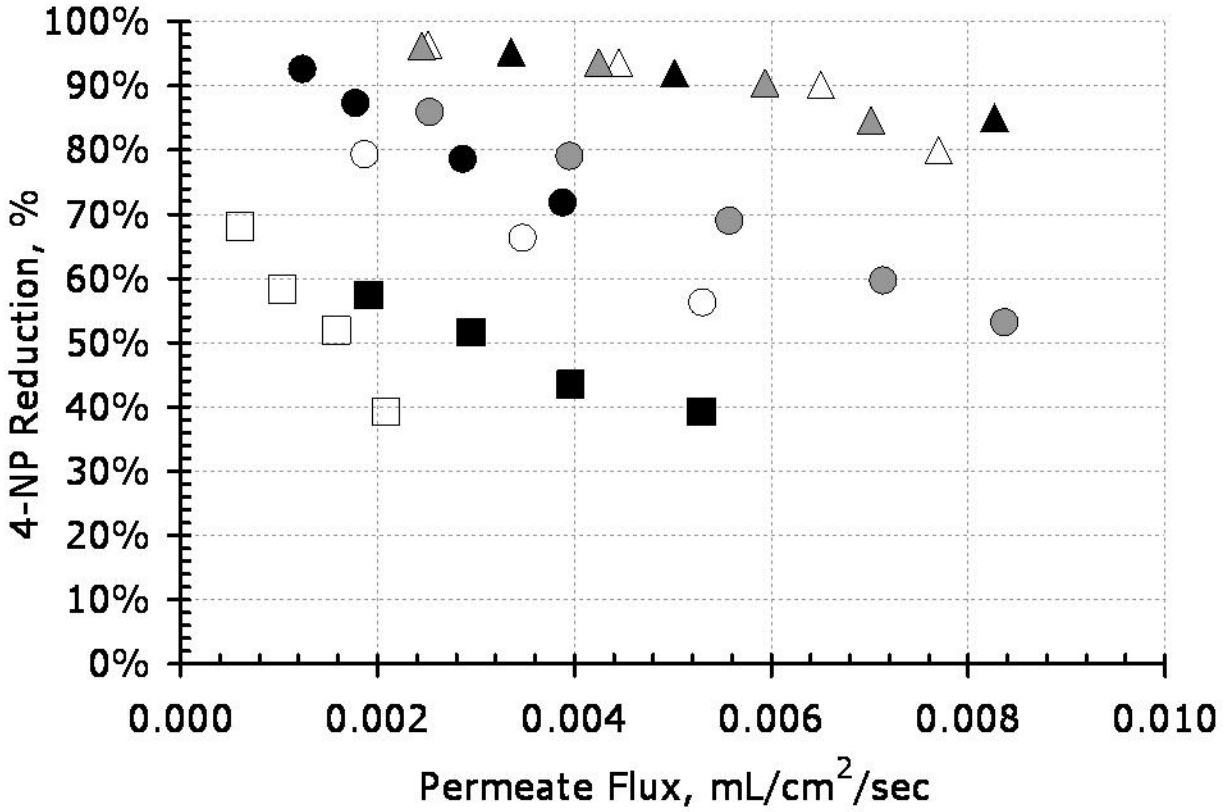

Figure 1.12. Displays the 4-NP reduction efficiency of xGnP-Au membranes as catalytic flow through reactors. Squares, circles, and triangles represent results for xGnP-Au1%, xGnP-Au5% and xGnP-Au10%, respectively. Each filling, shaded, open, shaded, or closed, represents one experimental data set. E.g. closed squares represent one experiment with one xGnP-Au 5% membrane. Increased loading of xGnP-Au catalysts clearly resulted in increased catalytic activity. Permeate flux and 4-NP reduction efficiency appear to have an inversely proportional relationship.

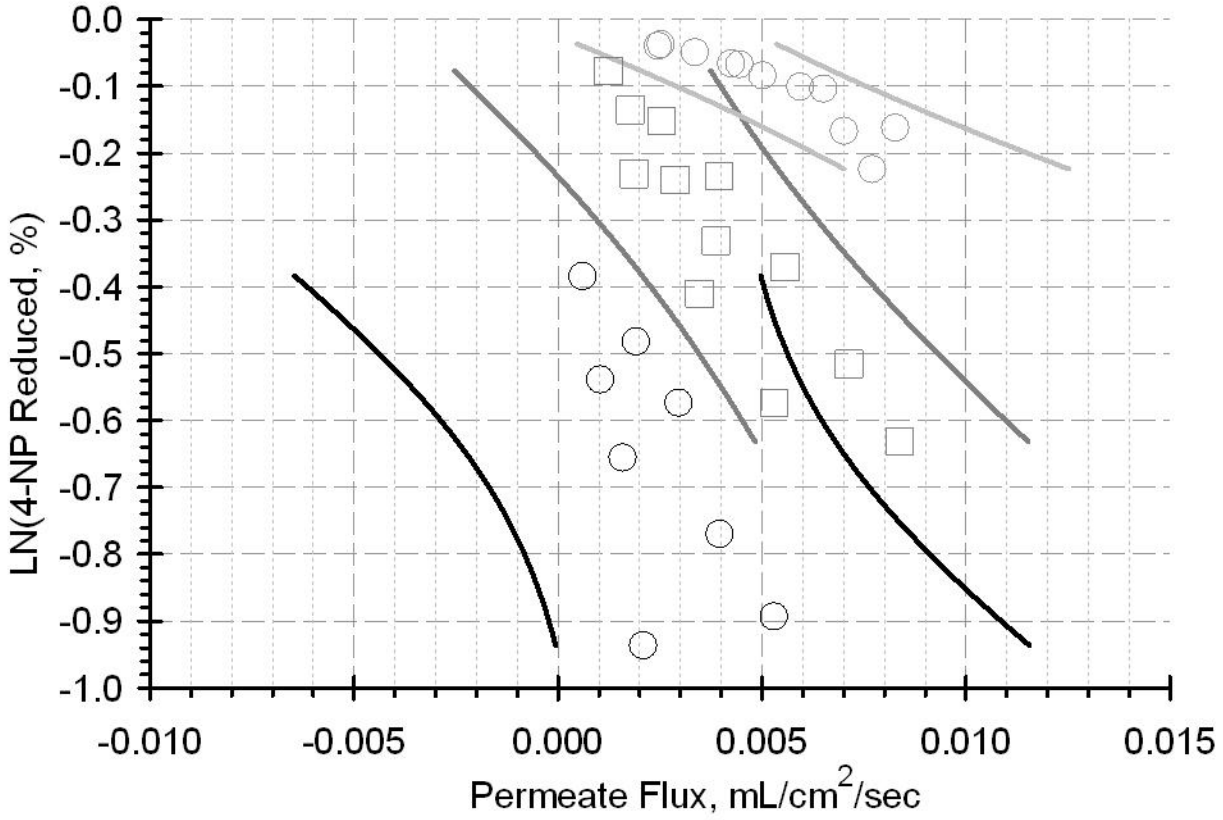

Figure 1.13. Percent reduction of 4-NP for xGnP-Au1%, xGnP-Au5%, and xGnp-Au10%. Black circles, squares, and grey circles represent xGnP-Au1%, xGnP-Au5% and xGnP-Au10%, respectively. Black, dark grey, and light grey lines represent 90% confidence intervals for the log of 4-NP reduction as a function of permeate flux for xGnP-Au1%, xGnP-Au5%, and xGnP-Au10%, respectively.

1.5.4.2. Mathematical Modeling

The first order reaction equation is given as

$$\frac{\partial C}{\partial t} + \frac{\partial uC}{\partial x} + \frac{\partial vC}{\partial y} + \frac{\partial wC}{\partial z} = D_x \frac{\partial^2 C}{\partial x^2} + D_y \frac{\partial^2 C}{\partial y^2} + D_z \frac{\partial^2 C}{\partial z^2} \mp kC \tag{8}$$

where C is concentration, t is time, u, v, and w are the respective velocity components, Dx, Dy, Dz are the respective components of the diffusion coefficient, and k is the reaction constant. In plug flow reactors, advection dominates and we can neglect longitudinal dispersion and diffusion. Further, assuming location-independent velocity u, eq 6 can then be simplified to

$$\frac{\partial C}{\partial t} + u\frac{\partial C}{\partial x} = \pm R \tag{9}$$

where R represents reaction rate: $R = kC$. Integration of eq 9 across the length of the membrane, ℓ,yields

$$C(\ell) = C_o \exp\left(\frac{-k'\ell}{u}\right) \tag{10}$$

where C_o is the concentration in the feed and k' is the first-order rate constant. We made a few assumptions pertaining to our reactor in order to produce k' values that were in turn compared to our observed results. Specifically, we assumed a membrane porosity of 0.7, which is a common value for the type of membrane used in this study [56], and a membrane thickness of 200 μm (determined using SEM). A variety of k' values were then used to solve eq. 10 for a variety of C(ℓ) values. These theoretical

model fits were then compared to our experimental results (Figure 1.14.) Note that each test for a given xGnP-Au loading (e.g. xGnP-Au1%) consisted of a single membrane coupon cut from a membrane sheet. All coupons for a given xGnP-Au loading were cut from a single sheet. When analyzing data presented in Figure 1.14, we see that the reaction constant varies significantly for different coupons from the same membrane sheet, as a single constant does not conform to all data points for a given xGnP-Au loading. This is likely due to local changes in porosity and experimental error.

We expected to see an increase in 4-NP conversion as membranes were loaded with additional xGnP-Au due to increased k values [4]. There should be a linear relationship between gold loading and percent 4-NP reduced if it assumed that all gold is available for reaction [4], meaning that reaction constant for xGnP-Au5% would be 500 percent higher than that of xGnP-Au1%, as gold loading is 5 fold greater. This would be true if we assumed that a) the gold loading per nanoplatelet were constant and b) all gold nanoparticles added to the system were available for reaction. In our system, these assumptions may not hold true. It is fair to assume that the gold loading per platelet was constant; at least for the 1% and 5% loadings, because their preparation procedures were the same, but we cannot say that at increased loadings, gold availability is constant. At increased loading, the xGnp-Au nanoplatelets may be in a more aggregated state, which would result in a lower than expected amount converted, as less gold would be available for reaction. Therefore, we surmise that we did not observe the linear increase in percent reduction as a function of gold loading as report by Dotzauer et al [4] due to membrane morphological differences.

The extracted reaction constants (k') outlined above were for the *entire membrane reactor*; they were not specifically for the xGnP-Au catalyst. If one wished to accurately compare the catalyst prepared in this work to those utilized by others [4], the reaction constant should be normalized by the surface area of the gold nanocatalyst particles. Quantification of these parameters would be difficult for a number of reasons. First, the surface area of nanoparticles would have to be quantified with consideration given to their availability, as it is likely that a fraction of the total particle surface is occluded by the polymer and does not participate in the reaction. The extent of such occlusion in a phase inversion membrane would be difficult to quantify due to membrane complexity and asymmetry. The location of the reaction within the membrane cross-section would also need to be quantified as the inherent properties of an asymmetrical phase inversion membrane likely result in particles located in only portions of the membrane participating in the reaction. Lastly, the quantity of catalyst per membrane should also be identified.

There are two notable drawbacks associated with our approach. First, any future experiments should include an experimental determination of membrane porosity. Second, additional considerations for reactor length should be taken, rigorous determination of which would likely involve quantification of the section of the membrane where the reaction mostly occurs (e.g. membrane skin layer). Furthermore, tortuosity of membrane pores should be taken into consideration.

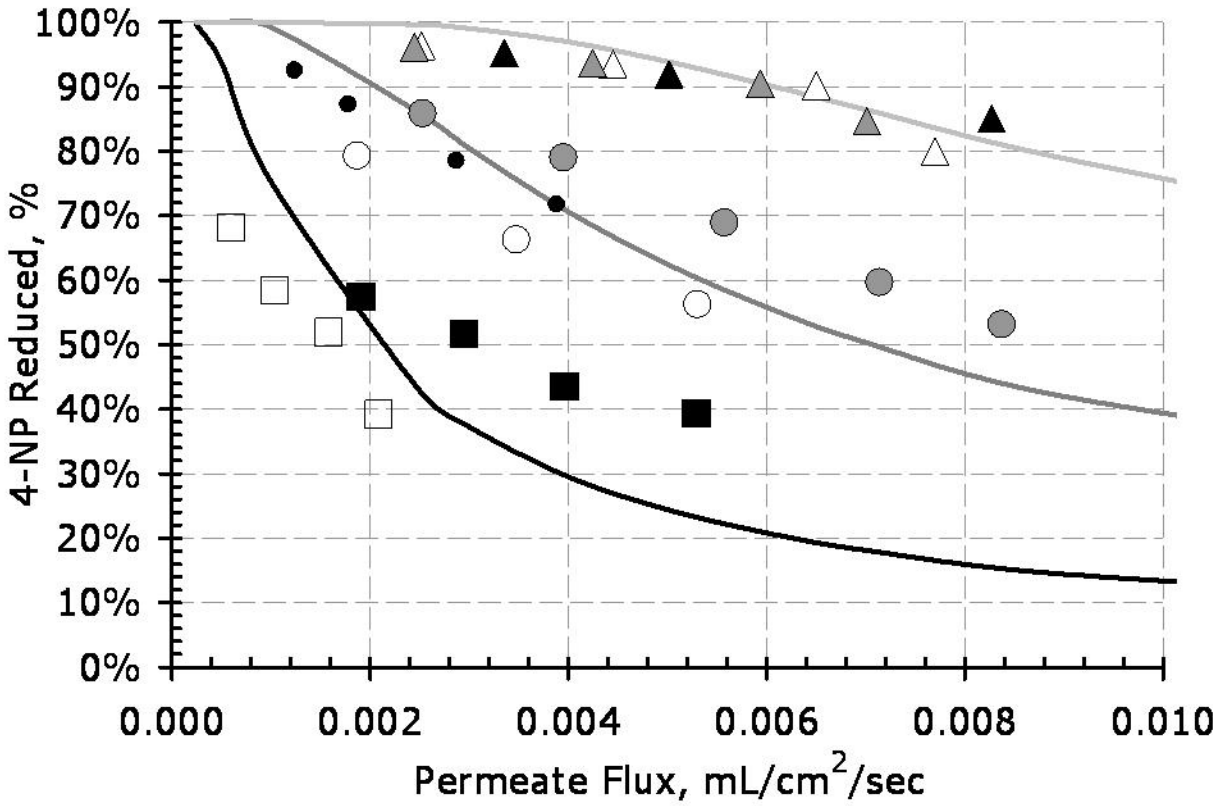

Figure 1.14. Displays results of xGnP-Au reaction experiments. Squares, circles, and triangles represent results for xGnP-Au1%, xGnP-Au5% and xGnP-Au10%, respectively. Each filling, shaded, open, shaded, or closed, represents one experimental data set. E.g. closed squares represent one experiment with one xGnP-Au 5% membrane. The black (—), grey (—) and light grey (—) lines represent fits to the model described in eq. 2 for reaction constants of 0.10, 0.35, and 1.00, respectively.

1.5.4.3. Potential Advantages

Although xGnP-Au membranes did not achieve the near complete conversion reported by a previous study [4], the membranes produced in this study do have some advantages. First, the xGnP-Au membranes were made via immersion precipitation – a method commonly implemented in industrial and commercial practices; the others were prepared using polyelectrolyte multilayer film membranes, which to our knowledge have not been applied in an industrial or commercial setting. It is also important to mention that this system has not been optimized. Further improvements could lead to higher catalytic reactivity. Second, our membranes are unique in the fact that they contain a hierarchical nanoparticle delivery system, which provides the capability of introducing additional nanoparticles to achieve additional functionalities.

1.5.4.4. Future Directions

This study was designed as an initial set of proof-of-concept experiments and a basis for future, more detailed studies. As recently explained by Lightcap et al. [57], there is a demand for creating multifunctional catalysts mats using graphene base nano-architectures. Our method of preparation, the polyol method, can be utilized to decorate the graphene sheets with a variety of different nanoparticles. Therefore, we hope to add additional functionalities to our xGnP-Au membranes by anchoring different nanoparticles to the graphite nanosheets. One such example could be Fe_3O_4, which has been shown to exhibit superparamagnetic properties [58]. These particles could be utilized along with the gold catalysts to preferentially align the graphite sheets within the membrane matrix. This could improve the availability of the catalyst and/or alter the

permeability of the membrane and improve membranes resistance to compaction. An additional example could be the introduction of another catalyst, such as Platinum. One could then have chemical specific catalysts for each component of a multi-contaminant feed solution. A mini proposal that outlines some of the potential implications in more detail can be found in the Appendix.

1.6. Summary

Based on the research and results displayed and discussed above, we can conclude the following:

- A more commercially viable catalytically active flow-through membrane can be easily fabricated at the laboratory scale using the polyol method as the nanocatalyst preparation procedure and phase inversion as the membrane fabrication procedure.
- We successfully demonstrated the ability to fabricate hierarchically structured nanocomposite membranes.
- Gold nanoparticles were well distributed across the nanoplatelets surfaces when prepared via the polyol method.
- Not all gold nanoparticles from the reaction mixture bonded to the xGnP platelets, likely due to a relative shortage of overall bonding sites along the surface of the xGnP particle.
- The introduction of additional functional groups to the perimeter of the xGnP appeared to increase Au bonding onto the carbon nanoparticle.
- If not fully dispersed via sonication, xGnP aggregates got caught in the blade of the membrane casting knife and would precipitously get dragged through the membrane film as it was being cast, creating tears and seams in the membrane sheet. Therefore, proper sonication is critical to producing homogeneous xGnP membranes.
- Extended exposure to sonication appeared to damage xGnP platelets coated with nanoparticles prepared and attached via the polyol method.

- Increased sonication time appears to either further exfoliate, fracture, or create additional functional groups on the xGnP, ultimately resulting in additional gold loading onto the xGnP.
- xGnP-Au membranes proved to be less efficient catalytic flow-through reactors when comparing with the results reported using multilayer film membranes.
- There was a clear inverse relationship between permeate flux and percent 4-NP reduced suggesting that our fabricated membranes were not mass flow limited as were the membranes prepared using the LbL method [4], rather they were reaction limited.
- The performance of xGnP-Au10% membranes with respect to percent reduced was similar to those reported by Dotzauer et. al [4], who achieved >99% reduction. Our membranes however, had significantly lower permeate fluxes, which was a direct consequence of our choice of the fabrication method.
- Our data only partly conformed to the model of a simple first order reaction.

CHAPTER 2

PERFORMANCE OF POLYELECTROLYTE MULTILAYER NANOFILTRATION MEMBRANES UNDER CONDITIONS OF PRECIPITATIVE FOULING

2.1. Background

Synthetic membranes can be divided into two distinct categories: porous and non-porous membranes [59]. In order of largest pore size to smallest pore size, porous membranes can be subdivide into, three categories: microfiltration (MF), ultrafiltration (UF), and nanofiltration (NF). Reverse osmosis (RO) membranes are non-porous while NF membranes may sometimes be classified non-porous (dense), depending on the properties of the particular membrane. Ultrafiltration and microfiltration are generally used to remove particles from fresh water, and to pretreat saline and brackish waters for future treatment by RO [60]. Nanofiltration is often applied to soften ground waters and remove disinfection by-product precursors from surface waters. Reverse osmosis membranes are primarily used in desalination, but can also be used to remove other small molecular weight solutes such as perchlorate, nitrate, nitrite, and synthetic organic compounds [60].

2.1.1. Nanofiltration Membranes

The nanofiltration process is of increasing importance as it offers a comprehensive approach to meeting critical water treatment objectives such as removal of dissolved organic and inorganic molecules [61]. Applications of NF include the treatment of surface water [62][56], agricultural runoff [63], and brackish groundwater [64], among others .

2.1.2. Ultrafiltration Membranes

Ultrafiltration membranes are among the most widely used in industrial and commercial membrane applications; the estimated market value of the US Ultrafiltration market was predicted to reach $900+ million in 2011 [65]. They are frequently used to remove particles from fresh waters [60]. UF membranes have also been advocated as pretreatment for more dense membrane processes like NF and RO, as UF is capable of reducing suspended solids concentrations to the levels needed for NF and RO [60].

2.1.3. Polyelectrolyte Multilayer Film Membranes

Polyelectrolyte multilayer membranes can be prepared by the layer-by-layer (LbL) technique [66]. The LbL method involves the sequential adsorption of polyanionic and polycationic polyelectrolyte layers onto UF or NF membrane supports to create an ultrathin active skin layer that is capable of rejecting divalent ions, among other contaminants [13]. Although this membrane preparation technique is relatively new, this fabrication method has yielded membranes that reject proteins [12], divalent ions [13], [67], and various other foulants. To our knowledge, there are no current commercial applications of such membranes.

2.1.4 PEM Membrane Regeneration

A distinct advantage of PEM membranes is that the PEM layer can be removed and reapplied. The removal is accomplished by exposing the membrane to a high pH solution [68]. The ability to essentially remove and subsequently reapply the active membrane layer (i.e. PEM) could facilitate the successful regeneration of a fouled membrane.

2.2. Precipitation of Inorganic Salts

High levels of inorganic solutes such as calcium, sulfate, bicarbonates, etc. in feed of salt-rejecting membranes often lead to the precipitation of inorganic scale as the concentration of inorganic species near the membrane surface increases due to concentration polarization and can exceed the solubility limit for one or more of sparingly soluble salts such as $CaSO_4$, $CaCO_3$, $BaSO_4$. [50]. Concentration polarization can be described as the formation of a concentration gradient near the membrane surface as a result of full or partial rejection of species by the membrane [69]. Membrane scaling could formally be defined as the precipitation of solids at the membrane surface due to solute concentrations in the feed stream [70]. Through a variety of mechanisms [64], the inorganic scale can effectively reduce the water flux through the membrane surface by as much as 90% [71]. A list of solubility products of sparingly soluble salts of practical concern is shown in Table 2.1. Accordingly, the reduction in scaling propensity of membrane feed solutions is of particular interests to scientists and engineers developing new membrane materials and designing membrane systems.

In order of importance for membrane separations, the sparingly soluble salts are calcium carbonate, calcium sulfate, silica complexes, barium sulfate, strontium sulfate, and calcium fluoride [69]. Formation of calcium carbonate scale can be prevented by acidifying the feed solution [69]. Even if formed, the $CaCO_3$ deposit scale can be relatively simply removed via exposure to acidic solutions, which releases carbon

dioxide [53]. Calcium sulfate is the second most commonly occurring scale [69]. Its precipitation and subsequent fouling of membranes by $CaSO_4$ can be inhibited by the addition of *antiscalants* to the feed water [53]. Antiscalants are polymeric compounds that either prevent scale formation entirely or permit formation of scale that can be removed easily during cleaning [72]. Unlike $CaCO_3$ scale, precipitates of calcium sulfate and other sulfate salts are inherently difficult to remove. If their presence is not detected early, a satisfactory cleaning efficiency is very difficult to achieve [53].

Table 2.1. Solubility products of sparingly soluble inorganic salts of significance in water treatment practice [73].

Salt	**Solubility Product (25^{o}C)**
$CaCO_3$	2.8×10^{-9}
$CaHPO_4$	1×10^{-7}
$CaSO_4$	4.93×10^{-5}
$Ca_3(PO_4)_2$	2.07×10^{-29}
$MgCO_3*3H_2O$	2.38×10^{-6}
$Mg_3(PO_4)_2$	$1.04\ 10^{-24}$
$AlPO_4$	9.83×10^{-21}
$Al(OH)_3$	1.3×10^{-33}
$Ca(OH)_2$	5.5×10^{-6}
$CaHPO_4$	1.0×10^{-7}
$Fe(OH)_3$	2.79×10^{-39}
$FePO_4*2H_2O$	9.92×10^{-29}

Polyelectrolytes are commonly used as antiscalants for inorganic scale in bulk aqueous solutions [74–79]. Various polyelectrolytes have been shown to successfully inhibit the precipitation of gypsum [72][74], calcium carbonate [78], calcium fluoride [76], and calcium oxalate monohydrate [80]. These highly charged molecules (polyelectrolytes) are expected to preferentially adsorb onto the nuclei of precipitating salts and block the active growth sites [79]. A relatively new model describes the process of polyelectrolyte bulk scale inhibition by suggesting that after a certain quantity of the inhibiting polyelectrolyte is removed from the solution via adsorption onto nuclei, a critical inhibitor concentration is reached and crystallization ensues at rates similar to those in absence of inhibitor molecules [81].

In this project we recognize that some of polyelectrolytes used as components of PEM films have been shown to very effectively inhibit crystal growth in bulk solutions [75]. To our knowledge, there has been no studies to-date on the performance of PEM films as nanofiltration membrane skins under conditions of precipitative fouling.

2.3. Hypothesis

We hypothesized that a scale resistant membrane with flux and rejection performances similar to that of NF270 could be fabricated using a combination of PEMs and commercially available UF membranes. NF270 was chosen because it is a commercially available nanofiltration membrane that exhibited similar flux and rejection performance to the PEM membranes that were to be considered in this study. For additional information on NF270 see a previously published article by Manttari et al [76]. The goal of this research was to investigate the flux and rejection properties of PEM nanofiltration membranes when exposed to nearly saturated calcium sulfate solutions.

2.4. Objectives

1. Fabricate PEM membranes using poly(sodium 4-styrene sulfonate (PSS), poly(allyamine hydrochloride) (PAH) and poly acrylic acid (PAA) as constituting polyelectrolytes.
2. Evaluate flux and rejection of these membranes when challenged by an oversaturated solution of calcium sulfate and compare membrane performance with that of commercial NF270 membrane.

2.5. Methods and Materials

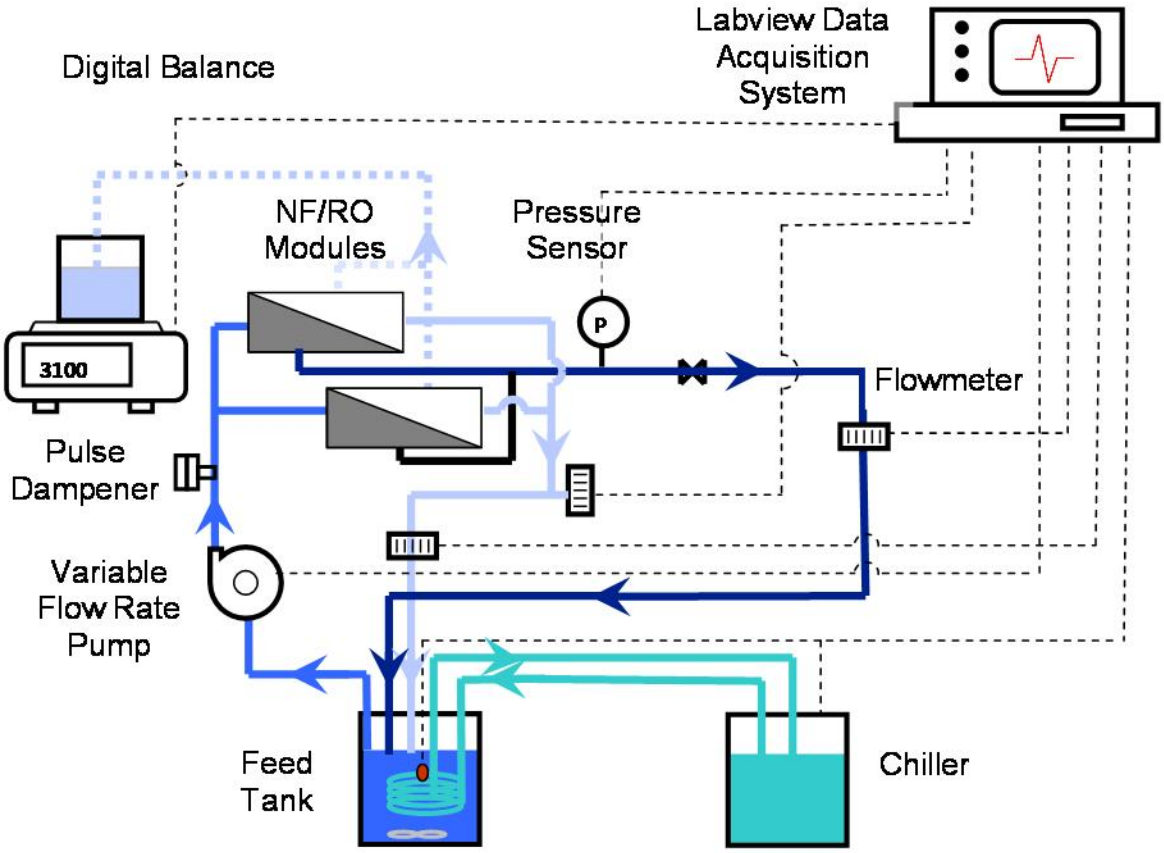

Figure 2.1. Schematic representation of the bench-scale crossflow filtration unit used in this study. The experimental setup was the same as the one utilized by Wang et al. [82].

2.5.1. Experimental Apparatus

A schematic of the bench-scale crossflow system used is shown in Fig. 2.1. Two identical Sepa CF II high-pressure crossflow cells (GE Osmonics, Minnetonka, MN) were connected in parallel. Using two cells in parallel instead of a single unit provided permeate flux volumes within the quantification range of the digital flow meters, whereas this could not always be achieved, at pressures typical for NF, using a single cell. A positive displacement pump outfitted with a flowrate control unit (KBMD-240D, KB Electronics Inc., Coral Springs, FL) and a pulsation dampener (Model H1020V, Bloacoch Fluid Control Inc., Riverside, CA) was employed to deliver the feed solution to the cells. A backpressure valve (BP-3, Circle Seal Controls Inc., Corona, CA) was used to generate the transmembrane pressure. Pressure was monitored using an analog pressure transducer (PX303-500G5V, Omega, Stamford, CT) connected to a computer. An in-line digital flowmeter (Model 101-3, McMilan Co., Georgetown, TX) was used to continuously measure the permeate flux. In all experiments, retentate flow was kept at a constant rate of 2.4 L/min. Retentate flow was calibrated using a stopwatch and a digital mass balance. The crossflow velocity in each cell was 0.25 m/s per cell, which corresponded to a Reynolds number of 487. Data from the analog pressure transducer and digital flowmeters were computer interfaced via a data acquisition module (PCI-6023E/SC-23415, National Instruments Corp., Austin, TX) and an in-house LabView program. The experimental setup and description are the same utilized by Wang et al [82].

Feed solutions were held in a 28.4 L high density polyethylene feed tank (Nalgene Labware, Rochester, NY). Temperature of the feed solutions was maintained

at 20±5 °C using a programmable circulating chiller (Model 9512, PolysScience, Niles, IL) equipped with an external temperature probe and a custom build stainless steel circulation coil. Cooling liquid was composed of equivolume amounts of distilled water and ethylene glycol. Two feed solution concentrations were used; one undersaturated and one oversaturated with respect to gypsum; saturation indices (SI) were 0.91 and 1.5, respectively. The later of the two was used only for a scaling reversibility experiment. In what follows, all experiments should be assumed to be carried out at SI=0.91 unless stated otherwise.

2.5.2. Reagents and Chemical Solutions

All reagents were of ACS analytical grade or higher purity (Fisher Scientific, Pittsburgh, PA) and were used without further purification. The ultrapure water used in the experiments was supplied by a commercial ultrapure water system (Lab Five, USFilter Corp., Hazel Park, MI) equipped with a terminal 0.2 μm capsule microfilter (PolyCap, Whatman Plc., Sanford, ME). The resistivity of water was equal to or greater than 16 MΩ.cm.

2.5.3. Water Characterization

Samples of permeate and feed solutions were manually taken throughout experimentation. Cation and anion concentrations were determined by flame atomic adsorption (Flame AA) and high performance liquid chromatography (HPLC). Calcium samples and standards included 5,000 ppm of lanthanum (as lanthanum chloride heptahydrate) in order to avoid anionic interferences [74]. Sodium samples and

standards included the addition of 2,000 ppm potassium as potassium chloride in order to suppress ionization.

2.5.4. Membrane Supports

Two commercially available membranes were used: NF270 (Filmtech NF270, Dow Chemical Company, Midland, MI) and a 50 kDa UF membrane (PALL Corporation, East Hills, NY). NF270 was chosen as a readily available commercial membrane for comparative purposes. NF270 is a nanofiltration membrane composed of a semi-aromatic piperazine-based polyamide layer on top of a polysulfone microporous support reinforced with polyester non-woven backing layer [83]. The maximum operating temperature is 45 ^{o}C and the maximum pressure tolerance of 41 bar. The pH range for continuous operation is from 3 to 10 (cleaning pH from 1 to 12).

The 50 kDa UF membrane was chosen as the porous support for the polyelectrolyte multilayer films. It should be noted that some research on PEM membranes involved the use of a high flux, brittle alumina support [15], [67]. Given the fragile character of these membranes, it was decided to use a more ductile polymer membrane as a support. 50 kDa membranes were chosen based on the results demonstrated by Malaisamy et al [13] who showed that PES supports of larger pore size may not be fully covered by the polyelectrolytes, resulting in lower solute rejections.

2.5.5. Polyelectrolyte Multilayer Films

Poly(sodium 4-styrene sulfonate) (PSS) MW=70,000, poly(allylamine hydrochloride) (PAH) MW=70,000, and poly(acrylic acid) (PAA) MW=1,800 (Sigma Aldrich, St. Louis,

MO) were used for PEM fabrication. All solutions contained 20 mM polyelectrolyte concentrations and 0.5 M NaCl as the supporting electrolyte, except for the terminating layers, which had 3.0 M NaCl in order to increase surface charge [15][16]. The pH of PSS and PAH solutions used to make PSS/PAH membranes were adjusted to 2.1 and 2.3 [16], respectively. The pH of PSS, PAH and PAA solutions used to make PSS/PAH/PAA membranes was 2.1, 2.3, and 4.5, respectively [67]. The pH of PAA and PAH solutions used to make PAA/PAH membranes was adjusted to pH 7 for both polyelectrolytes in order to produce a thin highly ionized PEM [67]. PEM membranes were fabricated using the layer-by-layer approach. Adsorption times were 2 min for PSS and 5 min for PAH and PAA [15], [16], [67]. Each adsorption step was followed by a 1-min rinse with DI water.

2.5.6. Regeneration

Regeneration of PEMs was performed by soaking the feed side of the fouled membranes in a buffer solution composed of 0.6 M NaHCO3 and 0.06 M Na_2CO_3 for 10 min using an in-house made holder. The pH of the solutions was adjusted to pH 10 using NaOH. In some cases, membranes were backwashed prior soaking in the buffer solution. Backwashing was conducted as follows; 20 L of DI water was prepared in the feed tank, the membrane was inserted into the cell in the upside down position (the support layer of the feed solution), pressure was then applied at an elevated value and the system was allowed to run for 3 min. The PEM was then reapplied and re-tested.

2.5.7. Filtration Protocol

2.5.7.1. Membrane Compaction

It is well known that membranes often exhibit irreversible compaction behavior [11]. At the beginning of each experiment, DI water was filtered through the membrane overnight to fully compact the membrane. This was done to minimize the contribution of compaction to the flux decline during the scaling experiment. The permeate flux value recorded at the end of the compaction stage was used for the membrane resistance calculation.

2.5.7.2. Conditioning

After compacting the membrane overnight, pressure was momentarily released; a 2 L solution of sodium sulfate was prepared, magnetically mixed for approximately 2 min to create a sodium sulfate electrolyte solution, and then added into the feed tank to start the conditioning stage of the experiment. The electrolyte solution was then filtered for 2 h, which was sufficient time for the flux of NF270 to stabilize. The same procedure was followed for the PEM membranes. For further details on the compaction and conditioning stages see Wang et al [82].

2.5.7.3. Scaling

After 2 h of conditioning, the transmembrane pressure was again momentarily released and the 2 L beaker was again filled with the feed solution. Calcium chloride was then added to the solution, which was then stirred for approximately 2 min. The electrolyte was then slowly added to the feed solution, thus initiating the scaling experiment.

2.5.7.4. Experiments on Membrane Fouling by SRNOM solution

Bulk solutions of Suwannee River natural organic matter (SRNOM) were prepared using two separate solutions (see below) that were combined after the conditioning phase. The ionic strength of the solutions was adjusted using NaCl, calcium was added as calcium chloride, and pH was adjusted using NaOH. The first solution prepared contained 10 mM total ionic strength, 1 mM Ca^{2+}, was adjusted to pH 8.2, and contained no SRNOM; this solution was used as the conditioning solution. The second solution prepared was identical to the first, except that it contained SRNOM such that after adding the second solution to the feed tank with the first solution after membrane conditioning, the concentration of SRNOM was 20 mg/L. The solution composition was determined based on previously reported data [84]. Due to the relatively high price of SRNOM, a smaller feed tank was used in order to minimize the total quantity used per experiment. Also, one cell of the unit was shut off in order to compensate for the low feed quantities.

2.6. Governing Equations

The convective flux through microfiltration, ultrafiltration, nanofiltration and reverse osmosis membranes is defined as [11]:

$$J = \frac{\Delta P}{\eta R_m} \tag{11}$$

where ΔP is the applied pressure, η is the dynamic viscosity, and R_m is the membrane resistance. The presence of salts on the feed side of a salt-rejecting membrane creates a solute concentration differential across the membrane that results in an osmotic pressure difference, $\Delta\pi$, between the feed and permeate solutions eq 11 now becomes:

$$J = \frac{\Delta p - \Delta\pi}{\eta R_m} \tag{12}$$

As scale forms on the membrane surface, a portion of the surface is blocked, thus reducing the membrane area available for permeation. Eq 12 then becomes [85]:

$$J = \beta \frac{\Delta p - \Delta\pi}{\eta R_m} \tag{13}$$

where

$$\beta = \frac{A_{free}}{A_{total}} \tag{14}$$

and A_{free} is the unblocked membrane area, A_{total} is the total membrane area, and β is the blockage coefficient. For multicomponent salt systems $\Delta\pi$ can be defined as [86]:

$$\Delta\pi = RT\sum_{0}^{i}\left(C_{im} - C_{ip}\right) \tag{15}$$

where R is the universal gas constant, T is absolute temperature, C_{im} is concentration at the membrane surface, and C_{ip} is the concentration of species i in the permeate.

The boundary layer film model can be used to estimate C_m [11]:

$$J \cdot C + D\frac{dC}{dX} = J \cdot C_P \tag{16}$$

Integration yields

$$\frac{C_m - C_p}{C_f - C_p} = \exp\left(\frac{J\delta}{D}\right) \tag{17}$$

$$k = \frac{D}{\delta} \tag{18}$$

combining (17) and (18) yields

$$\frac{C_m - C_p}{C_f - Cp} = \exp\left(\frac{J}{k}\right) \tag{19}$$

where C_f is the feed solution concentration, δ is the thickness of the boundary layer, D is the ion diffusion coefficient. The mass transfer coefficient k is dependent on the hydrodynamics of the system and, for laminar flow, is given by [85]:

$$k = 1.86\left(\frac{vD^2}{d_h L}\right)^{0.33} \tag{20}$$

where d_h is the hydraulic diameter of the membrane channel, L is channel length and v is flow velocity. Solving eq 19 for C_m yields:

$$C_m = C_p + (C_f - C_p)\exp\left(\frac{J}{k}\right) \tag{21}$$

Osmotic pressure can now be quantified by inserting eq 21 into eq 13.

2.7. Results and Discussion

2.7.1. UF Substrate

Initial experiments using PEM membranes involved deposition of PEM films onto a 10 kDa UF membrane (results not shown). Flux values for the resulting membrane were significantly lower than those for NF270. However, with the same PEM film deposited onto a 50 kDa UF support we were able to achieve specific fluxes and rejections comparable to those of NF 270 membrane. Thus, the 50 kDa PEM membrane was used for all the reported data unless stated otherwise. It is important to note that we did not include a comparison of the bare UF substrate in the proceeding flux, rejection, and scaling analyses. Such a comparison was not necessary because the 50 kDa UF membrane is not a salt rejection membrane.

2.7.2. Evaluation of NF270 Performance Under Conditions of Gypsum Scaling

It was necessary to first establish a baseline performance for the practical evaluation of the PEM membranes. Accordingly, we first tested the flux and rejection properties of a NF270 membrane in experiments where the membrane was challenged with close-to-saturation (SI=0.91) solutions of $CaSO_4$. The performance of NF270 was tested via a simple fouling and hydraulic rinsing procedure. The initial scaling experiment was used as a “probe”, with the goal of locating roughly when and if in the scaling process the membrane was irreversibly fouled. As shown in Fig. 2.2, for the chosen experimental conditions gypsum scale did not appear to irreversibly foul the membrane. The data series from time zero to 2 h represents the first scaling probe. This was followed by a brief 3 min rinse at zero transmembrane pressure using the feed solution at an elevated

crossflow velocity, which was used to simulate a chemical-free flushing procedure. Pressure was then reapplied and another scaling experiment initiated. We see that flux was fully recovered with each rinsing cycle.

In response to the probing experiment carried out at a gypsum SI=0.91, the SI was increased to 1.5 in an attempt to create irreversible fouling conditions. The flux performance decreased more rapidly, as predicted, but the NF270 membrane did not irreversibly foul (results not shown). These results were consistent with those obtained for other polyamide NF membranes [87]. We can thus conclude that gypsum scale alone did not appear to irreversibly foul an NF270 membrane.

Interestingly, we did not observe the same trend for PEM-coated membranes. Although the initial flux was in some cases recovered, the slope of the flux curve after a rinse was markedly higher than that of the initial curve (see Fig. 2.3). This could be explained by the fact that polyelectrolytes preferentially adsorb onto active crystal growth sites [77]. In addition, the negatively charged surfaces of the terminating layer [15], [88] have also been suggested to contain strong chelating properties with respect to an oppositely charged ion [89] (i.e. calcium and/or sodium; calcium is divalent so it's chelating affinity is greater than that of sodium). Therefore, the observed results could be the product of a PEM film that is both bonded to the polymer substrate as well as the gypsum scale. When rinsed, the bulk of the gypsum scale is likely removed, but small crystals and/or nuclei likely remain bonded to the PEM surface. This residual mineral scale provides growth sites for the second scaling experiment, thus increasing the crystal growth propensity and more rapidly decreasing the permeate flux.

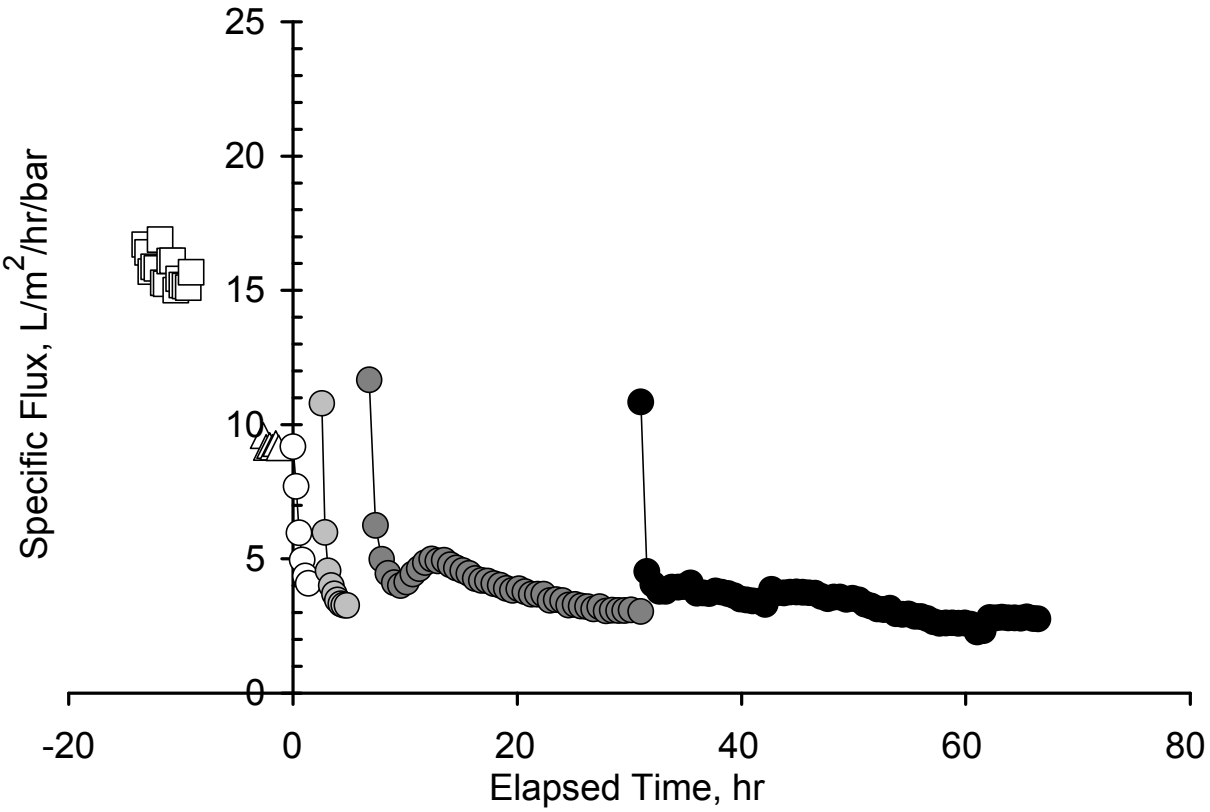

Figure 2.2. Specific flux through NF270 membrane in a fouling experiment designed to test the reversibility of $CaSO_4$ scale. Squares represent the compaction stage, triangles represent the conditioning stage, and circles represent the scaling experiments. Circular shape symbols of different shades of gray represents different scaling "probes". The membrane was repeatedly scaled with $CaSO_4$ and rinsed with DI water in order to test the irreversibility of gypsum scaling.

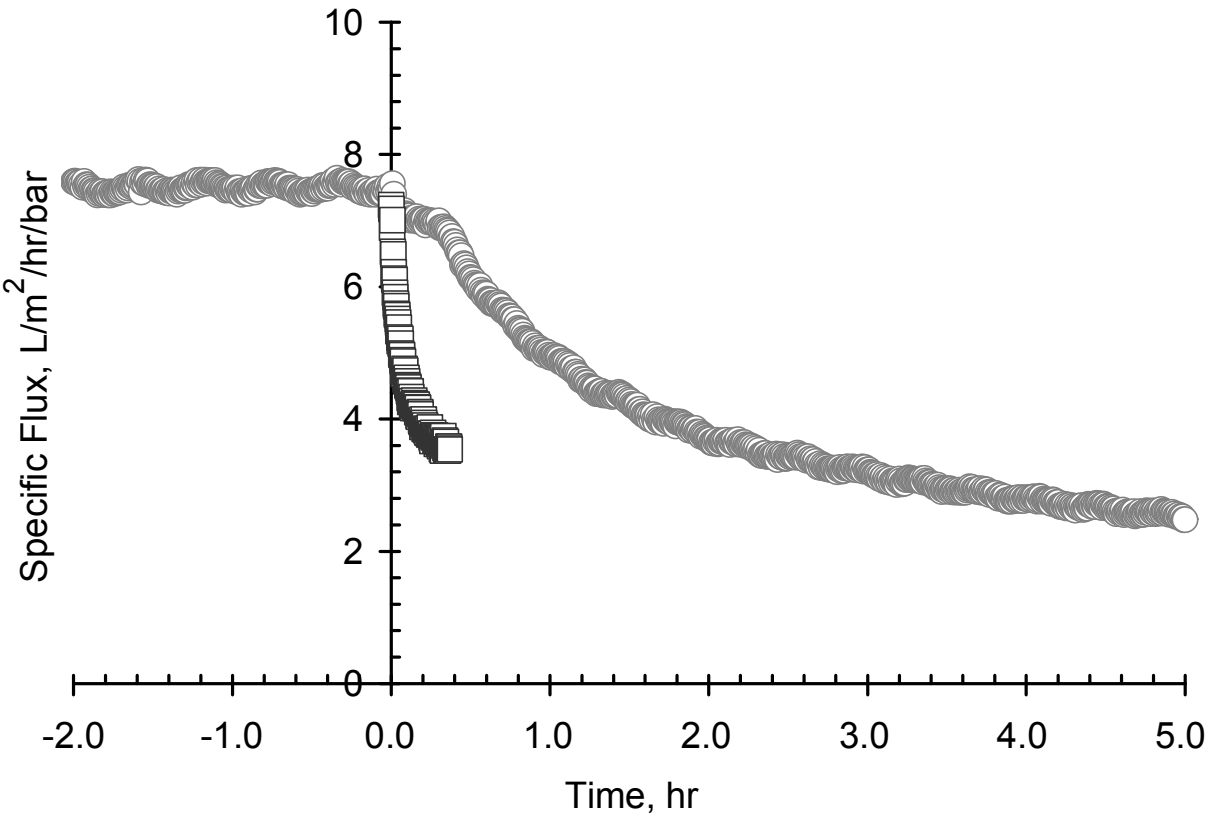

Figure 2.3. Initial flux profile (-○-) during a scaling experiment of NF270+$(PSS/PAH)_3$-(PAA) scaled by calcium sulfate with a feed solution saturation index of 0.9 and the initial scale profile (-□-) of the same membrane after being and rinsed with DI water.

2.7.3. Fouling

With a $(PSS/PAH)_{4.5}$ film deposited on a 50 kDa support we observed higher specific fluxes but lower overall rejections than those observed for NF270 (Fig. 2.4 and Fig. 2.5). The higher specific flux of UF+$(PSS/PAH)_{4.5}$ could be partially explained by the notable initial rejection differences between the NF270 and the composite PEM membrane (see Table 2.2). The elevated rejections of the NF270 lead to increased concentration polarization and osmotic pressure, thus decreasing the specific flux. Therefore, although the pure water flux of NF270 and UF+$(PSS/PAH)_{4.5}$ are markedly similar (see Fig. 2.6) the differences in rejection result in different specific fluxes.

A modified PEM membrane containing PAA, a demonstrated effective gypsum scale bulk inhibitor [77], was also used with the intention of creating a scaling resistant membrane. Low molecular weight PAA was used, as it has been shown that, crystallization induction time decreases with increasing molecular weight for this particular polyelectrolyte [77]. PAA was used only in the terminating layer; the bulk components of the PEM were unchanged because PAA is known to be a relatively dense PE and typically produces PEMs of relatively low water permeability [67]. The $(PSS/PAH)_4$-PAA membrane resulted in a ~25% increase in membrane resistance (see Fig. 2.6) and a ~10% increase of monovalent and divalent ion rejections (Fig. 2.5 and Fig. 2.7). Although slightly denser than NF270, this membrane produced very similar rejections, with the exception of sulfate, which was ~25% percent lower. This could be the result of the superior size exclusion capabilities of NF270, as PEMs are known to be dependent on Donnan exclusion as a part of their removal mechanism [15], [90].

PEMs were also fabricated using NF270 as a support. Two different PEMs were evaluated; $(PSS/PAH)_3$-(PAA) and $(PAA/PAH)_{3.5}$. In order to minimize increases in membrane resistance only three layers of the bulk polyelectrolytes were used. In both instances we observed a ~10% increase in ionic rejections (Fig. 2.8 and Fig. 2.9). For NF270+$(PSS/PAH)_3$-PAA the increase in rejection was coupled with a mild increase in resistance. For NF270+$(PAA/PAH)_{3.5}$, membrane resistance remained unchanged. The increase in rejections is likely the result of increased Donnan exclusion, which is believed to be an important salt rejecting mechanism of PEMs [17].

A negatively charged polyelectrolyte was always used as the first bi-layer when preparing NF270-PEM membranes; PSS, PAA and NF270 [83] are all negatively charged. Electrostatic forces are often the main driving force for attraction between surface charges and charged groups along the polyelectrolyte backbone [91]. Additionally, it has been suggested that polyelectrolyte adsorption to similarly charged surfaces only occurs when the non-electrostatic affinity is sufficient to overcome the electrostatic repulsion and entropic penalty of adsorption [91]. We did not evaluate the non-electrostatic affinity of PSS and PAA to the surface of NF270 membranes. Therefore, future studies should ensure adequate affinity exists between polyelectrolytes and surfaces of similar charge.

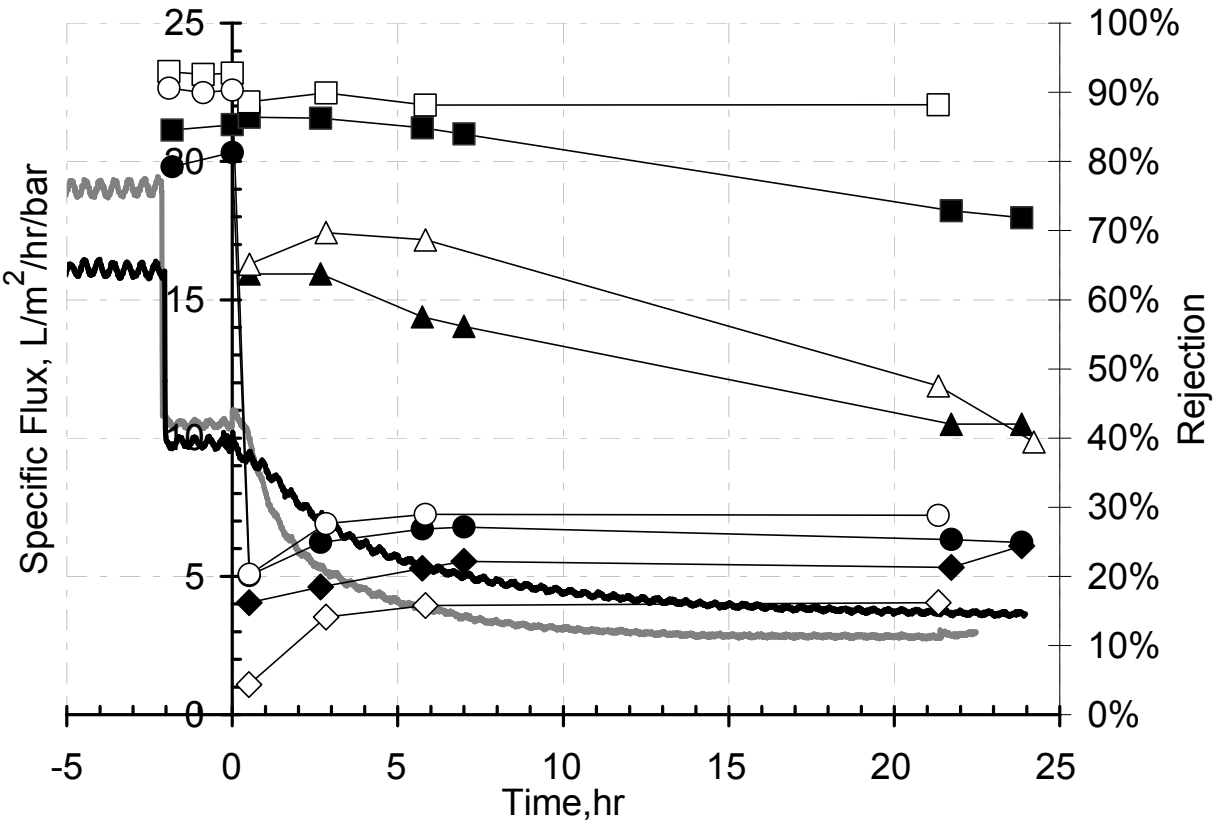

Figure 2.4. Flux and rejection performance data of two NF270 membranes scaled by calcium sulfate with a feed calcium sulfate saturation index of 0.9. The solid black line and the filled symbols denote flux and rejection values, respectively, for one data set. The grey line and open symbols denote a replicate dataset. Squares, triangles, circles, and diamonds represent denote sulfate, calcium, sodium and chloride rejections, respectively.

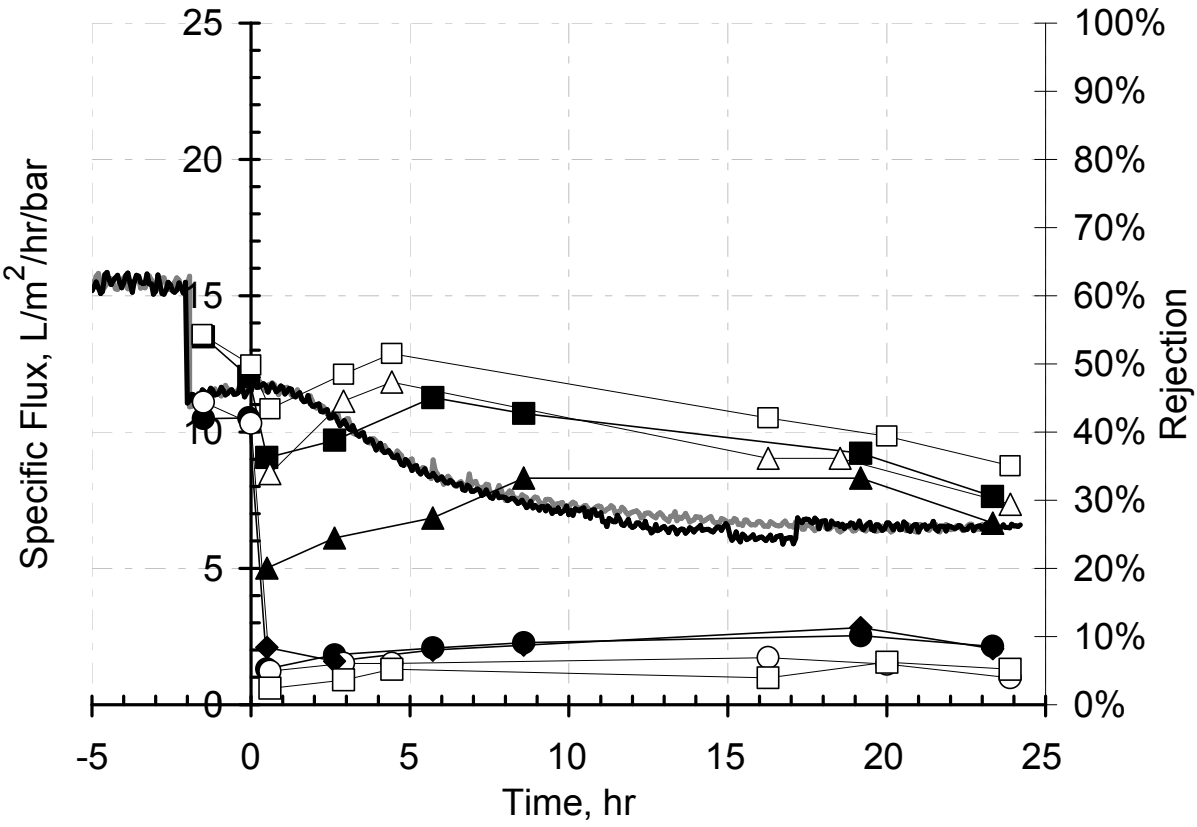

Figure 2.5. Flux and rejection performance of two UF+$(PSS/PAH)_{4.5}$ membranes scaled by calcium sulfate with a feed solution saturation index of 0.9. The solid black line and the filled symbols denote the flux and rejection, respectively, for one data set. The grey line and open symbols denote another. Squares, triangles, circles, and diamonds represent denote sulfate, calcium, sodium and chloride rejections, respectively.

Table 2.2. Comparison of initial rejection performance of NF270 and UF+$(PSS/PAH)_{4.5}$.

	MEMBRANE	
ION	**NF270**	**UF+$(PSS/PAH)_{4.5}$**
Sulfate	~87%	~45%
Calcium	~65%	~30%
Chloride	~20%	~10%
Sodium	~15%	~10%

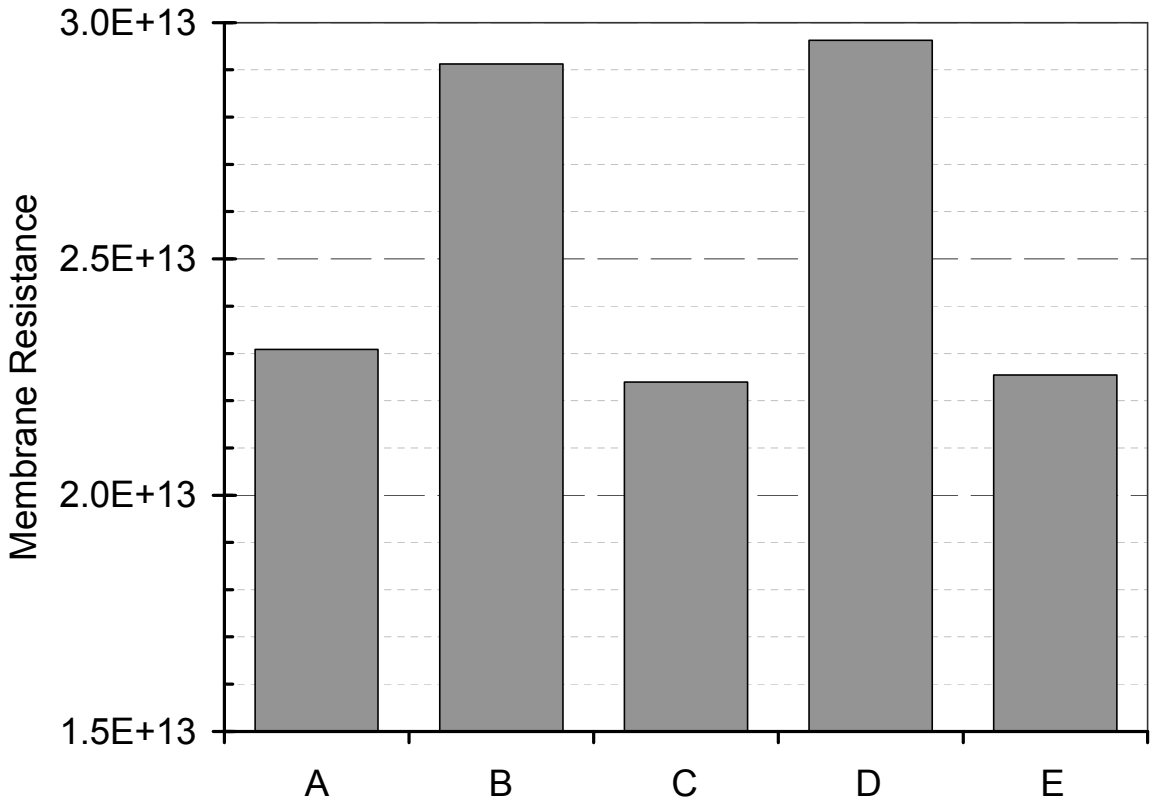

		Bulk Layer pH		Final layer pH	Salt Content (M)	
Membrane	ID	Polyanion	Polycation	Polyanion	Bulk Layer	Final layer
UF+$(PSS/PAH)_{4.5}$	A	2.1	2.3	2.1	0.5	3.0
UF+$(PSS/PAH)_4(PAA)$	B	2.1	2.3	4.5	0.5	3.0
NF270	C	n/a	n/a	n/a	0.5	3.0
NF270+$(PSS/PAH)_3(PAA)$	D	2.1	2.3	4.5	0.5	3.0
NF270+$(PAA/PAH)_{3.5}$	E	7	7	7	0.5	3.0

Figure 2.6. Membrane resistance data and membrane composition information for the NF270 and PEM membranes considered in this study.

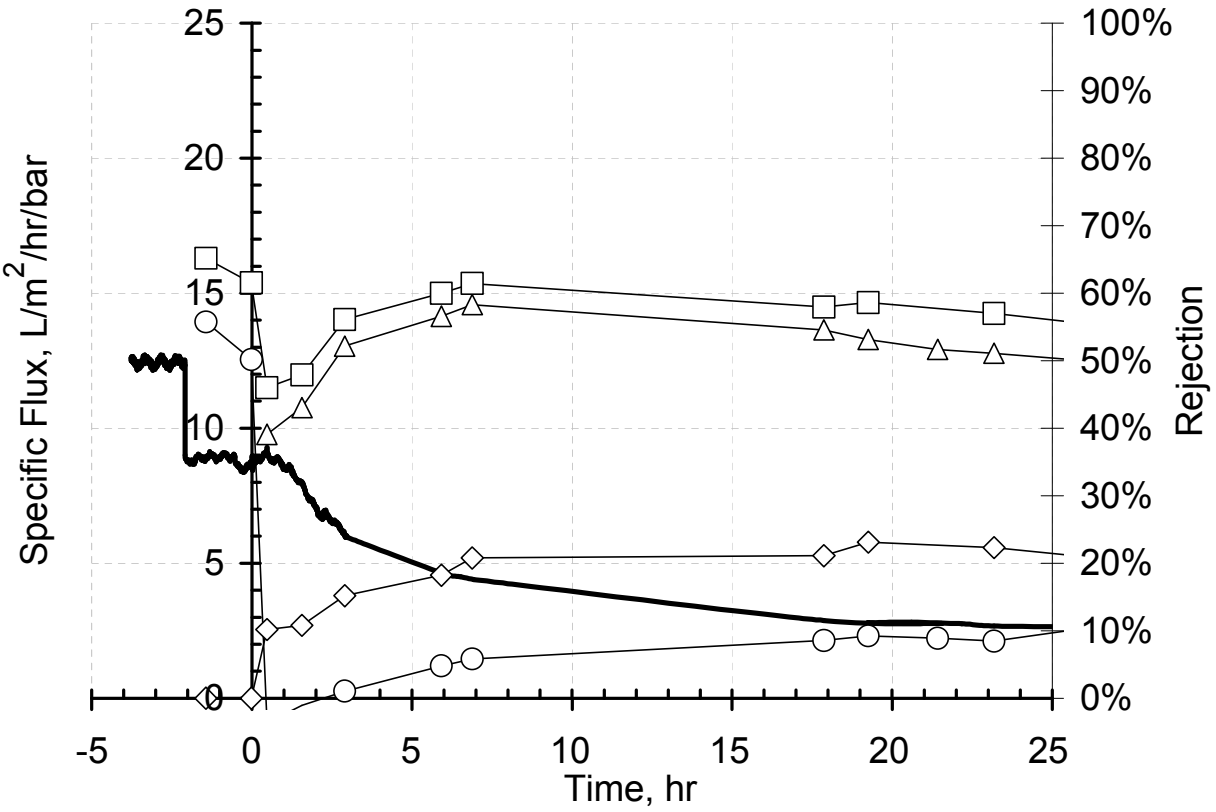

Figure 2.7. Flux and rejection performance of UF+(PSS/PAH)$_4$-(PAA) scaled by calcium sulfate with a feed solution saturation index of 0.9. The solid black line and the open black symbols denote the flux and rejection, respectively. Squares, triangles, circles, and diamonds represent denote sulfate, calcium, sodium and chloride, respectively.

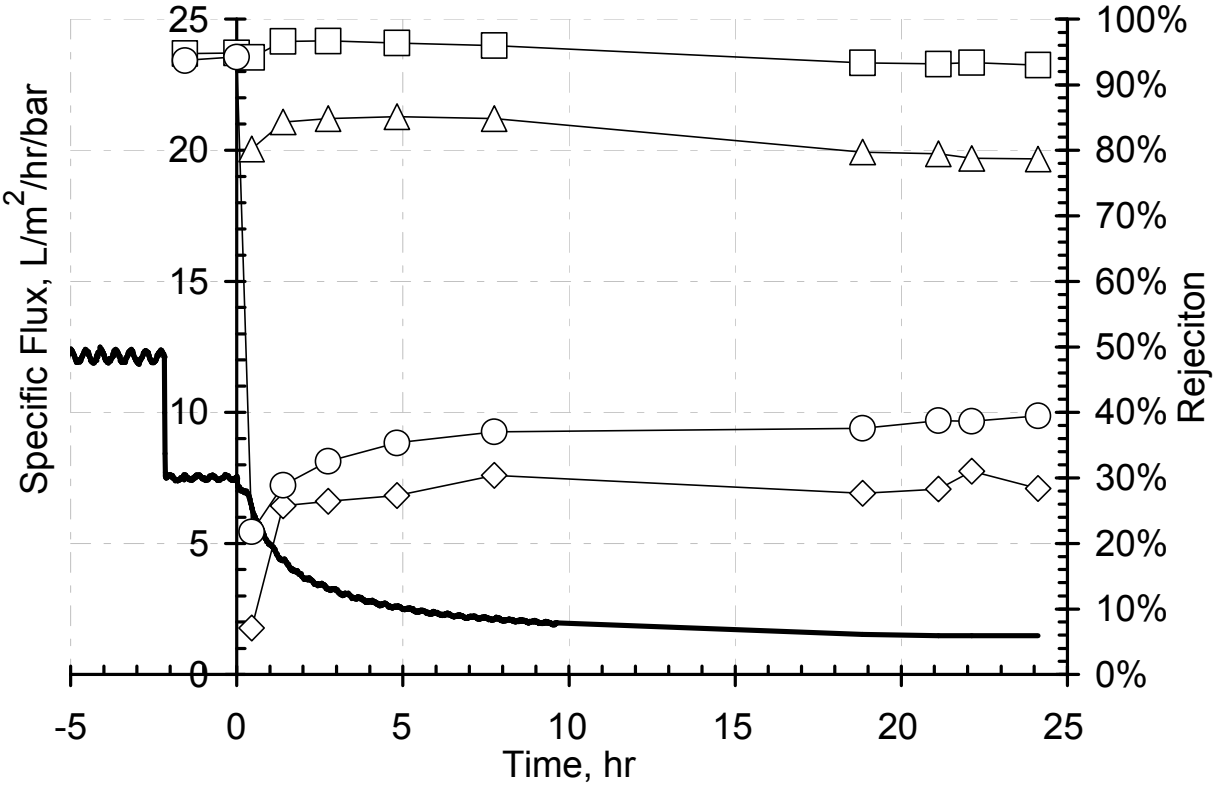

Figure 2.8. Flux and rejection performance of a NF270+$(PSS/PAH)_3$-PAA membrane scaled calcium sulfate with a feed solution saturation index of 0.9. The solid black line denotes flux. Squares, triangles, circles, and diamonds represent denote sulfate, calcium, sodium and chloride rejections, respectively.

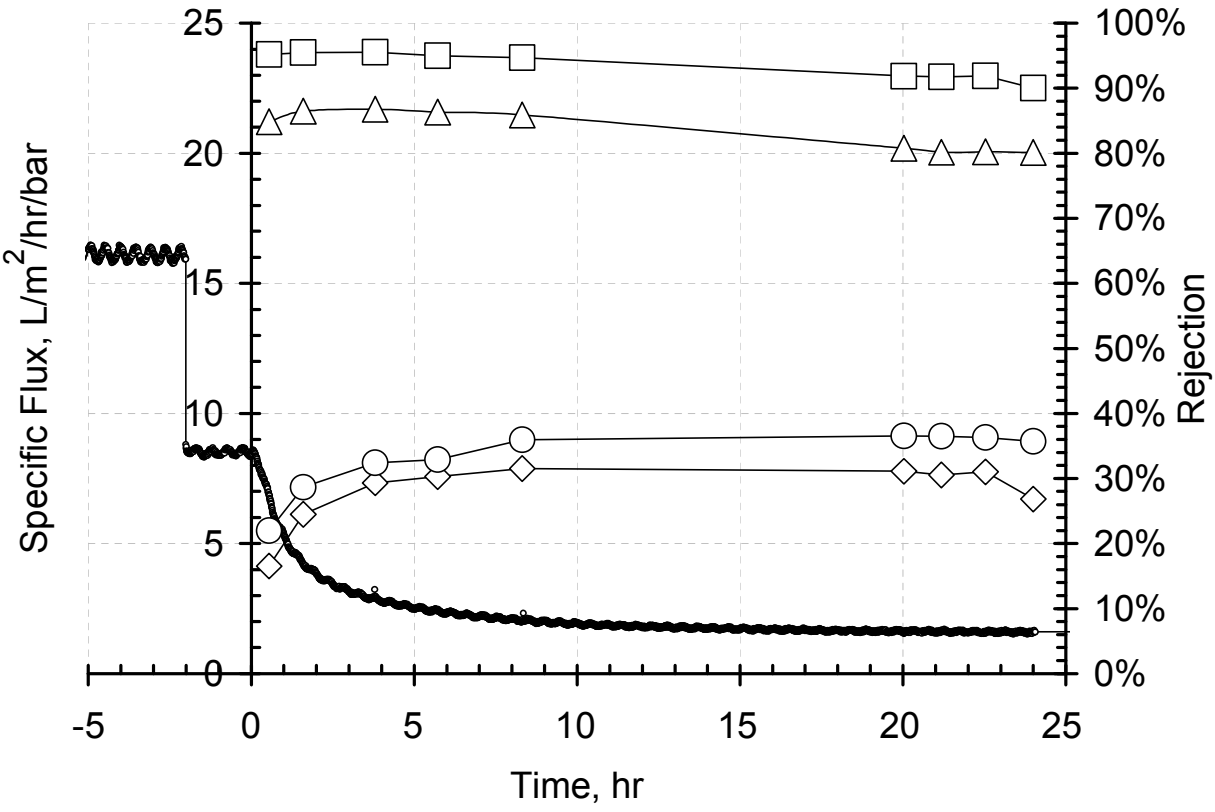

FIgure 2.9. Flux and rejection performance of NF270+$(PAA/PAH)_{3.5}$ scaled by calcium sulfate with a feed solution saturation index of 0.9. The solid black line denotes flux. Squares, triangles, circles, and diamonds represent denote sulfate, calcium, sodium and chloride rejections, respectively.

2.7.4. Surface Blockage

Solving eq. 13 for β, the amount of surface blockage and the surface saturation indices for all the considered membranes were calculated and plotted as a function of time (Fig. 2.10-2.14). This was done to evaluate the antiscaling potential of the PEMs. We see that surface blockage is inversely related to flux and that surface saturation indices are initially quite high, as a result of concentration polarization, but decrease with time as scale precipitates, which reduces the amount of ionic calcium and sulfate present in the boundary layer. The results suggest that the PEMs considered did not act as antiscaling membranes. A possible explanation for this could be the relatively small amounts of PEMs adsorbed on the membrane surface. Although minute amounts of polyelectrolytes have been shown to effectively inhibit bulk calcium sulfate crystallization [66], they've also been shown to induce nucleation of calcium phosphate [89], [92]. The polyelectrolytes induced nucleation of calcium phosphate only at low concentrations and proceeded to inhibit nucleation after a certain concentration threshold is passed [92]. We could be witnessing a similar effect with calcium sulfate.

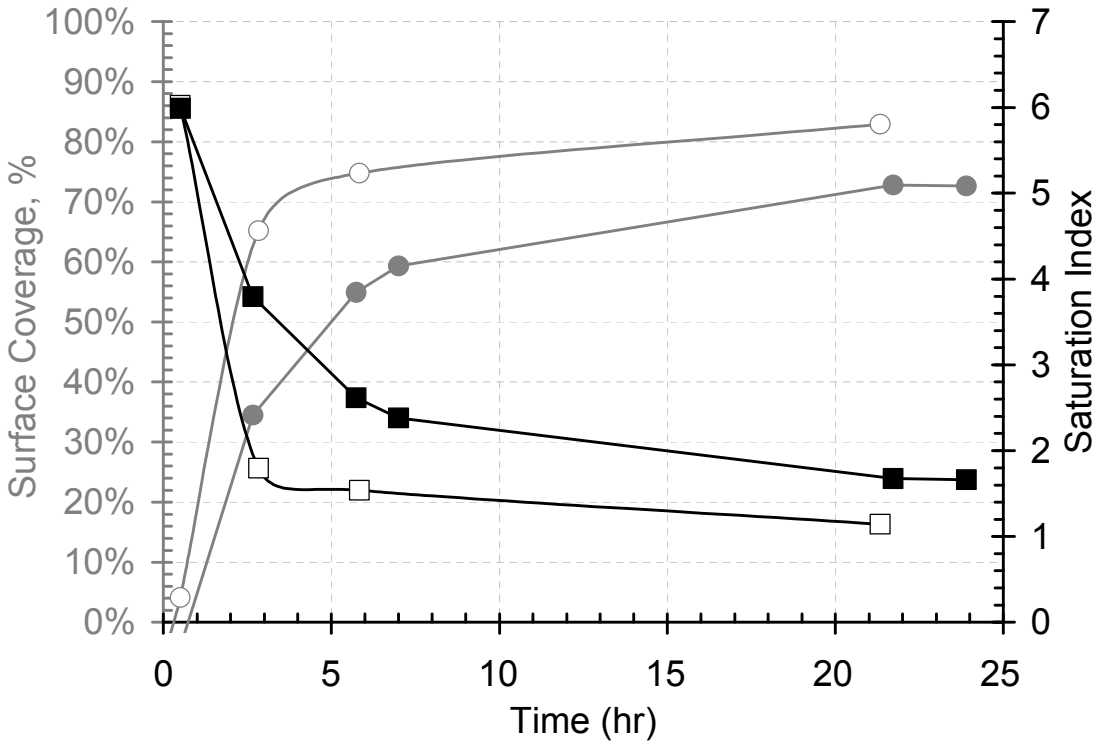

Figure 2.10. Calculated surface blockage and surface saturation index as a function of time for two NF270 membranes scaled by calcium sulfate with a feed solution saturation index of 0.9. The open and closed symbols delineate the two data sets displayed.

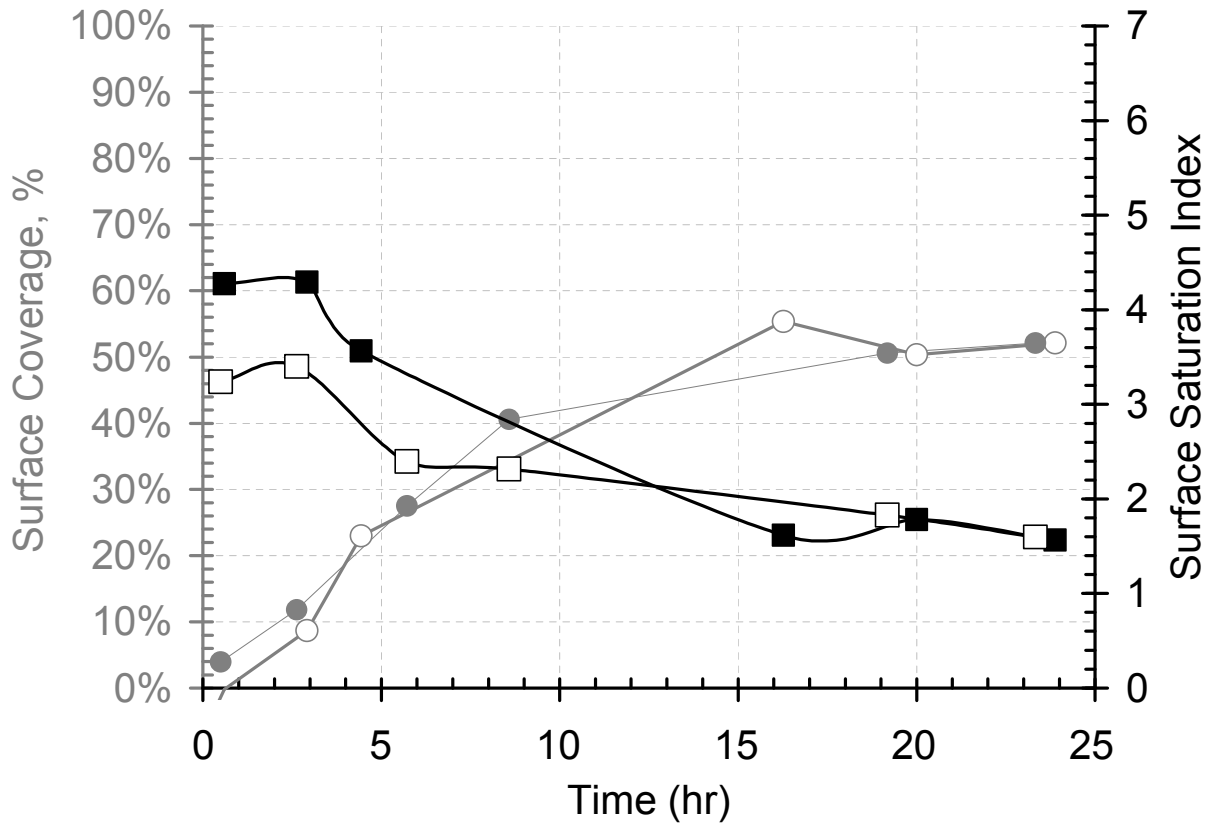

Figure 2.11. Calculated surface blockage and surface saturation index as a function of time for two UF+$(PSS/PAH)_{4.5}$ membranes scaled by calcium sulfate with a feed solution saturation index of 0.9. The open and closed symbols delineate the two data sets displayed.

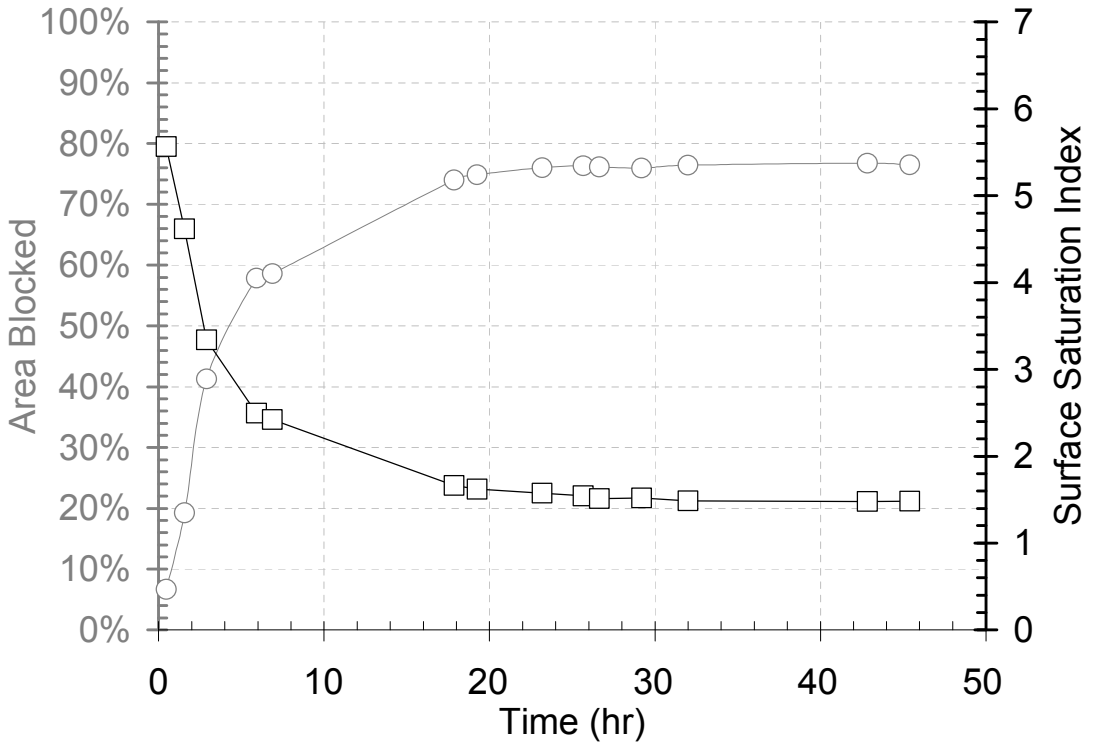

Figure 2.12. Calculated surface blockage and surface saturation index as a function of time for a UF+$(PSS/PAH)_4$-PAA membrane scaled by calcium sulfate with a feed solution saturation index of 0.9.

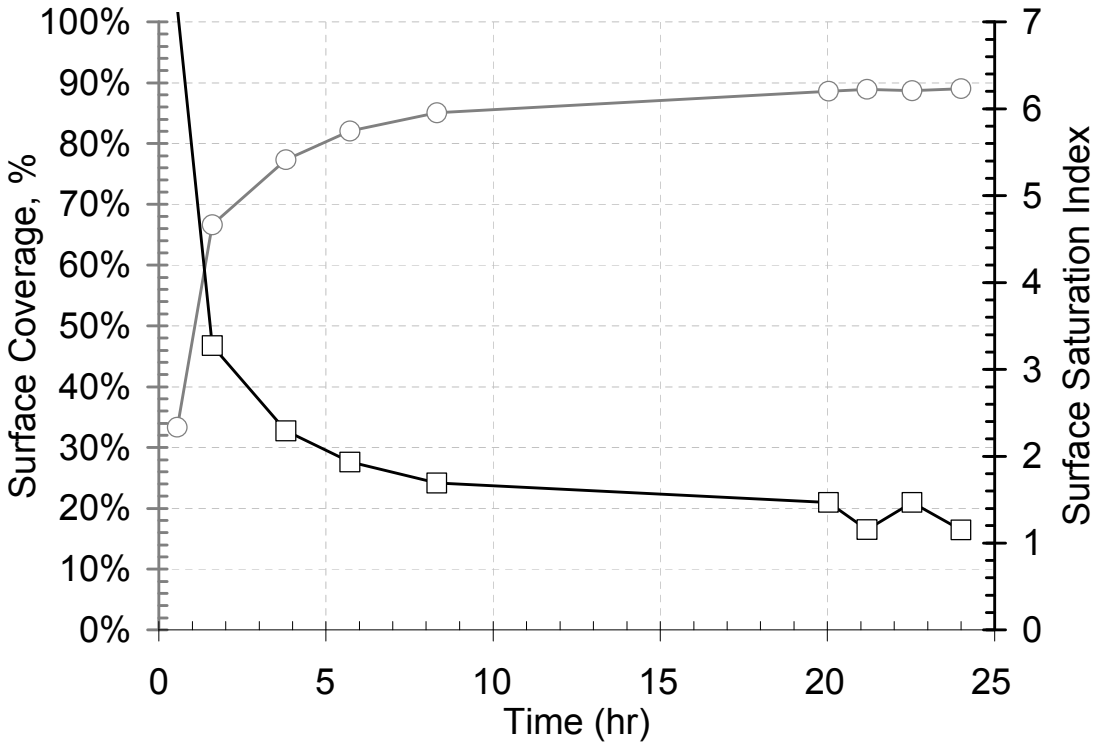

Figure 2.13. Calculated surface blockage and surface saturation index as a function of time for a NF270+$(PAA/PAH)_{3.5}$. membrane scaled by calcium sulfate with a feed solution saturation index of 0.9.

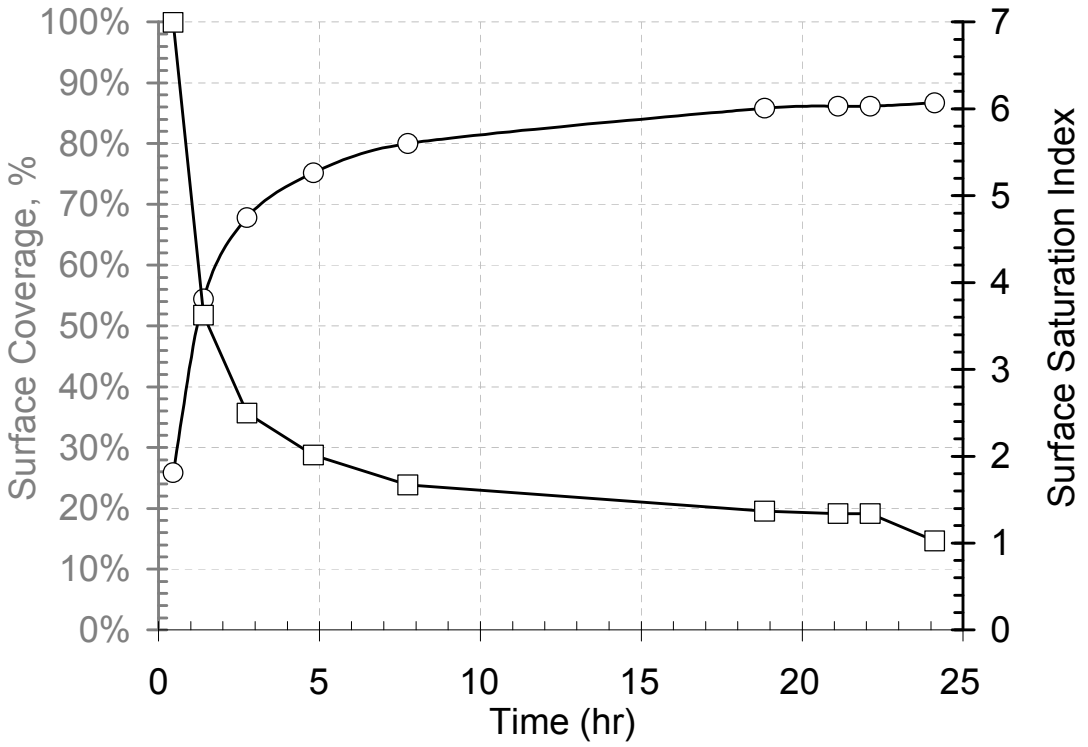

Figure 2.14. Calculated surface blockage and surface saturation index as a function of time for a NF270+$(PSS/PAH)_3$-PAA membrane scaled by calcium sulfate with a feed solution saturation index of 0.9.

2.7.5. Regeneration

Previous research has shown that PEM films can effectively dissociate from their supports via exposure to high ionic strength salt solutions [68]. In order to test the regeneration capabilities of the fouled $(PSS/PAH)_{4.5}$ membrane coupons were backwashed and/or exposed to a high pH sodium bicarbonate solution. Neither soaking in the buffer solution alone, nor backwashing coupled with soaking in the buffer solution were able to effectively restore the initial membrane flux (Fig. 2.15); which indicates incomplete PEM removal. Interestingly, the membrane resistance of the regenerated PEM membranes was markedly higher for the backwashed and buffered PEM, as opposed to the buffered only membrane. Rejections of the regenerated PEM membranes were lower than those of the newly made ones (Fig. 2.16 and Fig. 2.17), even though there was an increase in membrane resistance (Fig. 2.15). The results imply that PEMs are capable of being regenerated, although there is a loss of flux and rejection performance. Further analysis of different buffer solution and/or backwashing strategies could yield a fully regenerable PEM-based membrane.

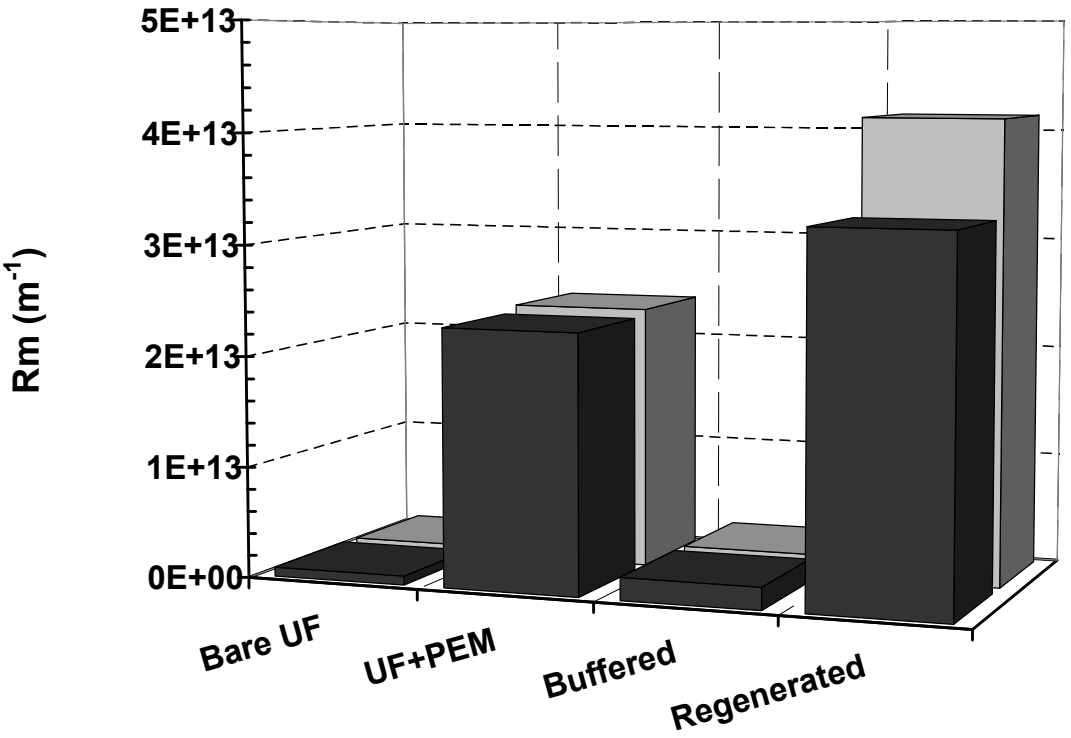

Figure 2.15. The membrane resistances of two UF+$(PSS/PAH)_{4.5}$ membranes that were scaled by calcium sulfate with a solution saturation index of 0.9, buffered in a high pH solution to remove the PEM layer, and regenerated. The black columns are for a membrane that was buffered only and the grey columns are for a membrane that was both buffered and backwashed.

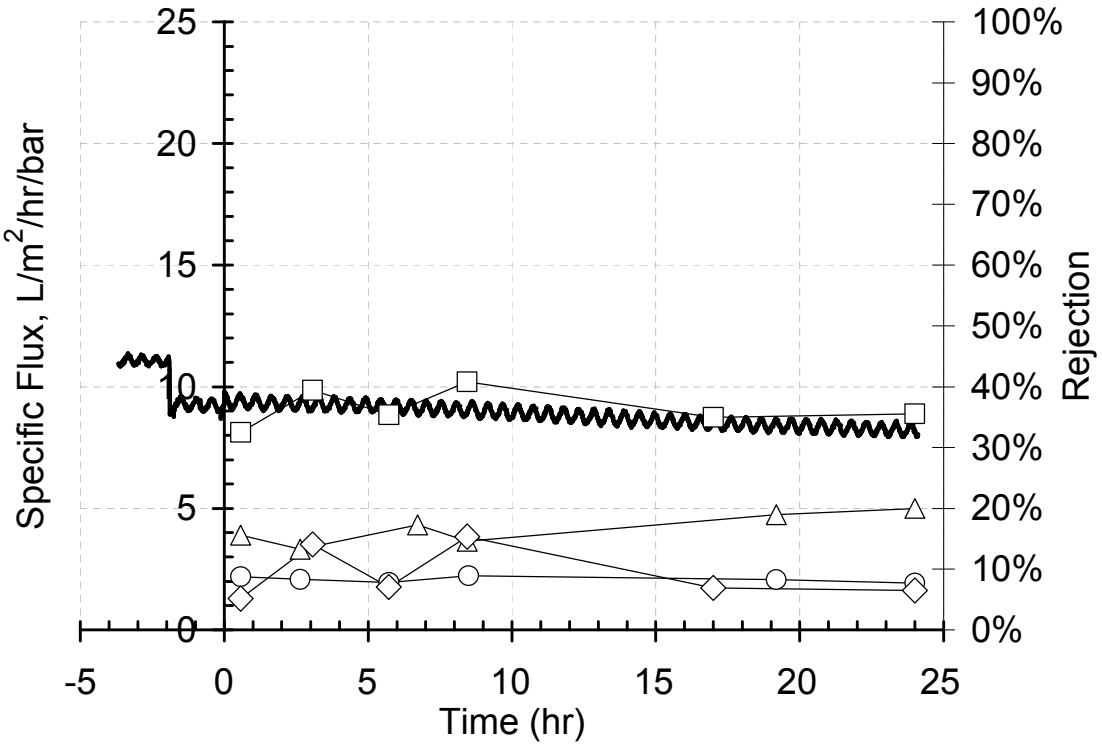

Figure 2.16. Flux and rejection performance of a previously scaled UF+$(PSS/PAH)_{4.5}$ membrane that was buffered and regenerated UF+$(PSS/PAH)_{4.5}$ membrane scaled by calcium sulfate with a feed solution saturation index of 0.9. The squares, triangles, circles and diamonds represent the sulfate, calcium, sodium, and chloride rejections; respectively. The solids black line represents flux data.

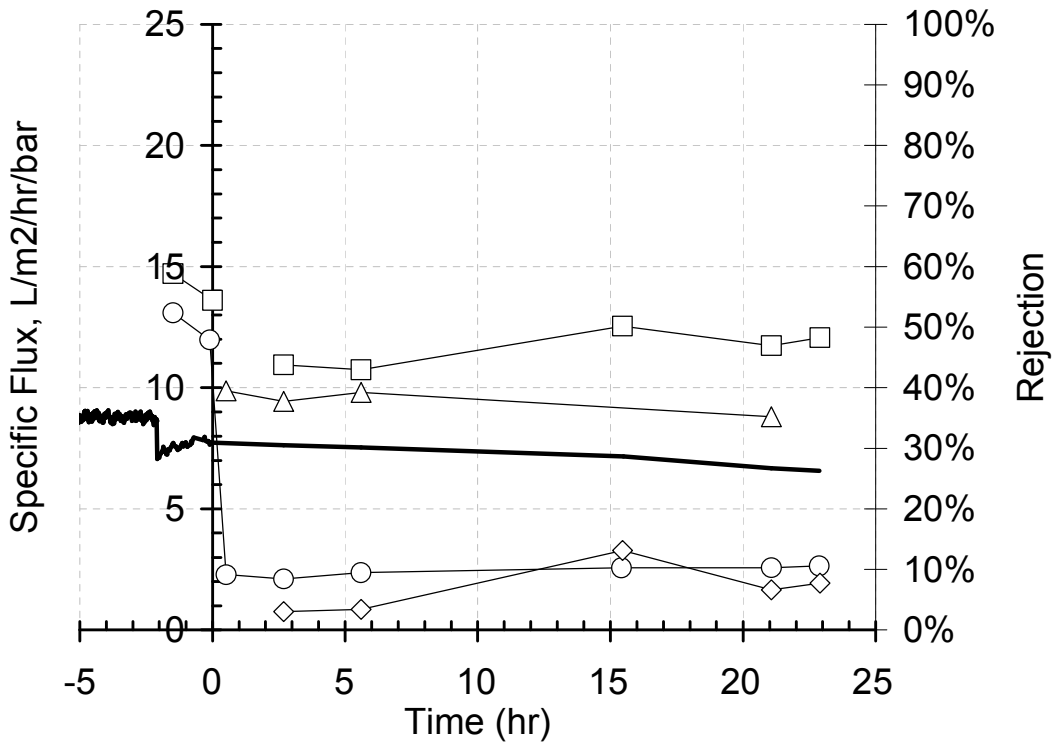

Figure 2.17. Flux and rejection performance of a previously scaled UF+$(PSS/PAH)_{4.5}$ membrane that was backwashed, buffered, and regenerated with and re-scaled by calcium sulfate with a feed solution saturation index of 0.9. The squares, triangles, circles and diamonds represent the sulfate, calcium, sodium, and chloride rejections; respectively. The solids black line represents flux data.

2.7.6. Scale Morphology

Previous studies have demonstrated that polyelectrolytes deployed as bulk scale inhibitors can affect the morphology of gypsum scale [77]. Similar effects have also been reported for calcium carbonate scale [93]. For gypsum scale the authors report different scale morphologies for different polyelectrolyte inhibitors. In the control experiments, gypsum scale precipitated as crystals of needle-like morphology. However, when PAA is used as an inhibitor they report a disappearance of the needle-like structure and the presence of small agglomerations. In light of these data SEM images were taken at of the PEM membrane surfaces in order to evaluate any such effects (Fig. 2.18, Fig. 2.19, and Fig. 2.20). All SEM samples were recorded from the same region of the membranes (Fig. 2.21). From Fig. 2.18, we can see fully developed gypsum scale rosettes on a NF270 membrane. The rosette structure of the scale is similar to what has been previously reported [64]. Comparing these images with those obtained for membranes from experiments with UF+$(PSS/PAH)_{4.5}$ and UF+$(PSS/PAH)_4$-(PAA) membranes we did not see any significant changes in the morphology of precipitated crystals. This could be attributed to the relatively low quantities of polyelectrolytes located on the membrane surface, as a sufficient amount of polyelectrolyte is needed to effectively inhibit gypsum scale and thus affect scale morphology.

All SEM images were taken from membranes at the end of fouling experiments when the membranes were covered by significant amount of gypsum scale. To understand and compare kinetics of surface blockage for both NF270 and PEM

membranes, membrane surface should be imaged during the early stages of the filtration process.

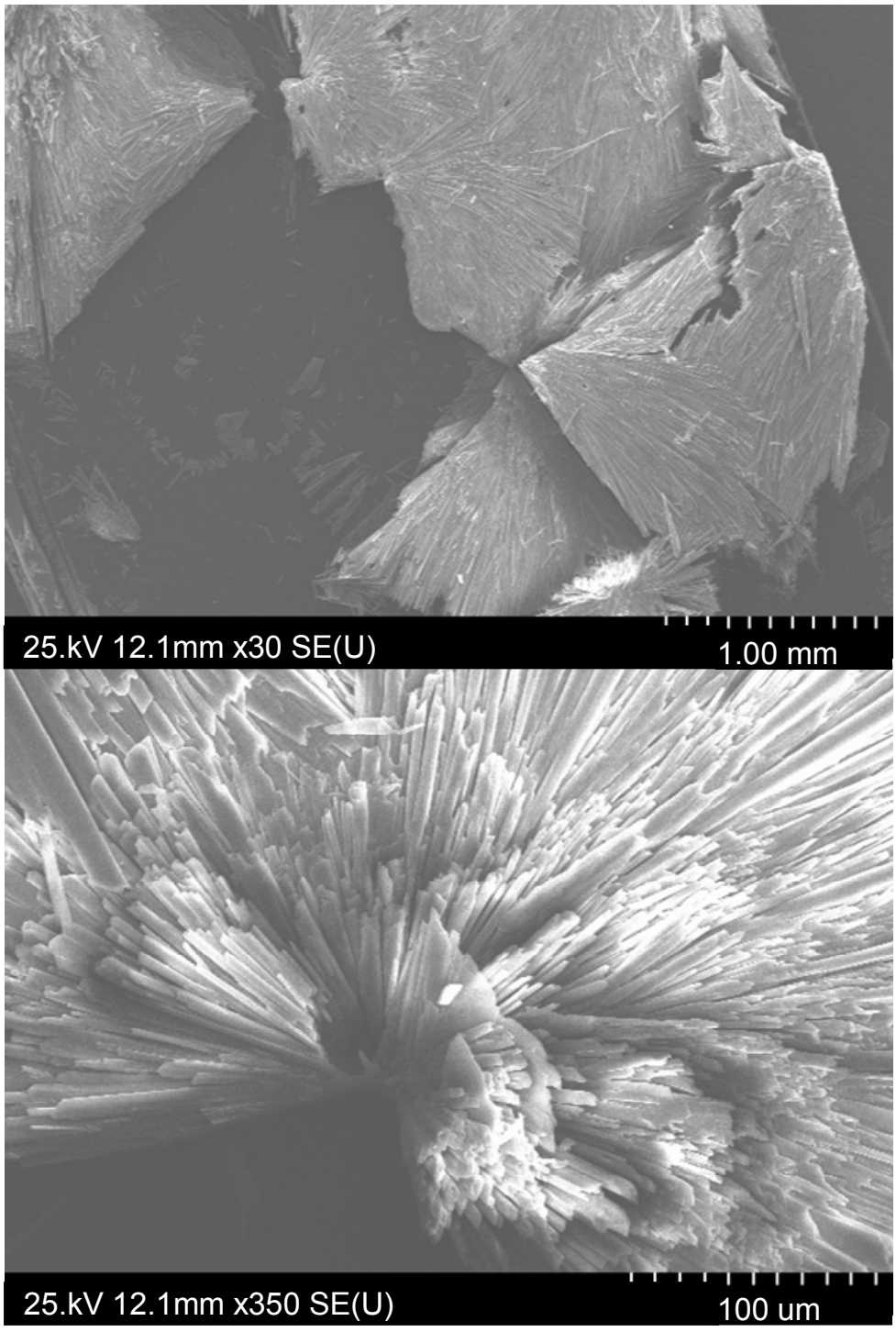

Figure 2.18. SEM images of gypsum scale on the surface of a NF270 membrane that was challenged by a calcium sulfate feed solution with a saturation index of 0.9 for ~24 hours.

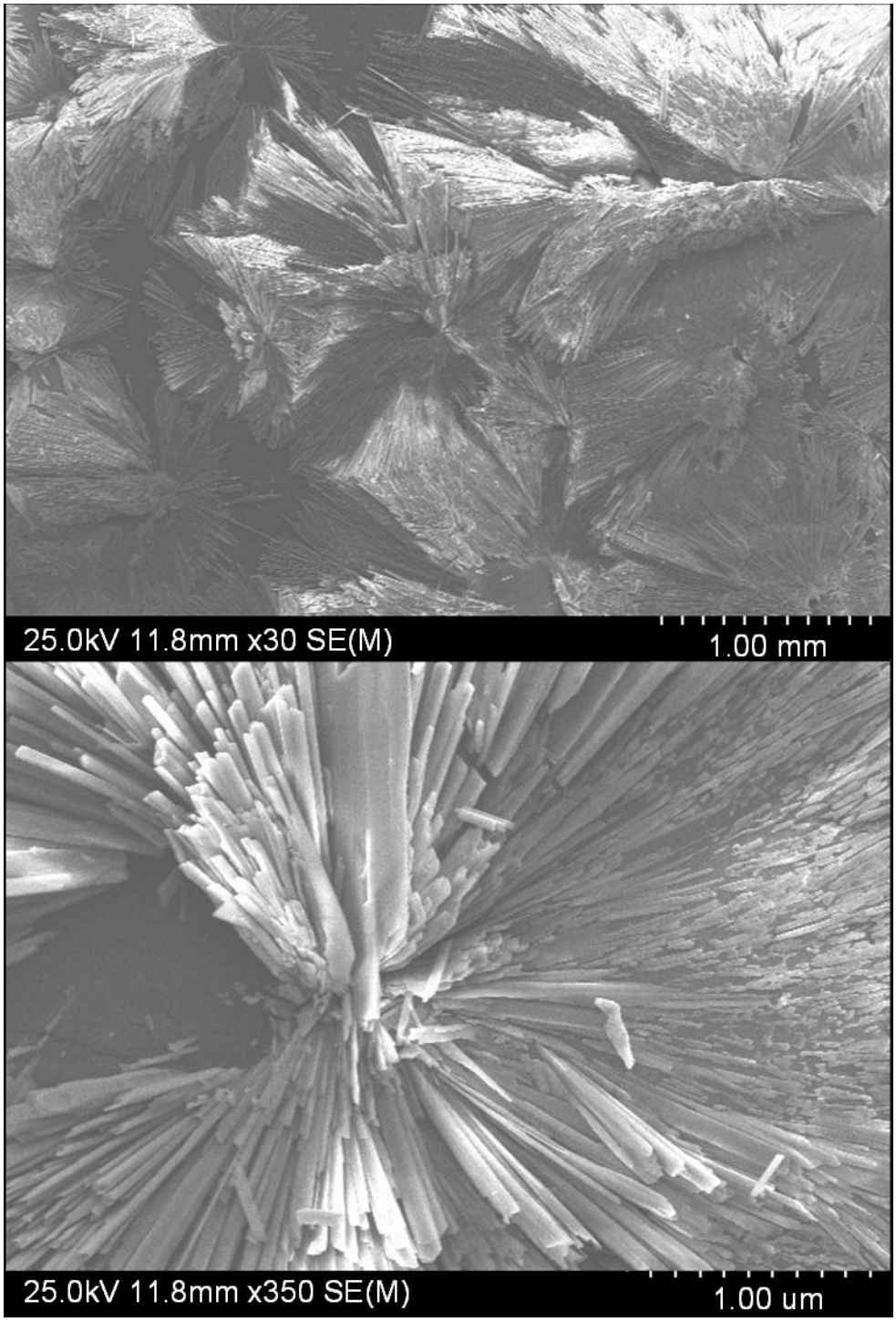

Figure 2.19. SEM images of gypsum scale on the surface of a UF+$(PSS/PAH)_{4.5}$ membrane that was challenged by a calcium sulfate feed solution with a saturation index of 0.9 for ~24 hours.

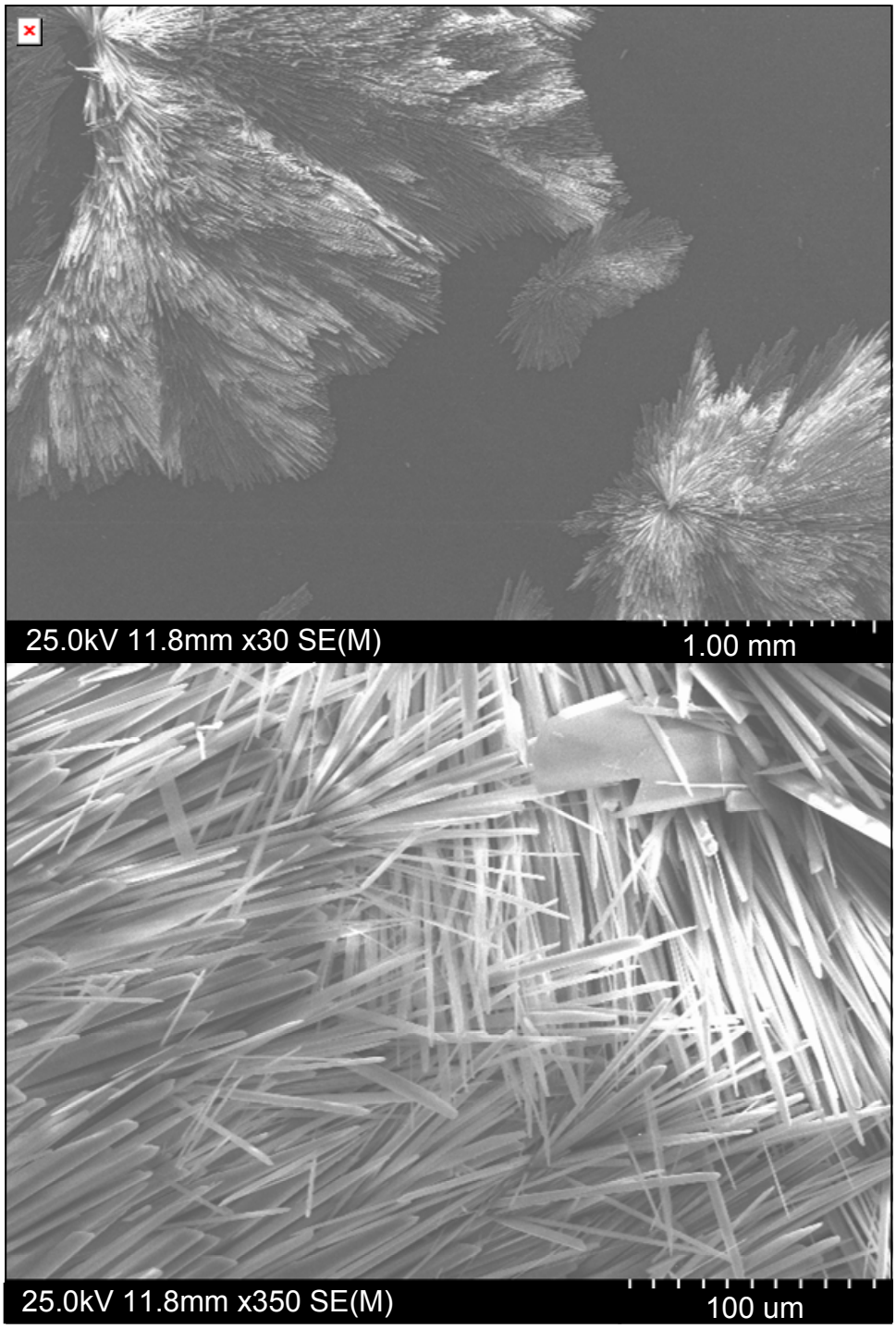

Figure 2.20. SEM images of gypsum scale on the surface of a UF+$(PSS/PAH)_4$-PAA membrane that was challenged by a calcium sulfate feed solution with a saturation index of 0.9 for ~24 hours.

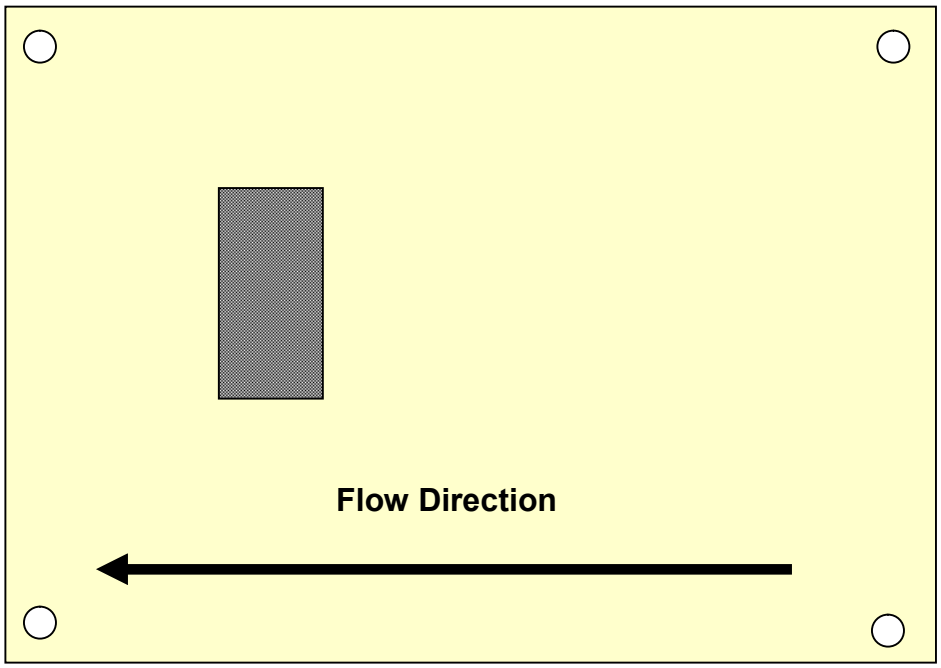

Figure 2.21. Schematic representation of where in the membrane coupon SEM images were taken.

2.7.7. Membrane Fouling by SRNOM

NOM has been shown to irreversibly foul NF membranes [84]. Accordingly, NF270 and PEM membranes were exposed to NOM feed solutions to evaluate their rejection and regeneration capabilities. NF270 consistently rejected almost all SRNOM (Fig. 2.22). The UF+$(PAA/PAH)_{4.5}$ membrane performed well initially, but rejection dramatically decreased with time (Fig. 2.23). The loss of rejection suggests either charge neutralization or deconstruction of the PEM. Since the flux declined with time, as opposed to increasing, which would be expected if the PEM's structural integrity was compromized, it is surmised that charge neutralization by foulant adsorption onto the PEM caused the decrease in rejection. Further investigation is needed however before any conclusions can be drawn.

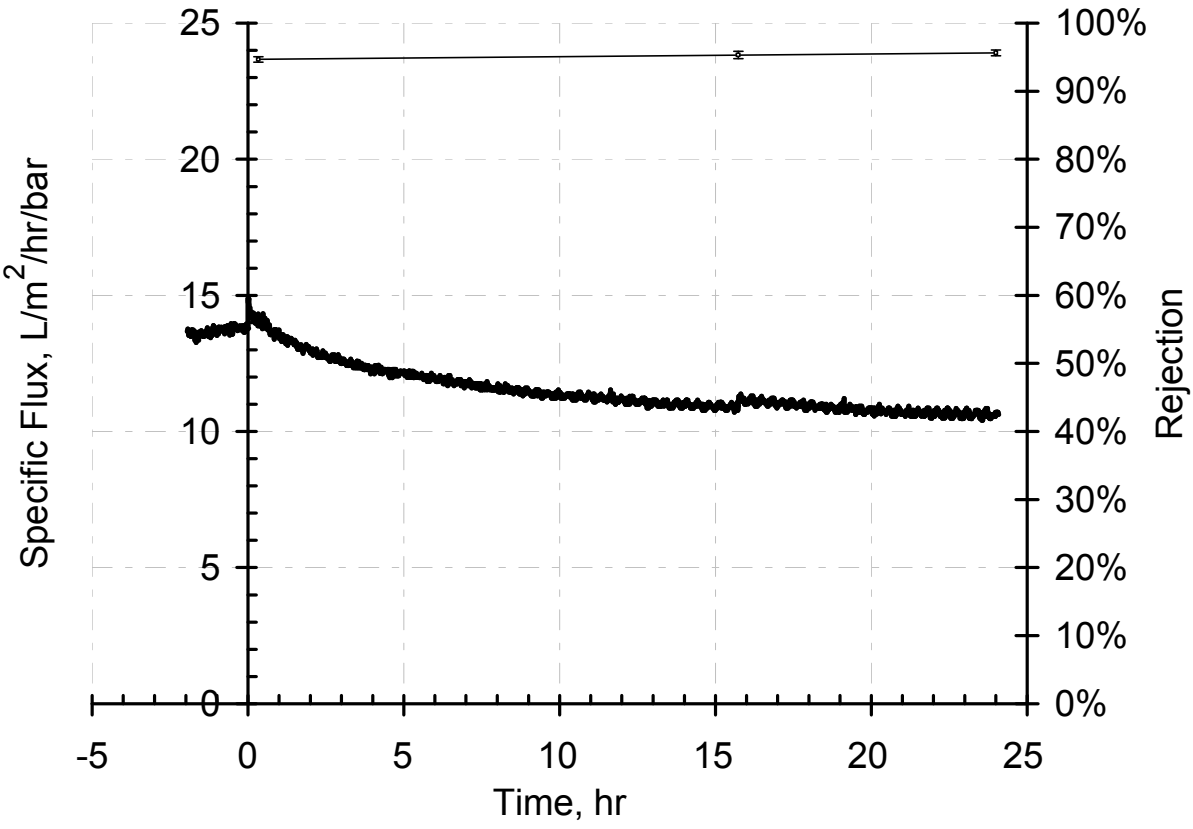

Figure 2.22. NF270 flux and TOC rejection performance when challenged with a 20 mg/L SRNOM solution.

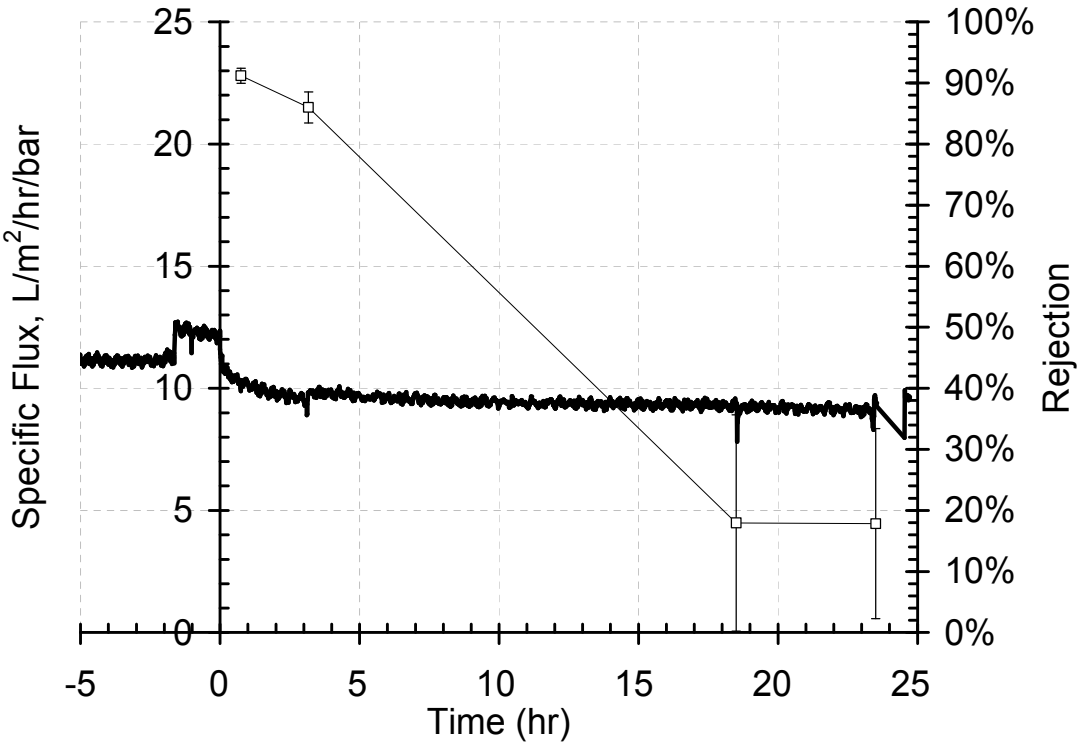

Figure 2.23. UF+$(PAA/PAH)_{4.5}$ flux and TOC rejection performance when challenged with a 20 mg/L SRNOM solution.

2.8. Summary

- Gypsum scale alone did not appear to irreversibly foul a NF270 membrane. We did not see a similar trend for PEM membranes as they did not fully recover their flux performance following a rinse with DI water. It was hypothesized that gypsum crystals are not fully removed from the PEM layer and thereby provide active growth sites for gypsum scale in the scaling experiment that follows.
- With a $(PSS/PAH)_{4.5}$ film deposited on a 50 kDa support we observed higher specific fluxes but lower overall rejections than NF270.
- Substituting low molecular weight PAA for PSS as the terminating layer in a $(PSS/PAH)_4$ membrane resulted in a ~25% increase in membrane resistance and a ~10% increase of monovalent and divalent ion rejections.
- Adding $(PSS/PAH)_3$-PAA to NF270 increased membrane resistance and only slightly increased rejection performance
- Adding $(PAA/PAH)_{3.5}$ to NF270 increased rejection performance and did not significantly affect membrane resistance.
- The PEM membranes considered in this thesis did not appear to possess antiscaling functionalities.
- We did not see any significant changes in surface scale morphology of PEM membranes when compared to NF270.
- Initial results indicated that PEM membrane rejection performance was not comparable to NF270.

APPENDIX

NANOCOMPOSITE MEMBRANES AND CARBON NANOPARTICLE ALIGNMENT VIA EXTERNAL FIELDS

By

Adam Rogensues

A Proposal

Submitted to

V.V. Tarabara, L.T. Drzal, S.J. Masten, M.L. Bruening

Department of Civil and Environmental Engineering
Michigan State University
East Lansing, MI 48824

1. BACKGROUND

Membrane filtration is a very powerful technique used in a wide variety of applications, including gas separation, membrane distillation, and aqueous membrane filtration. Aqueous membrane filtration is of particular importance due to its implications in the desalination of brackish and sea waters, as well as in wastewater treatment. Much recent research within aqueous membrane filtration involves the fabrication of multifunctional membranes. Multifunctional membranes could be defined as membranes that perform more than one specific task. One facet of multifunctional membranes is the incorporation of nanoparticles (NPs) into the membrane filtration process. Three popular methods that are used to incorporate nanoparticles include: 1) the deposition of NPs onto the membrane surface, 2) introduction of NPs to the feed solution, or 3) incorporation of NPs into the membrane polymer matrix. Much attention has been directed towards the latter of the three due to its simplicity and effective results. Using this method, researchers have been produce antibacterial membranes [1], antifouling membranes [94], and membranes with controllable permeabilities [95], among other functionalities.

Phase inversion membranes are a common type of membrane used for nanoparticle composites due to their relatively simple laboratory-scale fabrication process and wide applicability. Phase inversion can be defined as the process by which a polymer is transformed in a controlled manner from a liquid to a solid state [11]. A demixing process in which one liquid state forms two liquid states, which is often termed liquid-liquid demixing, usually initiates the solidification process. At a certain point in the demixing process one of the liquid states will solidify and form a solid matrix, thus

creating a membrane. The most common technique used to create phase inversion membranes is immersion precipitation, which is the process in which a polymer/solvent solution is cast on a support and subsequently immersed in a non-solvent bath [11]. This process is frequently used for nanocomposites because NPs are easily incorporated within the polymer matrix by simply suspending them within the casting solution prior to casting the membranes.

Polysulfone (Psf) is widely used in the fabrication of phase inversion membranes [96]. It is known to be a tough, rigid, high strength thermoplastic that maintains its characteristics over a wide range of temperatures. It has good thermal and chemical stability, mechanical strength, and oxidative resistance [96], [97], thus making it an ideal candidate for use in ultrafiltration membranes.

Graphite is a layered mineral composed of weakly bonded graphene sheets that are held together by van der Waals forces. When graphite is intercalated with acid it can be expanded to hundreds of times over its initial volume, which results in the separation of graphene nanosheets along the c-axis of the graphene layers [30]. These *exfoliated graphite nanoplatelets* (xGnP) are potential alternatives for clays and carbon nanotubes as they provide excellent competitive functionalities [98]. Furthermore, xGnP can be purchased for much lost cost (~$5/lb) than the potentially expensive carbon nanotubes [46].

Given the relative cheap cost and comparable properties of xGnP, the high applicability and societal relevance of Psf membranes, as well as the potential implications of nanocomposite membranes, a comprehensive study of xGnP-Psf composites is needed. The present proposal is focused on the fabrication and

characterization of xGnP-Psf nanocomposite membranes, the alignment of carbon-based nanoparticles within a Psf matrix, and the resulting properties of non-aligned and aligned xGnP-Psf composite membranes.

2. SIGNIFICANCE

The rapidly expanding global population and an increase in the standard of living of the growing middle class has put an unavoidable demand on water and energy resources [99]. With this growing demand comes the precipitous need for more efficient, more cost effective treatment technologies. An increasing water and wastewater treatment method is membrane filtration, especially in the United States. The number of installed plants and plant capacity has considerably increased since the first plant was installed in Keystone, Colorado in 1987 [100]. Although recent developments in membrane technology have drastically decreased operational and maintenance costs, further improvements are still apposite. These improvements include the need for more resilient, efficient, and multifunctional membranes.

Membrane breakage is a major problem that induces high maintenance costs in drinking water treatment plants [12]. The fabrication of durable, more resilient membranes would assist in the reduction of membrane breakage and therefore decrease maintenance and performance costs. Membrane compaction is an additional issue commonly experienced in membrane filtration plants. Compaction in membrane processes is a process by which the applied pressure causes the membrane structure to become denser, resulting in flux decline [11], [98]. Results have shown that compaction in reverse osmosis membranes can cause up to a 20 percent increase in membrane resistance [82]. This increase in resistance induces more energy consumption, thus decreasing the efficiency of the filtration process.

Examples of multifunctional membranes could be catalytically active membranes or membranes with controllable permeability. There has been recent interest in the

development of both such technologies [101], [102], [4]. Reactive membranes have very relevant industrial applications, as they could be used to expediently convert a hazardous substance to more environmentally tolerable material. Controllable permeability could allow the membrane to adapt to changing feed solutions and increase treatment applicabilities. Both are in their infant stages of development and their stands to be significant improvements in coming years.

In light of the stated results, a comprehensive study of non-aligned and align nanoparticles within a porous membrane and its effects on the hydraulic, mechanical, and morphological properties of phase inversion membranes is warranted. Both should allow for the improvement of membrane efficiency and increase the applicability and tunability of ultrafiltration membranes.

3. LITERATURE REVIEW

3.1. Particle Enabled Nanocomposites

Many studies have been published that investigate the effect of particle incorporation on Psf membrane permeability and rejection [1], [6], [7], [9], [94], [95], [101] ; the overall goal being to increase membrane permeability and/or functionality without a loss of retention properties. An increase in permeability without a significant loss in retention is of obvious significance when considering the efficiency of the filtration process. While reports show mixed results for rejection performance, all show either almost no change (Fe_3O_4/Psf [101], TiO_2/Psf [94], MWCNT/PSf [9]), or an increase in membrane permeability (Ag/Psf [1], ZrO_2/Psf [95], MWCNT/Psf [97]). For the cases in which little or no permeability change occurred, the situation could be the result of incorrect particle concentration. A prime example of this lies in the two papers previously cited on MWCNT/PSf composites. One author reports an *increase* in membrane permeability at a MWCNT concentration of 1.5% w/w MWCNT/Psf concentration [97], while the other reports a statistically *indeterminate* change in flux at a higher loading of 4% [9]. An explanation of this discrepancy could be that the addition of larger amounts of inorganic fillers into the polymer-solvent matrix alters the viscosity of the mixture which in turn affects the solvent-nonsolvent diffusion rates and results in a thicker membrane skin layer [6], [7]. The increased skin thickness affects the overall membrane resistance, which effects water permeability; therefore different particle concentrations result in different membrane morphologies and different skin layer thicknesses. Thus, rather than choosing a single filler/Psf ratio, a series of experiments involving different ratios

should be conducted in order to determine the ideal concentration at which membrane permeability should increase without a significant loss in retention performance.

3.2. Electric Field Alignment of Carbon Nanoparticles

There have been many studies published on the alignment of carbon nanoparticles via external electric fields [103–112]. It is understood that when exposed to direct current (DC) electric fields, particles tend to migrate towards the electrode [111], [113] , thus only alternating current (AC) electric fields were considered. Furthermore, the alignment via an external AC field has been tested using carbon nanoparticles in various media. Given the scope of this report, we will limit the reviewed literature to carbon nanoparticles aligned in composites. The nanoparticles considered include carbon nanotubes, graphite flakes, carbon nanofibers, carbon black, and graphite nanosheets.

3.2.1. Theory

The alignment of a particle within an electric field can be described by

$$\tau = \left| pxE \right| \tag{1}$$

where τ is the torque on induced on a particle, p is the polarizability, and E is the applied electric field. For carbon nanotubes, this becomes

$$I\left(\alpha_{||} - \alpha_{\perp}\right)E^2 \sin(\theta)\cos(\theta) \tag{2}$$

where l is the length of the nanotube, $\alpha_{\perp}$ is the perpendicular polarizability per unit length, $\alpha_{||}$ is the parallel polarizability per unit length, and θ is the angle to the field. Theoretically, $\alpha_{||}>\alpha_{\perp}$for all nanotubes, even more so for metallic nanotubes [31]. This implies that all carbon nanotubes experience a greater torque to align parallel to the electric field than they due perpendicular. Graphite also has been reported to have an anisotropic electric polarizability; results suggest that the same agreement applies, $\alpha_{||}>\alpha_{\perp}$ (typically by a factor of ~3) [32].

3.2.2. Carbon Nanotubes

Martin et al. dispersed multiwalled-carbon-nanotubes (MWNTs) in a polymer resin and exposed the solution to both AC and DC fields during the resin curing process. They report more uniform and more aligned networks using AC fields. They also report that with increasing field strength (10 V/mm max) the bulk conductivity of the composites was enhanced [111]. In a similar experiment, Park et al immersed single-walled-carbon-nanotubes (SWNTs) in a polymer matrix and varied field strength, time of exposure, and frequency of the AC current. At an electrode spacing of 2.3 mm, they report that alignment ensued only after an applied current density of ~16 V/mm. The degree of alignment increased with an increase in all three factors: exposure time, field strength, and frequency [110]. Ma et al. [103] adopted a slightly different approach, in the sense that they compared the alignment of pristine MWNTs to that of oxidized MWNTs. The MWNTs were oxidized in a 1:1 mixture of sulfuric and nitric acid heated

to 150 $^{\circ}$C for 30 min. Composites were exposed to 300 V_{p-p} at a frequency of 500 Hz. They report less reagglomeration and better alignment for the oxidized NTs. This was attributed to less viscous resistance from the matrix brought upon by the shorter NT length and increased polar functional groups (-COOH, -OH) with leads to larger dipole moments [103].

3.2.3 Graphite Flakes

The successive alignment of graphite flakes of 100-300nm thickness and 6.5 μm in diameter has been demonstrated. Successive alignment was achieved by first exposing the x-axis of a sample to a 20 V/mm electric field for 5 min and immediately exposing the y-axis to a field of the same strength. Electrical anisotropy of the composites was increased by 5-6 orders of magnitude [106].

3.2.4. Carbon Nanofibers

Carbon nanofibers with a diameter distribution around 160 nm were aligned in an epoxy resin by applying AC and DC voltages of 40-80 V/mm; electrode spacing was 4.5 mm. They report significant anisotropic electric conductivities of the aligned samples [107].

3.3 Magnetic Field Alignment of Carbon Nanoparticles

There have been numerous studies conducted on the magnetic alignment of carbon nanotubes in various media via the application of external magnetic fields [114–118] however, no data was found on the magnetic alignment of xGnPs or NPs of similar compositions (i.e. other graphite materials). Considering that CNTs and xGnPs are very similar in chemical structure**,** strength, and conductivity, a review of the literature involving CNTs exposed to external magnetic fields was conducted.

3.3.1. Theory

In vacuum, the magnetic field **H** and the magnetic induction **B** are related by

$$B = \mu_o H \tag{3}$$

where μ_o is the magnetic permeability of the a vacuum ($4\pi x10^{-7}$ $VsA^{-1}m^{-1}$). In order to describe magnetic fields within a media a third parameter is added to eq 1; magnetization M. Magnetization can be defined as the volume density of the magnetic moments. eq. 3 now reads

$$B = \mu_o H + M \tag{4}$$

In isotropic *paramagnetic* or *diamagnetic* materials there is a linear relationship between magnetic field and magnetic induction

$$B = \mu\mu_o H \quad (5)$$

where μ is the *relative magnetic permeability*, which is dimensionless and >1 for paramagnetic materials and <1 for diamagnetic materials. This relationship between magnetization (M) and the magnetic field (H) defines the *magnetic susceptibility* χ. Our equation now becomes [38]

$$M = \chi\mu_o H \quad (6)$$

Research suggests that the magnetic susceptibility of carbon nanotubes and graphite are anisotropic. Tsui et al. [119] measured the magnetic susceptibility of MWNTs in a polymer composite are report that the susceptibility is indeed diamagnetic, anisotropic with the perpendicular component stronger than the tube axis component. Zaric et al. [120] also report that for SWNTs the magnetic susceptibility is larger in the perpendicular component than the parallel component; reporting a value of ~1.4×10^{-5}emu/mol. The susceptibility of graphite is also anisotropic and reported to be -5×10^{-7} emu/g perpendicular to the c-axis and -375×10^{-7} parallel to the c-axis [121], but decreases with increasing temperature.

3.3.2. Carbon Nanotubes

As stated above, there have been numerous strategies implemented to align carbon nanotubes using a magnetic field, but none were found for xGnPs. This is particularly interesting because it has been reported that graphite (agglomeration of entercalated graphene) has an anisotropic magnetic susceptibility larger than that of carbon nanotubes, where $\chi_{||}$ (c-axis)/$\chi_{\perp}$(c-axis) is 75 and $\chi_{||}$(axis)/$\chi_{\perp}$(axis) is 3, respectively [122]. Most strategies implemented to align CNTs involve the use of inefficient high strength magnetic fields that require special facilities and large quantities of energy [115], [116], [123]. More recently novel techniques such as the attachment of magnet particles to the perimeter of CNTs and utilization of magnetic catalysts have shown promising results at much lower magnetic field strengths. Kordas et al. used impure CNTs containing residual iron catalyst particles left over from the fabrication process to increase the magnetic response of the CNTs and were able to successfully align the CNTs at a magnetic filed strength of ~1 Tesla. Correa-Duarte et al. [118] attached magnetite NPs to the exterior of CNTs via layer-by-layer (LbL) assembly technique and were able to align the particles at a surprisingly low magnetic field strength of 0.2 Tesla. Interestingly, the polyelectrolyte utilized in the technique to wrap CNTs has been shown to effectively wrap and disperse xGnP in aqueous solutions [124].

One study was found that investigated the effect of particle-enabled membranes exposed to external magnetic fields during the filtration process. The authors report no change in membrane permeability post particle incorporation, but report a controllable change in membrane retention. The results however were inconclusive on the exact

mechanism of retention alterations, as it could have been a function of the solute or the membrane morphology [101].

3.4 Summary

A wide variety of nanoparticle fillers have been incorporated into porous polymer matrices. Results by previous authors indicate that correctly fabricated nanocomposite membranes could result in a membrane of increased permeability without a significant loss in retention, thus resulting in a more economical membrane. Previous reports also state that carbon nanoparticles have been successfully aligned in various media using both electric and magnetic fields. In order to achieve successful alignment of carbon nanoparticles in a polymer matrix via electric fields, it appears that a field density of ~20 V/mm is needed. Both nanotubes and nano-graphite should align parallel to the external field. In order to align pristine carbon nanotubes via external magnetic fields, prohibitively high field strengths are needed. There are however, methods such as magnetic particle coating of the CNTs that can be used in order to drastically decrease the field strength needed.

4. Proposal

4.1. Plan of Action

We plan to investigate the effects of randomly dispersed and aligned exfoliated graphite nanoplatelets on a phase inversion polysulfone ultrafiltration membranes. By doing so, we hope to achieve numerous advantageous results. First, by randomly dispersing the xGnP within a Psf membrane matrix we hope to fabricate a membrane with higher permeability without a significant loss in retention. We plan to characterize the composite membranes by testing **flux**, **rejection**, **compaction**, and **biofouling** potential. Second, after successfully fabricating and characterizing the randomly dispersed particles, we plan on aligning the nanocomposites by exposing the composite membrane film to external electric and/or magnetic fields. The external fields should align the nanoparticles within the Psf matrix. This should yield a less compacting membrane, due to increased anisotropic membrane properties. The same characterization methods described above will be applied. Furthermore, we hypothesize that by manipulating the orientation of the high aspect ratio xGnPs that we will effectively be able to control the permeability of the nanocomposite membrane. We will test this by simply exposing a nanocomposite membrane to an external field during the filtration process.

REFERENCES

REFERENCES

[1] J. S. Taurozzi et al., “Effect of filler incorporation route on the properties of polysulfone-silver nanocomposite membranes of different porosities,” *Journal of Membrane Science*, vol. 325, no. 1, pp. 58-68, 2008.

[2] J. S. Taurozzi, C. A. Crock, and V. V. Tarabara, “C60-polysulfone nanocomposite membranes: Entropic and enthalpic determinants of C60 aggregation and its effects on membrane properties,” *Desalination*, vol. In Press, .

[3] D. M. Dotzauer, S. Bhattacharjee, Y. Wen, and M. L. Bruening, “Nanoparticle-Containing Membranes for the Catalytic Reduction of Nitroaromatic Compounds,” *Langmuir*, vol. 25, no. 3, pp. 1865-1871, 2009.

[4] D. M. Dotzauer, J. Dai, L. Sun, and M. L. Bruening, “Catalytic Membranes Prepared Using Layer-by-Layer Adsorption of Polyelectrolyte/Metal Nanoparticle Films in Porous Supports,” *Nano Letters*, vol. 6, no. 10, pp. 2268-2272, 2006.

[5] L. Ouyang, D. M. Dotzauer, S. R. Hogg, J. Macan·s, J.-F. Lahitte, and M. L. Bruening, “Catalytic hollow fiber membranes prepared using layer-by-layer adsorption of polyelectrolytes and metal nanoparticles,” *Catalysis Today*, vol. In Press, .

[6] P. Aerts, I. Genne, S. Kuypers, R. Leysen, I. F. J. Vankelecom, and P. A. Jacobs, “Polysulfone-aerosil composite membranes: Part 2. The influence of the addition of aerosil on the skin characteristics and membrane properties,” *Journal of Membrane Science*, vol. 178, no. 1-2, pp. 1-11, 2000.

[7] P. Aerts, E. Van Hoof, R. Leysen, I. F. J. Vankelecom, and P. A. Jacobs, “Polysulfone-Aerosil composite membranes: Part 1. The influence of the addition of Aerosil on the formation process and membrane morphology,” *Journal of Membrane Science*, vol. 176, no. 1, pp. 63-73, 2000.

[8] J. Kim, S. H. R. Davies, M. J. Baumann, V. V. Tarabara, and S. J. Masten, “Effect of ozone dosage and hydrodynamic conditions on the permeate flux in a hybrid ozonation-ceramic ultrafiltration system treating natural waters,” *Journal of Membrane Science*, vol. 311, no. 1-2, pp. 165-172, 2008.

[9] L. Brunet et al., “Properties of Membranes Containing Semi-dispersed Carbon Nanotubes,” *Environmental Engineering Science*, vol. 25, no. 4, pp. 565-576, 2008.

[10] S. Kim, I. Do, and L. T. Drzal, “Thermal stability and dynamic mechanical behavior of exfoliated graphite nanoplatelets-LLDPE nanocomposites,” *Polymer Composites*, vol. 31, no. 5, pp. 755-761.

[11] M. Mulder, *Basic Principles of Membrane Technology*. Dordrecht: Kluwer Academic Publishers, 1996.

[12] M. L. Bruening, D. M. Dotzauer, P. Jain, L. Ouyang, and G. L. Baker, "Creation of Functional Membranes Using Polyelectrolyte Multilayers and Polymer Brushes," *Langmuir*, vol. 24, no. 15, pp. 7663-7673, 2008.

[13] R. Malaisamy and M. L. Bruening, "High-Flux Nanofiltration Membranes Prepared by Adsorption of Multilayer Polyelectrolyte Membranes on Polymeric Supports," *Langmuir*, vol. 21, no. 23, pp. 10587-10592, 2005.

[14] M. D. Miller and M. L. Bruening, "Controlling the Nanofiltration Properties of Multilayer Polyelectrolyte Membranes through Variation of Film Composition," *Langmuir*, vol. 20, no. 26, pp. 11545-11551, 2004.

[15] L. Ouyang, R. Malaisamy, and M. L. Bruening, "Multilayer polyelectrolyte films as nanofiltration membranes for separating monovalent and divalent cations," *Journal of Membrane Science*, vol. 310, no. 1-2, pp. 76-84, 2008.

[16] B. W. Stanton, J. J. Harris, M. D. Miller, and M. L. Bruening, "Ultrathin, Multilayered Polyelectrolyte Films as Nanofiltration Membranes," *Langmuir*, vol. 19, no. 17, pp. 7038-7042, 2003.

[17] J. J. Harris, J. L. Stair, and M. L. Bruening, "Layered Polyelectrolyte Films as Selective, Ultrathin Barriers for Anion Transport," *Chemistry of Materials*, vol. 12, no. 7, pp. 1941-1946, 2000.

[18] M. S. Diallo, S. Christie, P. Swaminathan, J. H. Johnson, and W. A. Goddard, "Dendrimer Enhanced Ultrafiltration. 1. Recovery of Cu(II) from Aqueous Solutions Using PAMAM Dendrimers with Ethylene Diamine Core and Terminal NH2 Groups," *Environmental Science & Technology*, vol. 39, no. 5, pp. 1366-1377, 2005.

[19] S. M. C. Ritchie, L. G. Bachas, T. Olin, S. K. Sikdar, and D. Bhattacharyya, "Surface Modification of Silica- and Cellulose-Based Microfiltration Membranes with Functional Polyamino Acids for Heavy Metal Sorption," *Langmuir*, vol. 15, no. 19, pp. 6346-6357, 1999.

[20] S. M. C. Ritchie, K. E. Kissick, L. G. Bachas, S. K. Sikdar, C. Parikh, and D. Bhattacharyya, "Polycysteine and Other Polyamino Acid Functionalized Microfiltration Membranes for Heavy Metal Capture," *Environmental Science & Technology*, vol. 35, no. 15, pp. 3252-3258, 2001.

[21] J. A. Hestekin, L. G. Bachas, and D. Bhattacharyya, "Poly(amino acid)-Functionalized Cellulosic Membranes: Metal Sorption Mechanisms and Results,"

Industrial & Engineering Chemistry Research, vol. 40, no. 12, pp. 2668-2678, 2001.

[22] V. Smuleac, D. A. Butterfield, S. K. Sikdar, R. S. Varma, and D. Bhattacharyya, "Polythiol-functionalized alumina membranes for mercury capture," *Journal of Membrane Science*, vol. 251, no. 1-2, pp. 169-178, 2005.

[23] D. G. Yu, M. Y. Teng, W. L. Chou, and M. C. Yang, "Characterization and inhibitory effect of antibacterial PAN-based hollow fiber loaded with silver nitrate," *Journal of Membrane Science*, vol. 225, no. 1-2, pp. 115-123, 2003.

[24] W.-L. Chou, D.-G. Yu, and M.-C. Yang, "The preparation and characterization of silver-loading cellulose acetate hollow fiber membrane for water treatment," *Polymers for Advanced Technologies*, vol. 16, no. 8, pp. 600-607, 2005.

[25] R. Bhattacharya, T. N. Phaniraj, and D. Shailaja, "Polysulfone and polyvinyl pyrrolidone blend membranes with reverse phase morphology as controlled release systems: experimental and theoretical studies," *Journal of Membrane Science*, vol. 227, no. 1-2, pp. 23-37, 2003.

[26] J. G. Sanchez Marcano and T. T. Tsotsis, "Introduction," in *Catalytic Membranes and Membrane Reactors*, Wiley-VCH Verlag GmbH & Co. KGaA, 2004, pp. 1-14.

[27] H. Fukushima and L. T. Drzal, "Graphite Nanoreinforcements in Polymer Nanocomposites," *Materials Science and Engineering*, vol. Ph.D. Michigan State University, East Lansing, 2003.

[28] K. Kalaitzidou, H. Fukushima, and L. T. Drzal, "Mechanical properties and morphological characterization of exfoliated graphite-polypropylene nanocomposites," *Composites Part A: Applied Science and Manufacturing*, vol. 38, no. 7, pp. 1675-1682, 2007.

[29] K. S. Novoselov et al., "Electric Field Effect in Atomically Thin Carbon Films ," *Science* , vol. 306, no. 5696, pp. 666-669, Oct. 2004.

[30] D. Cho, S. Lee, G. Yang, H. Fukushima, and L. T. Drzal, "Dynamic Mechanical and Thermal Properties of Phenylethynyl-Terminated Polyimide Composites Reinforced With Expanded Graphite Nanoplatelets," *Macromolecular Materials and Engineering*, vol. 290, no. 3, pp. 179-187, 2005.

[31] G. Chen, C. Wu, W. Weng, D. Wu, and W. Yan, "Preparation of polystyrene/graphite nanosheet composite," *Polymer*, vol. 44, no. 6, pp. 1781-1784, 2003.

[32] J. Lu, L. T. Drzal, R. M. Worden, and I. Lee, "Simple Fabrication of a Highly Sensitive Glucose Biosensor Using Enzymes Immobilized in Exfoliated Graphite

Nanoplatelets Nafion Membrane," *Chemistry of Materials*, vol. 19, no. 25, pp. 6240-6246, Nov. 2007.

[33] M. Haruta, "Gold as a Novel Catalyst in the 21st Century: Preparation, Working Mechanism and Applications," *ChemInform*, vol. 35, no. 44, p. no-no, 2004.

[34] M. Haruta, N. Yamada, T. Kobayashi, and S. Iijima, "Gold catalysts prepared by coprecipitation for low-temperature oxidation of hydrogen and of carbon monoxide," *Journal of Catalysis*, vol. 115, no. 2, pp. 301-309, 1989.

[35] A. Sanchez et al., "When gold is not noble: Nanoscale gold catalysts," *JOURNAL OF PHYSICAL CHEMISTRY A*, vol. 103, no. 48, pp. 9573-9578, Dec. 1999.

[36] G. Luft, "Principles and Practice of Heterogeneous Catalysis. J. M. Thomas, Wiley-VCH Verlagsgesellschaft, Weinheim, 669 Seiten; brosch., DM 88,– ISBN 3-527-29239-x," *Chemie Ingenieur Technik*, vol. 70, no. 5, pp. 581-582, 1998.

[37] S. Panigrahi et al., "Synthesis and Size-Selective Catalysis by Supported Gold Nanoparticles:‚Äâ Study on Heterogeneous and Homogeneous Catalytic Process," *The Journal of Physical Chemistry C*, vol. 111, no. 12, pp. 4596-4605, 2007.

[38] EPA, "Technology Transfer Network Air Toxics Web Site: 4-Nitrophenol," vol. 2011, no. 23. 2007.

[39] Y.-C. Chang and D.-H. Chen, "Catalytic reduction of 4-nitrophenol by magnetically recoverable Au nanocatalyst," *Journal of Hazardous Materials*, vol. 165, no. 1-3, pp. 664-669, 2009.

[40] A. Kumar, S. Kumar, S. Kumar, and D. V. Gupta, "Adsorption of phenol and 4-nitrophenol on granular activated carbon in basal salt medium: Equilibrium and kinetics," *Journal of Hazardous Materials*, vol. 147, no. 1-2, pp. 155-166, 2007.

[41] S. Laha and K. P. Petrova, "Biodegradation of 4-nitrophenol by indigenous microbial populations in Everglades soils," *Biodegradation*, vol. 8, no. 5, pp. 349-356, 1998.

[42] M. S. Dieckmann and K. A. Gray, "A comparison of the degradation of 4-nitrophenol via direct and sensitized photocatalysis in TiO2 slurries," *Water Research*, vol. 30, no. 5, pp. 1169-1183, 1996.

[43] C. Li, K. L. Shuford, M. Chen, E. J. Lee, and S. O. Cho, "A Facile Polyol Route to Uniform Gold Octahedra with Tailorable Size and Their Optical Properties," *ACS Nano*, vol. 2, no. 9, pp. 1760-1769, 2008.

[44] R. Yu et al., “Platinum Deposition on Carbon Nanotubes via Chemical Modification,” *Chemistry of Materials*, vol. 10, no. 3, pp. 718-722, Jan. 1998.

[45] W. Li et al., “Preparation and Characterization of Multiwalled Carbon Nanotube-Supported Platinum for Cathode Catalysts of Direct Methanol Fuel Cells,” *The Journal of Physical Chemistry B*, vol. 107, no. 26, pp. 6292-6299, 2003.

[46] J. Lu, I. Do, L. T. Drzal, R. M. Worden, and I. Lee, “Nanometal-Decorated Exfoliated Graphite Nanoplatelet Based Glucose Biosensors with High Sensitivity and Fast Response,” *ACS Nano*, vol. 2, no. 9, pp. 1825-1832, 2008.

[47] V. Lordi, N. Yao, and J. Wei, “Method for Supporting Platinum on Single-Walled Carbon Nanotubes for a Selective Hydrogenation Catalyst,” *Chemistry of Materials*, vol. 13, no. 3, pp. 733-737, 2001.

[48] T. W. Ebbesen, H. Hiura, M. E. Bisher, M. M. J. Treacy, J. L. Shreeve-Keyer, and R. C. Haushalter, “Decoration of carbon nanotubes,” *Advanced Materials*, vol. 8, no. 2, pp. 155-157, 1996.

[49] U. S. D. of Energy, “DOE Fundamental Handbook: Chemistry,” vol. 2, no. 2. Washington, D.C., 1993.

[50] W. C. Jiaqi Wan Jiangtao Feng, Xiangxi Meng, Enzhong Liu, “In situ decoration of carbon nanotubes with nearly monodisperse magnetite nanoparticles in liquid polyols,” *Journal of Materials Chemistry*, vol. 17, p. 5, 2007.

[51] C. A. Leon y Leon, J. M. Solar, V. Calemma, and L. R. Radovic, “Evidence for the protonation of basal plane sites on carbon,” *Carbon*, vol. 30, no. 5, pp. 797-811, 1992.

[52] E. Antolini, “Formation, microstructural characteristics and stability of carbon supported platinum catalysts for low temperature fuel cells,” *Journal of Materials Science*, vol. 38, no. 14, pp. 2995-3005, 2003.

[53] D. O. W. W. and P. Solutions, “FILMTEC Reverse Osmosis Membranes: Technical Manual.” Dow Chemical Company, p. 181.

[54] K. L. Kelly, E. Coronado, L. L. Zhao, and G. C. Schatz, “The Optical Properties of Metal Nanoparticles: The Influence of Size, Shape, and Dielectric Environment,” *The Journal of Physical Chemistry B*, vol. 107, no. 3, pp. 668-677, Dec. 2002.

[55] S. Goyanes, G. R. Rubiolo, A. Salazar, A. Jimeno, M. A. Corcuera, and I. Mondragon, “Carboxylation treatment of multiwalled carbon nanotubes monitored by infrared and ultraviolet spectroscopies and scanning probe microscopy,” *Diamond and Related Materials*, vol. 16, no. 2, pp. 412-417, 2007.

[56] Q.-Z. Zheng, P. Wang, Y.-N. Yang, and D.-J. Cui, “The relationship between porosity and kinetics parameter of membrane formation in PSF ultrafiltration membrane,” *Journal of Membrane Science*, vol. 286, no. 1-2, pp. 7-11, 2006.

[57] I. V. Lightcap, T. H. Kosel, and P. V. Kamat, “Anchoring Semiconductor and Metal Nanoparticles on a Two-Dimensional Catalyst Mat. Storing and Shuttling Electrons with Reduced Graphene Oxide,” *Nano Letters*, vol. 10, no. 2, pp. 577-583, 2010.

[58] W. Cai and J. Wan, “Facile synthesis of superparamagnetic magnetite nanoparticles in liquid polyols,” *Journal of Colloid and Interface Science*, vol. 305, no. 2, pp. 366-370, 2007.

[59] S. Shirazi, C.-J. Lin, and D. Chen, “Inorganic fouling of pressure-driven membrane processes: A critical review,” *Desalination*, vol. 250, no. 1, pp. 236-248.

[60] A. W. W. Association, *Water Quality and Treatment: A Handbook of Community Water Supplies*, 5th ed. McGraw-Hill, 1999.

[61] M. Nystrom, L. Kaipia, and S. Luque, “Fouling and retention of nanofiltration membranes,” *Journal of Membrane Science*, vol. 98, no. 3, pp. 249-262, 1995.

[62] R. Liikanen, J. Yli-Kuivila, J. Tenhunen, and R. Laukkanen, “Cost and environmental impact of nanofiltration in treating chemically pre-treated surface water,” *Desalination*, vol. 201, no. 1,Äì3, pp. 58-70, 2006.

[63] Y. A. Le Gouellec and M. Elimelech, “Calcium sulfate (gypsum) scaling in nanofiltration of agricultural drainage water,” *Journal of Membrane Science*, vol. 205, no. 1,Äì2, pp. 279-291, 2002.

[64] A. Rahardianto, W.-Y. Shih, R.-W. Lee, and Y. Cohen, “Diagnostic characterization of gypsum scale formation and control in RO membrane desalination of brackish water,” *Journal of Membrane Science*, vol. 279, no. 1,Äì2, pp. 655-668, 2006.

[65] “US ultrafiltration market to reach US$908 million,” *Filtration & Separation*, vol. 44, no. 4, p. 6, 2007.

[66] G. Decher, “Fuzzy Nanoassemblies: Toward Layered Polymeric Multicomposites,” *Science*, vol. 277, no. 5330, pp. 1232-1237, 1997.

[67] S. U. Hong, R. Malaisamy, and M. L. Bruening, “Optimization of flux and selectivity in Cl-/SO42- separations with multilayer polyelectrolyte membranes,” *Journal of Membrane Science*, vol. 283, no. 1-2, pp. 366-372, 2006.

[68] S. T. Dubas and J. B. Schlenoff, “Polyelectrolyte Multilayers Containing a Weak Polyacid: Construction and Deconstruction,” *Macromolecules*, vol. 34, no. 11, pp. 3736-3740, 2001.

[69] R. W. Baker, *Membrane technology and applications*. J. Wiley, 2004.

[70] P. E. Odendaal, A. R. Foundation, L. des eaux-Dumez, and S. A. W. R. Commission, *Water treatment membrane processes*. McGraw-Hill, 1996.

[71] V. A. N. D. E. N. BERG, SMOLDERS, #160, and C. A., *Flux decline in membrane processes*, vol. 25. Oxford, ROYAUME-UNI: Elsevier, 1988.

[72] T. Asano, *Water reuse: issues, technologies, and applications*. McGraw-Hill, 2007.

[73] N. A. Lange and J. A. Dean, *Lange’s Handbook of chemistry*. McGraw-Hill, 1979.

[74] I. Atamanenko, A. Kryvoruchko, L. Yurlova, and E. Tsapiuk, “Study of the CaSO4 deposits in the presence of scale inhibitors,” *Desalination*, vol. 147, no. 1,Äì3, pp. 257-262, 2002.

[75] Z. Amjad, “Applications of antiscalants to control calcium sulfate scaling in reverse osmosis systems,” *Desalination*, vol. 54, no. 0, pp. 263-276, 1985.

[76] Z. Amjad, “Inhibition of calcium fluoride crystal growth by polyelectrolytes,” *Langmuir*, vol. 7, no. 10, pp. 2405-2408, 1991.

[77] M. Oner, O. Dogan, and G. Oner, “The influence of polyelectrolytes architecture on calcium sulfate dihydrate growth retardation,” *Journal of Crystal Growth*, vol. 186, no. 3, pp. 427-437, 1998.

[78] F. V. Williams and R. A. Ruehrwein, “Effect of Polyelectrolytes on the Precipitation of Calcium Carbonate,” *Journal of the American Chemical Society*, vol. 79, no. 18, pp. 4898-4900, 1957.

[79] Ö. Doğan, E. Akyol, and M. Öner, “Polyelectrolytes inhibition effect on crystallization of gypsum,” *Crystal Research and Technology*, vol. 39, no. 12, pp. 1108-1114, 2004.

[80] E. Akyol and M. √ñner, “Inhibition of calcium oxalate monohydrate crystal growth using polyelectrolytes,” *Journal of Crystal Growth*, vol. 307, no. 1, pp. 137-144, 2007.

[81] A. Hernandez, A. La Rocca, H. Power, U. Graupner, and G. Ziegenbalg, “Modelling the effect of precipitation inhibitors on the crystallization process from

well mixed over-saturated solutions in gypsum based on Langmuir‚ÄìVolmer flux correction," *Journal of Crystal Growth*, vol. 295, no. 2, pp. 217-230, 2006.

[82] F. Wang and V. V. Tarabara, "Coupled effects of colloidal deposition and salt concentration polarization on reverse osmosis membrane performance," *Journal of Membrane Science*, vol. 293, no. 1‚Ä¬2, pp. 111-123, 2007.

[83] M. Manttari, T. Pekuri, and M. Nystrom, "NF270, a new membrane having promising characteristics and being suitable for treatment of dilute effluents from the paper industry," *Journal of Membrane Science*, vol. 242, no. 1‚Ä¬2, pp. 107-116, 2004.

[84] Q. Li and M. Elimelech, "Organic Fouling and Chemical Cleaning of Nanofiltration Membranes:‚Äâ Measurements and Mechanisms," *Environmental Science & Technology*, vol. 38, no. 17, pp. 4683-4693, 2004.

[85] S. Lee and C.-H. Lee, "Effect of operating conditions on CaSO4 scale formation mechanism in nanofiltration for water softening," *Water Research*, vol. 34, no. 15, pp. 3854-3866, 2000.

[86] S. Bhattacharjee and G. M. Johnston, "A Model of Membrane Fouling by Salt Precipitation from Multicomponent Ionic Mixtures in Crossflow Nanofiltration," *Environmental Engineering Science*, vol. 19, no. 6, pp. 399-412, Nov. 2002.

[87] C.-J. Lin, S. Shirazi, and P. Rao, "Mechanistic Model for CaSO[sub 4] Fouling on Nanofiltration Membrane," *Journal of Environmental Engineering*, vol. 131, no. 10, pp. 1387-1392, 2005.

[88] Z. Adamczyk, M. Zembala, P. Warszy≈Ñski, and B. Jachimska, "Characterization of Polyelectrolyte Multilayers by the Streaming Potential Method," *Langmuir*, vol. 20, no. 24, pp. 10517-10525, 2004.

[89] P. A. Ngankam, P. Lavalle, L. Szyk, G. Decher, P. Schaaf, and F. J. G. Cuisinier, "Influence of Polyelectrolyte Multilayer Films on Calcium Phosphate Nucleation," *Journal of the American Chemical Society*, vol. 122, no. 37, pp. 8998-9005, 2000.

[90] L. Krasemann and B. Tieke, "Selective Ion Transport across Self-Assembled Alternating Multilayers of Cationic and Anionic Polyelectrolytes," *Langmuir*, vol. 16, no. 2, pp. 287-290, 1999.

[91] P. M. Claesson, E. Poptoshev, E. Blomberg, and A. Dedinaite, "Polyelectrolyte-mediated surface interactions," *Advances in Colloid and Interface Science*, vol. 114–115, no. 0, pp. 173-187, Jun. 2005.

[92] P. Bar-Yosef Ofir, R. Govrin-Lippman, N. Garti, and H. F√°redi-Milhofer, "The Influence of Polyelectrolytes on the Formation and Phase Transformation of

Amorphous Calcium Phosphate," *Crystal Growth & Design*, vol. 4, no. 1, pp. 177-183, 2003.

[93] Q. Yang, Y. Liu, A. Gu, J. Ding, and Z. Shen, "Investigation of Calcium Carbonate Scaling Inhibition and Scale Morphology by AFM," *Journal of Colloid and Interface Science*, vol. 240, no. 2, pp. 608-621, 2001.

[94] T.-H. Bae and T.-M. Tak, "Effect of TiO2 nanoparticles on fouling mitigation of ultrafiltration membranes for activated sludge filtration," *Journal of Membrane Science*, vol. 249, no. 1–2, pp. 1-8, Mar. 2005.

[95] I. Genné, S. Kuypers, and R. Leysen, "Effect of the addition of ZrO2 to polysulfone based UF membranes," *Journal of Membrane Science*, vol. 113, no. 2, pp. 343-350, May 1996.

[96] H.-L. Huang and S. Yang, "Filtration characteristics of polysulfone membrane filters," *Journal of Aerosol Science*, vol. 37, no. 10, pp. 1198-1208, Oct. 2006.

[97] J.-H. Choi, J. Jegal, and W.-N. Kim, "Fabrication and characterization of multi-walled carbon nanotubes/polymer blend membranes," *Journal of Membrane Science*, vol. 284, no. 1–2, pp. 406-415, Nov. 2006.

[98] K. Kalaitzidou, H. Fukushima, and L. T. Drzal, "A new compounding method for exfoliated graphite–polypropylene nanocomposites with enhanced flexural properties and lower percolation threshold," *Composites Science and Technology*, vol. 67, no. 10, pp. 2045-2051, Aug. 2007.

[99] R. L. McGinnis and M. Elimelech, "Global Challenges in Energy and Water Supply: The Promise of Engineered Osmosis," *Environmental Science & Technology*, vol. 42, no. 23, pp. 8625-8629, Dec. 2008.

[100] U. States and P. Agency, "LOW-PRESSURE MEMBRANE FILTRATION FOR PATHOGEN REMOVAL : APPLICATION , IMPLEMENTATION , AND REGULATORY ISSUES," *Environmental Protection*, no. April, 2001.

[101] P. Jian, H. Yahui, W. Yang, and L. Linlin, "Preparation of polysulfone–Fe3O4 composite ultrafiltration membrane and its behavior in magnetic field," *Journal of Membrane Science*, vol. 284, no. 1–2, pp. 9-16, Nov. 2006.

[102] J. Dai and M. L. Bruening, "Catalytic Nanoparticles Formed by Reduction of Metal Ions in Multilayered Polyelectrolyte Films," *Nano Letters*, vol. 2, no. 5, pp. 497-501, Apr. 2002.

[103] C. Ma et al., "Alignment and dispersion of functionalized carbon nanotubes in polymer composites induced by an electric field," *Carbon*, vol. 46, no. 4, pp. 706-710, Apr. 2008.

[104] K. Bubke, H. Gnewuch, M. Hempstead, J. Hammer, and M. L. H. Green, “Optical anisotropy of dispersed carbon nanotubes induced by an electric field,” *Applied Physics Letters*, vol. 71, no. 14, pp. 1906-1908, Oct. 1997.

[105] M. R. Diehl, S. N. Yaliraki, R. A. Beckman, M. Barahona, and J. R. Heath, “Self-Assembled, Deterministic Carbon Nanotube Wiring Networks,” *Angewandte Chemie*, vol. 114, no. 2, pp. 363-366, 2002.

[106] G. Chen, H. Wang, and W. Zhao, “Fabrication of highly ordered polymer/graphite flake composite with eminent anisotropic electrical property,” *Polymers for Advanced Technologies*, vol. 19, no. 8, pp. 1113-1117, 2008.

[107] T. Prasse, J.-Y. Cavaillé, and W. Bauhofer, “Electric anisotropy of carbon nanofibre/epoxy resin composites due to electric field induced alignment,” *Composites Science and Technology*, vol. 63, no. 13, pp. 1835-1841, Oct. 2003.

[108] M.-K. Schwarz, W. Bauhofer, and K. Schulte, “Alternating electric field induced agglomeration of carbon black filled resins,” *Polymer*, vol. 43, no. 10, pp. 3079-3082, May 2002.

[109] H. Wang, H. Zhang, W. Zhao, W. Zhang, and G. Chen, “Preparation of polymer/oriented graphite nanosheet composite by electric field-inducement,” *Composites Science and Technology*, vol. 68, no. 1, pp. 238-243, Jan. 2008.

[110] C. Park et al., “Aligned single-wall carbon nanotube polymer composites using an electric field,” *Journal of Polymer Science Part B: Polymer Physics*, vol. 44, no. 12, pp. 1751-1762, 2006.

[111] C. A. Martin et al., “Electric field-induced aligned multi-wall carbon nanotube networks in epoxy composites,” *Polymer*, vol. 46, no. 3, pp. 877-886, Jan. 2005.

[112] Z. Zhou, D. Wan, X. Dou, L. Song, W. Zhou, and S. Xie, “Postgrowth alignment of SWNTs by an electric field,” *Carbon*, vol. 44, no. 1, pp. 170-173, Jan. 2006.

[113] B. Kozinsky and N. Marzari, “Static Dielectric Properties of Carbon Nanotubes from First Principles,” *Physical Review Letters*, vol. 96, no. 16, p. 166801, Apr. 2006.

[114] M. Fujiwara, E. Oki, M. Hamada, Y. Tanimoto, I. Mukouda, and Y. Shimomura, “Magnetic Orientation and Magnetic Properties of a Single Carbon Nanotube,” *The Journal of Physical Chemistry A*, vol. 105, no. 18, pp. 4383-4386, Apr. 2001.

[115] T. Kimura, H. Ago, M. Tobita, S. Ohshima, M. Kyotani, and M. Yumura, “Polymer Composites of Carbon Nanotubes Aligned by a Magnetic Field,” *Advanced Materials*, vol. 14, no. 19, pp. 1380-1383, 2002.

[116] D. A. Walters et al., “In-plane-aligned membranes of carbon nanotubes,” *Chemical Physics Letters*, vol. 338, no. 1, pp. 14-20, Apr. 2001.

[117] K. Kordás et al., “Magnetic-Field Induced Efficient Alignment of Carbon Nanotubes in Aqueous Solutions,” *Chemistry of Materials*, vol. 19, no. 4, pp. 787-791, Jan. 2007.

[118] M. A. Correa-Duarte et al., “Alignment of Carbon Nanotubes under Low Magnetic Fields through Attachment of Magnetic Nanoparticles,” *The Journal of Physical Chemistry B*, vol. 109, no. 41, pp. 19060-19063, Sep. 2005.

[119] F. Tsui, L. Jin, and O. Zhou, “Anisotropic magnetic susceptibility of multiwalled carbon nanotubes,” *Applied Physics Letters*, vol. 76, no. 11, pp. 1452-1454, Mar. 2000.

[120] S. Zaric et al., “Estimation of Magnetic Susceptibility Anisotropy of Carbon Nanotubes Using Magnetophotoluminescence,” *Nano Letters*, vol. 4, no. 11, pp. 2219-2221, Oct. 2004.

[121] J. Heremans, C. H. Olk, and D. T. Morelli, “Magnetic susceptibility of carbon structures,” *Physical Review B*, vol. 49, no. 21, pp. 15122-15125, Jun. 1994.

[122] P. Stamenov and J. M. D. Coey, “Magnetic susceptibility of carbon—experiment and theory,” *Journal of Magnetism and Magnetic Materials*, vol. 290–291, P, no. 0, pp. 279-285, Apr. 2005.

[123] M. J. Casavant, D. A. Walters, J. J. Schmidt, and R. E. Smalley, “Neat macroscopic membranes of aligned carbon nanotubes,” *Journal of Applied Physics*, vol. 93, no. 4, pp. 2153-2156, Feb. 2003.

[124] S. Stankovich, R. D. Piner, X. Chen, N. Wu, S. T. Nguyen, and R. S. Ruoff, “Stable aqueous dispersions of graphitic nanoplatelets via the reduction of exfoliated graphite oxide in the presence of poly(sodium 4-styrenesulfonate),” *Journal of Materials Chemistry*, vol. 16, no. 2, pp. 155-158, 2006.